UNIVERSITA' DELLA

CALABRIA

ANALYSIS OF LANDSLIDES REACTIVATED BY VARIATION IN THE GROUNDWATER REGIME

Ph.D. DISSERTATION
BY
ANTONIO DONATO

Ph.D. school in Geotechnical Engineering
Mediterranean University of Reggio Calabria

Department of Civil Engineering
University of Calabria

ANALYSIS OF LANDSLIDES REACTIVATED BY VARIATION IN THE GROUNDWATER REGIME

By

ANTONIO DONATO

Ph.D. Candidate

Ph.D. school in Geotechnical Engineering (XXVII cycle)

Mediterranean University of Reggio Calabria

SUPERVISORS
Professor E. Conte

_____

Professor A.Troncone

_____

COORDINATOR
Professor N. Moraci

_____

Abstract

Landslides can cause considerable damages to infrastructures and human lives. These phenomena appear in different kinematic forms: from extremely slow to extremely rapid. Although slow-moving slope movements do not frequently cause loss of human lives, they may damage structures, interrupt lifelines (highways, railways, pipelines) and require very high costs for their stabilisation. The aim of this research is to propose some approaches for the analysis of landslides controlled by changes in the pore pressure within the slope. In the first part, slow-moving landslides are analyzed. These landslides are characterized by the evidence that deformations are mostly concentrated within a narrow shear zone above which the unstable soil mass essentially moves as a rigid body. Two different approaches are proposed: the first one is a simplified method that is based on the infinite slope model to assess slope stability and on some analytical solutions to predict landslide mobility. The second one utilises a finite element approach in which an elasto-viscoplastic constitutive model in conjunction with a Mohr-Coulomb yield function is incorporated to describe the behaviour of the soil in the shear zone.

For the other soils involved by the landslide, an elastic model is used for the sake of simplicity. A significant advantage of the present methods lies in the fact that few constitutive parameters are required as input data, the most of which can be readily obtained by conventional geotechnical tests.

The rest of the required parameters should be calibrated on the basis of the available monitoring data concerning the changes in the piezometric levels and the associated movements of the unstable soil mass. After being calibrated and validated, both approaches can be used to predict future landslide movements owing to expected groundwater fluctuations or to assess the effectiveness of drainage systems which are designed to control the landslide mobility.

These methods are applied to back-predict the observed field behaviour of three active slow-moving landslides documented in the literature. In the second part of the work, a landslide of large dimensions (about 6 million of cubic meters) that occurred in Maierato (Calabria) on 2010, after a long period of heavy rainfall is analyzed using a finite element approach in order to establish the main causes of the landslide event and to define the failure process occurred.

Acknowledgements

This work has been carried out under the supervision of Professors Enrico Conte and Antonello Troncone in Geotechnical Engineering of Civil Engineering Department in University of Calabria.

The author wishes to express his sincere appreciation to supervisors for their advices and guidance during all time of this research.

Furthermore, the author extends heartfelt thanks to his "brothers in arms" Mirko Vena, Andrea Chidichimo and Paolo Zimmaro for their moral and professional support, which has been always useful.

The author will be always grateful to his family and Caterina for their tireless encouragement and infinite patience.

"Ad maiora semper"

Table of contents

Introduction

The present work concerns the analysis of active landslides which are controlled by changes in the pore water pressure regime within the slope. Usually, these landslide occur in gentle slopes of clayey soils. The main type of movement experienced by them is a translational or roto-translational slide with a velocity of order a few centimetres per year. Therefore, they can be classified as very slow or extremely slow landslides, according to Cruden and Varnes (1996). Typically, deformations are concentrated within a shear zone located at the base of the landslide body, in which the soil shear strength is at residual conditions owing to the high level of accumulated strain (Leroueil et al., 1996). The landslide body on the contrary experiences very small strains, so that it essentially moves as a rigid body. Generally, the slope movements are caused by an increase in pore water pressure with the total stress field that remains practically unchanged with movement. This increase in pore pressure determines a decrease in the effective stress level and consequently in the soil shear strength along the slip surface. Considering that the slope safety factor, *SF*, is governed by the residual strength along the slip surface, the values of *SF* are generally low. Therefore, small changes in pore pressure can produce significant changes in the displacement rate of the unstable soil mass. These changes are often caused by groundwater level fluctuations which in turn are related to rainfall. Therefore, the mobility of these landslides is characterized by alternating phases of rest and reactivation in accordance with the seasonal

rainfall conditions. In particular, raising of the groundwater level causes a reactivation and subsequent acceleration of the landslide because the resisting force decreases and cannot balance the destabilising force. On the other hand, a groundwater level reduction (as occurs during dry periods) mitigates the landslide velocity and may eventually bring the soil mass to rest. The continuous reactivation phases can cause significant damage to the structures and infrastructures located on the slope. Therefore, an adequate consideration of these phenomena is necessary for performing realistic slope stability analyses.

In the current applications, groundwater pressure regime and slope stability are usually dealt with in an uncoupled manner using some theoretical approaches. Specifically, the differential equations governing pore pressure changes within the slope due to changes in hydraulic conditions at the boundary are first solved. Then, the pore pressures calculated at the potential failure surface are used in a limit equilibrium analysis for assessing slope stability.

Simplified methods were also developed to perform directly an approximate assessment of the landslide velocity (Angeli et al., 1996; Gottardi and Butterfield, 2001; Corominas et al., 2005; Maugeri et al., 2006; Herrera et al., 2009; Conte and Troncone, 2012a). In these methods, it is assumed that the landslide body behaves as a rigid block sliding on an inclined plane.

Numerical models based on the finite element method or the finite difference method, in which reliable constitutive laws are incorporated, can provide a better understanding of the complex mechanisms of deformation and failure that occur in the slope.

In this work, active landslides are analysed using two approaches: a simplified method proposed by Conte & Troncone (2011) utilises an analytical solution and assumes that the landslide body behaves as a rigid block sliding on an inclined plane, and the finite element method. In this latter approach, an elasto-viscoplastic constitutive model is included to predict the behaviour of the soil in a finite shear zone located between the moving mass and the underlying stable geological formation. Both the proposed approaches are applied to assess the mobility of well documented active landslides which are periodically activated owing to groundwater level fluctuations. Lastly, a landslide of large dimensions that occurred in Calabria after a long period of heavy rainfall is analysed using a finite element approach in order to study the failure process observed.

The thesis is organized in four chapters: in the first one is reported a literature review concerning landslides caused by changes in the pore water pressure regime. In the second chapter is shown a detailed description of the proposed methods, which are afterwards applied in the third chapter to three active landslides. Finally, the last chapter reports an extensive study on the landslide occurred in Maierato (Southern Italy) on 15 February 2010. This study includes a description of the area, geological and geotechnical characteristics of the soils involved along with an analysis of documents and videos caught by local people, which have provided important information on the failure process occurred. Finally, the numerical analyses have shown that the landslide was a reactivation caused by a considerable increase in the pore water pressure owing to rainfall.

Chapter 1

Landslides induced by pore water pressure changes

1.1. Movements and failure mechanisms of natural slopes

Movements of slopes are a complex problem that involves a variety of geomaterials in different geological and climatic contexts. In order to simplify their analysis, Vaunat et al. (1994) and Leroueil et al. (1996) suggested classifying slope movements into four stages, as listed below and illustrated in Fig.1.1:

1. Pre-failure: this stage includes all the deformation processes leading to failure due to changes in stresses, creep and progressive failure.
2. Failure: characterized by the formation of a complete shear zone through the whole soil mass.
3. Post-failure: it includes landslide movement just from after the onset failure until it stops.
4. Reactivation: the unstable soil mass slides on a pre-existing shear surfaces along which the residual shear strength is at residual condition.

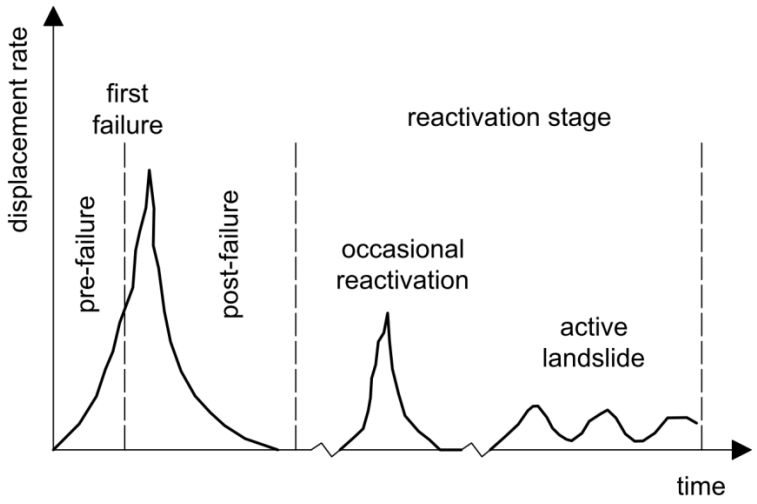

Fig. 1.1 – Schematic evolution of displacement rate (modified from Leroueil, 2001)

Fig.1.2 shows a possible time-horizontal displacement relationship for each stage above-mentioned (Picarelli, 2000).

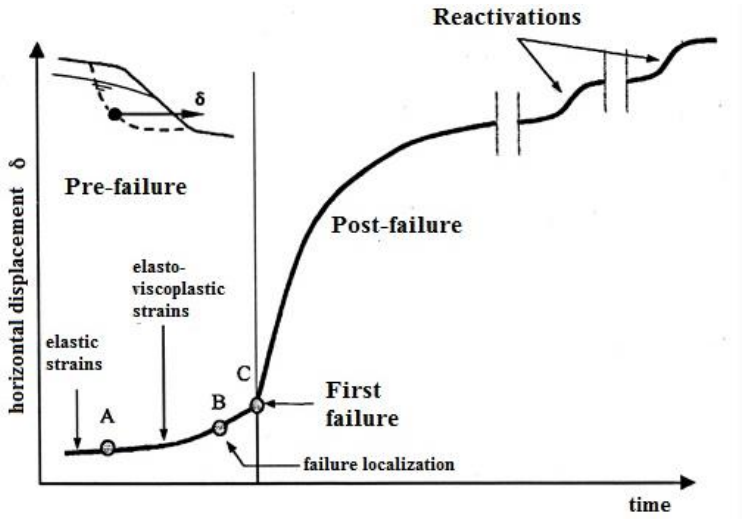

Fig. 1.2 –Evolution of the horizontal displacement of a point located on the failure surface (Picarelli, 2000)

As it can be seen, the reactivation stage is generally characterized by alternate phases of rest and motion. Movements are caused by a reduction of the soil shear strength along the existing slip surface, for example owing to changes in the pore water pressure regime induced by rainfall.

1.2. Rainfall-induced slope failures

Basically, slope failure due to rainfall is mainly caused by:

1. increase in weight of the soil mass;
2. decrease in suction for unsaturated soils owing to water infiltration;
3. rise in groundwater level.

Fig.1.3. shows a flowchart which illustrates the mechanism of rainfall-induced slope failure. Rainfall causes an increase in pore water pressure and consequently a reduction of the soil shear strength which can lead to slope failure.

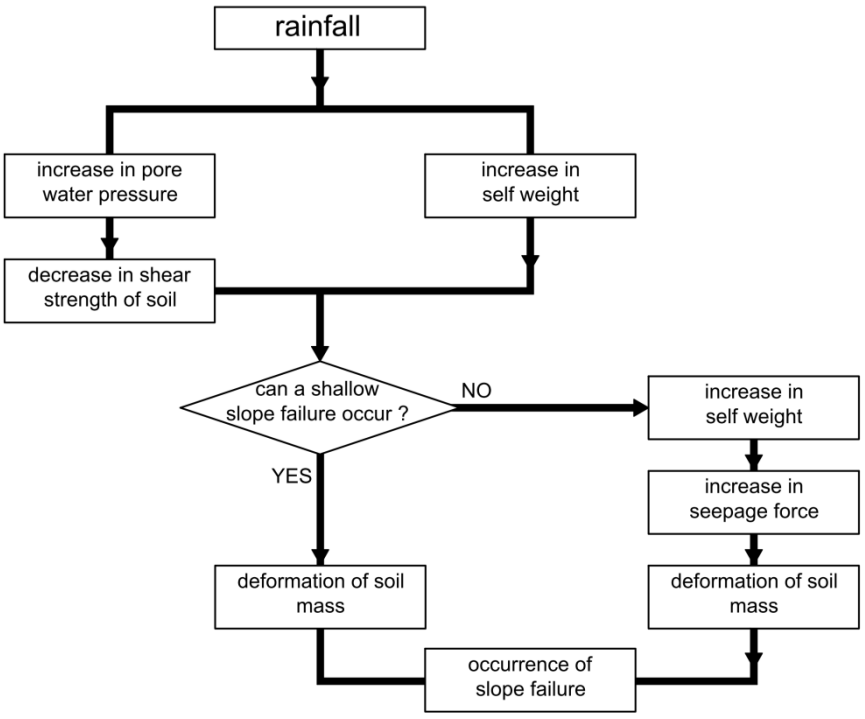

Fig. 1.3 – Mechanism of rainfall-induced slope failure

A shallow landslide usually occurs in the unsaturated zone of the soil. Also, groundwater table goes up causing deformation of soil mass up to the occurrence of slope failure. In this case, the slip surface is generally deep and develops mostly in the saturated zone of the soil.

1.2.1. Slope failure in unsaturated conditions

Due to rainfall infiltration, suction and consequently the soil shear strength decrease. According to the following equation proposed by Fredlund (2000):

$$\tau_f = c' + (\sigma - u_a)\tan\phi' + \chi \cdot s \cdot \tan\phi' \tag{1.1}$$

in which τ_f =failure shear stress, c' = effective cohesion, ϕ' =shear strength angle of the soil, σ = total normal stress; u_a = pore air pressure, s= matrix suction ($s=u_a-u_w$, in which u_w = pore water pressure), and χ = parameter ranging from 0 to 1. The following expression may be employed for χ (Fredlund et al., 1996):

$$\chi = \left(\frac{\theta - \theta_r}{\theta_s - \theta_r} \right)^{\lambda} \tag{1.2}$$

in which θ = volumetric water content at a given suction, θ_s = volumetric water content at saturation, θ_r = residual volumetric water content, λ = a fitting parameter depending on the soil type. As suggested by Fredlund (2000), a value of λ = 1 may be assumed for most inactive soils, such as sand, silt and some fine-grained soils in the suction range of 0-500 kPa. In this case χ can be therefore obtained directly from the soil-water characteristic curve of the soil as a function of suction.

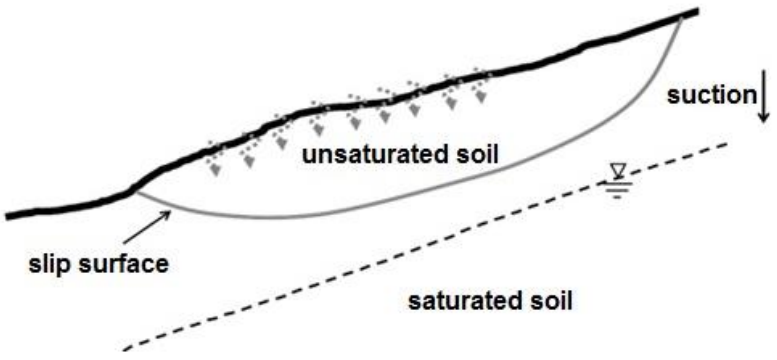

Fig.1.4- Schematic representation of a landslide in saturated conditions

Infiltration process in unsaturated soils represents a complex problem to be analyzed. In particular, it needs to take into account:

- initial conditions (pore pressure in function of the antecedent hydrologic events);
- degree of saturation, matrix suction and hydraulic conductivity.

Several theoretical and numerical studies (Alonso et al., 1995; Collins & Znidarcic, 1997; Sun et al., 1998) were carried out in order to analyze water infiltration in unsaturated soils. Pore pressure measurements performed using piezometers and tensiometers installed in a thick layer of residual soils outcropping in the Sila Massif in Italy were presented by Gullà & Sorbino (1996). In particular, Fig. 1.5 shows some periods during which pore pressure in the shallowest tensiometer (at a depth of 0.81 m) remain essentially constant, although rainfall was close to the maximum value measured during the observation period. This indicates that the wetting front did not propagate to at depth and that it is also necessary to consider evapotranspiration and runoff (from Leroueil, 2001).

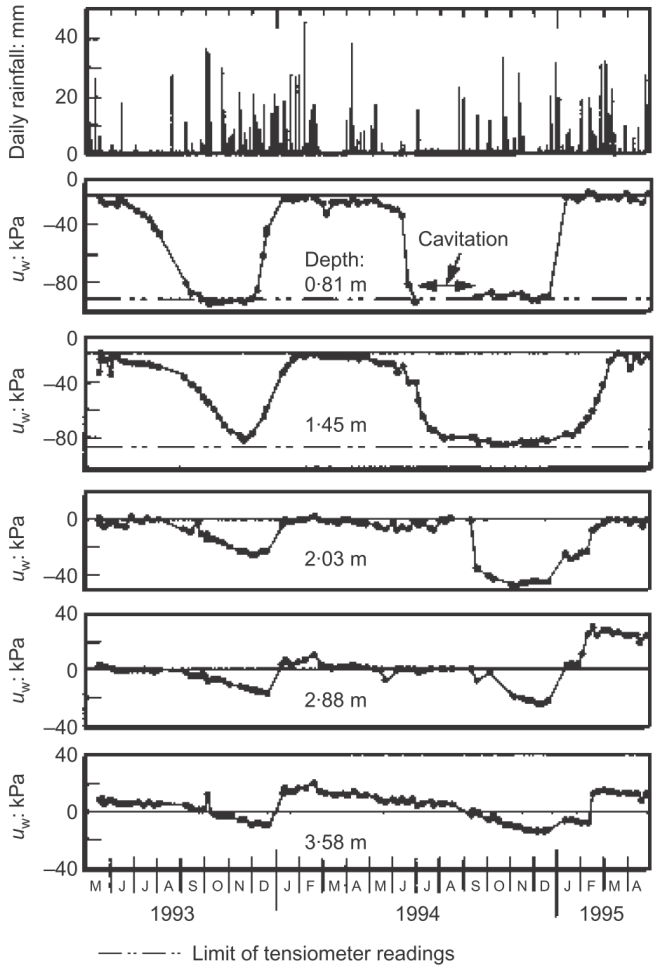

Fig. 1.5–Daily rainfall and pore pressure measurements at Sila Massif (Gullà & Sorbino, 1996)

Similar measurements were made by Johnson & Sitar (1990) in the Briones Regional Park, close to San Francisco. The authors report the pore pressure measurements during the rainfall events on 24 November 1985 and 12-20 February 1986 (Fig.1.6). Pore pressure response to rainfall was quick at the shallowest depth and gradually propagated with delay (12-24 hours) at larger depth. Furthermore, this study evidences the influence of the antecedent conditions on pore pressure response to rainfall.

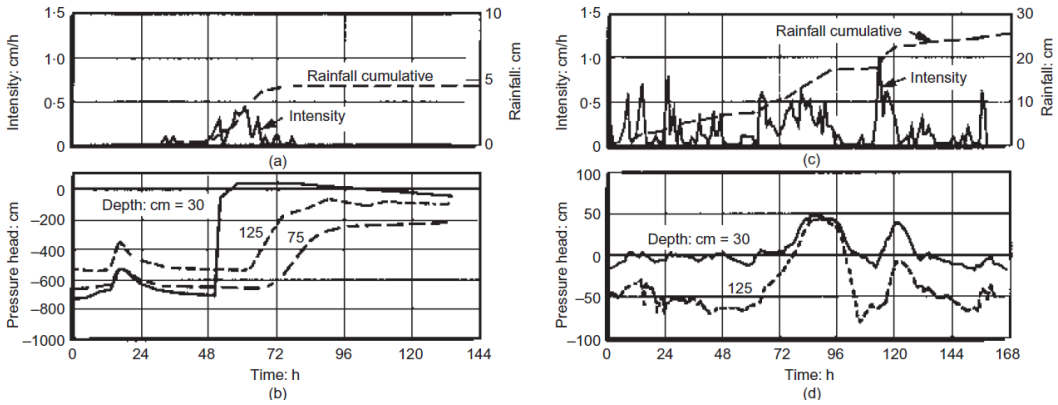

Fig. 1.6–Rainfall and pore pressure measurements at Briones Hills (Johnson & Sitar, 1990)

Observations made by Lacerda (1989), Johnson & Sitar (1990), Montgomery et al. (1997) showed that the development of pore pressure and the failure in unsaturated condition may not result from vertical infiltration only, but also from flows of water through more permeable soil layers and fractured bedrock. Water flow into slopes may also be influenced by animal burrows, desiccation cracks and root holes. The hydrologic and hydrogeological response of a hillslope to rainfall may thus be complex, as schematized in Fig. 1.7, and complicates the prediction of failure.

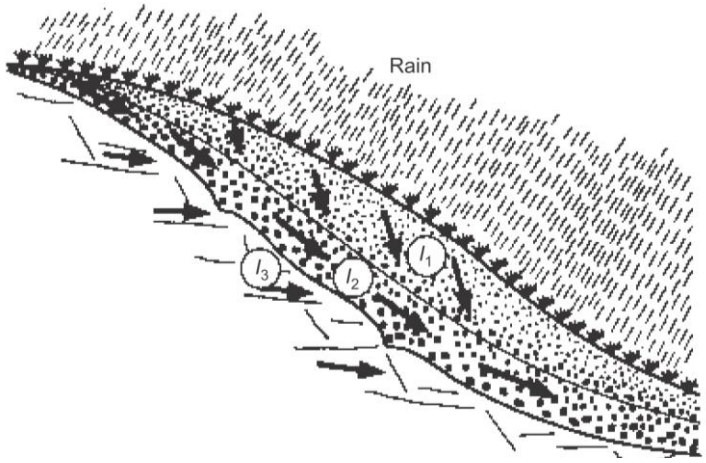

Fig. 1.7– Scheme of the hillslope hydrologic response to rainfall; arrows indicate groundwater flow directions (after Lacerda, 1989; Johnson & Sitar, 1990)

1.2.2. Slope failure in saturated conditions

Landslides are caused by an increase in groundwater level and the failure surface mostly develops within the saturated zone of the soil. Generally, these landslides are denoted as *active landslides*. Active landslides are often controlled by the groundwater level fluctuations which in turn are related to rainfall. The mobility of these landslides is characterized by alternate phases of rest and reactivation according to the weather conditions. In particular, a rising groundwater level owing to rainfall can cause a reactivation of the landslide or, if it is moving, an acceleration of the motion. On the other hand, a groundwater level reduction (as it occurs during dry periods) attenuates the landslide velocity and can bring the unstable soil mass to rest. The main type of movement experienced by these landslides is a translational or roto-translational slide with a velocity of order of some centimetres per year, so that they can be defined as slow-moving landslides (Cruden and Varnes, 1996). Generally, deformations are concentrated within a shear zone located at the base of the landslide body, in which the soil shear strength is at residual condition owing to the high strains accumulated (Leroueil et al., 1996). The soil above the shear zone is on the contrary affected by very small strains and it is characterized by a horizontal displacement profile that is essentially constant with depth.

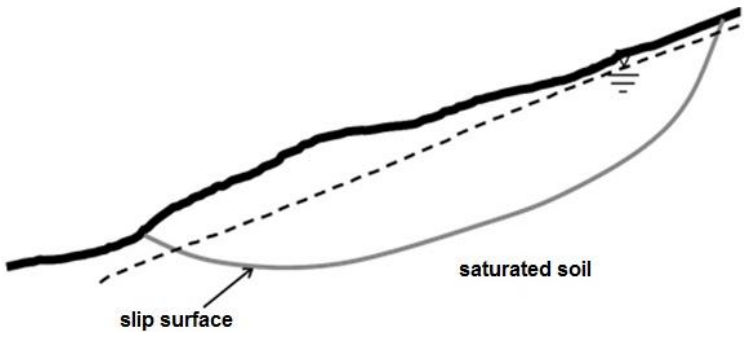

Fig.1.8 - Schematic representation of a landslide in saturated conditions

A change in pore pressure at a certain depth produces a change in effective stress, and consequently, in void ratio. For one-dimensional conditions, this is illustrated in Fig. 1.9.

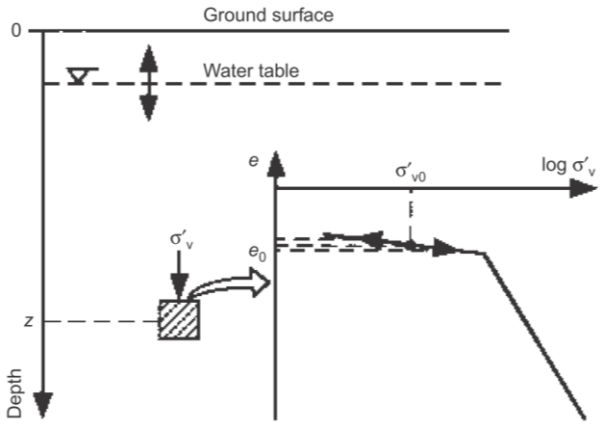

Fig. 1.9– Changes in void ratio due to changes in pore pressure condition for compressible material (from Leroueil, 2001)

Swelling/consolidation process for two-dimensional conditions and isotropic hydraulic conductivities (k_x=k_z) is controlled by Eq. (1.3).

$$\frac{\partial u_w}{\partial t} = \frac{k}{m\gamma_w}\left(\frac{\partial^2 u_w}{\partial x^2} + \frac{\partial^2 u_w}{\partial z^2}\right) = c_v\left(\frac{\partial^2 u_w}{\partial x^2} + \frac{\partial^2 u_w}{\partial z^2}\right) \tag{1.3}$$

where t is time, x and z are spatial coordinates, k is the hydraulic conductivity, m denotes the coefficient of volume change and c_v is the swelling/consolidation coefficient of the soil. As a result of this process, the seasonal variation of pore pressure at upper and lower boundaries of saturated soil deposit is not entirely reflected inside it. Specially in clayey deposits, the upper part is often fissured and behaves as an open aquifer in which water level varies by a maximum amount corresponding to $\Delta u_{z=0}$ (amplitude of pore pressure variation at the ground surface). Fig. 1.10 shows the relative amplitude of pore pressure ($\Delta u_z/\Delta u_{z=0}$), in which Δu_z is the amplitude of pore pressure variation at a depth

z, as a function of z^2/c_v for a sinusoidal variation of the pore pressure at the boundary (solution given by Carlslaw & Jaeger,1959). The soil deposit is assumed saturated and semi-infinite, bounded by a horizontal surface. In particular, two curves are shown: the continuous curve corresponds to one sinusoidal cycle per year, whereas the other is relative to two sinusoidal cycles per year. An analytical solution for analysing this process under more general boundary conditions, was derived by Conte & Troncone (2008).

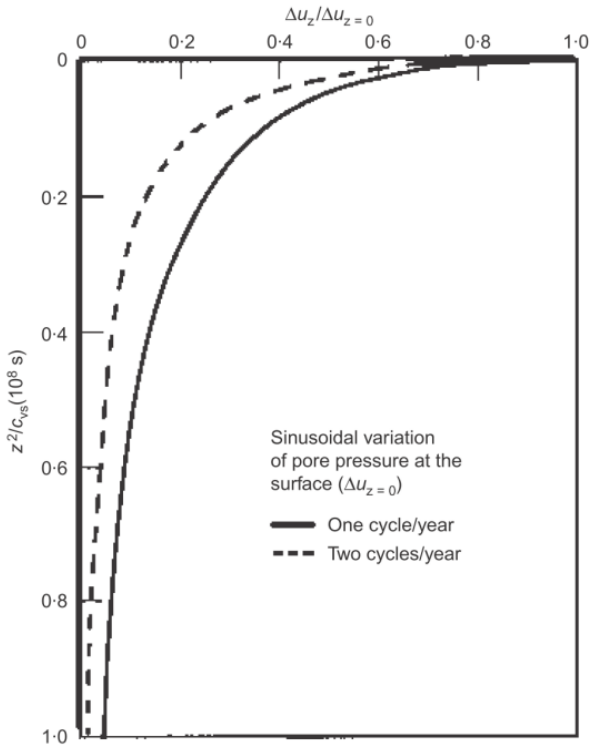

Fig. 1.10 – Variation of pore pressure in a soil deposit due to a sinusoidal variation of pore pressure at the surface (from Leroueil, 2001)

1.3. Landslide mobility owing to seasonal variations of pore water pressure

Active landslides which are controlled by groundwater fluctuations typically occur in gentle slopes of clayey soils and are characterized by a velocity of order of some centimetres per year. In this regard, IUGS (1995) and Cruden & Varnes (1996) proposed a classification based on the values of the landslide velocity. In particular, seven different classes were defined in Tab.1.1.

Class	Description	Typical velocity limits (mm/day)
1	Extremely slow	$< 4.4 \cdot 10^{-2}$ (<16mm/year)
2	Very slow	$4.4 \cdot 10^{-2}$ - 4
3	Slow	4 - 433
4	Moderate	433 - $4.3 \cdot 10^{4}$
5	Rapid	$4.3 \cdot 10^{4}$ - $4.3 \cdot 10^{6}$
6	Very rapid	$4.3 \cdot 10^{6}$ - $4.3 \cdot 10^{8}$
7	Extremely rapid	$> 4.3 \cdot 10^{8}$ (>5m/s)

Tab. 1.1 – Classification proposed by IUGS, 1995 and Cruden & Varnes, 1996

Therefore, the landslides at issue typically fall into classes 1 to 3. Analysis, modeling and prediction of such phenomena present several difficulties, essentially attributable to four different sources (Vulliet & Hutter, 1988c):

- most movements occur in isolated and remote areas and access to the sites may be difficult;
- monitoring of slow movements (typically few centimeters per year) needs a large period of observation;
- modelling the time-dependent behaviour of the soils involved requires specific tests and adequate constitutive models.
- slope movements are strongly affected by hydrological factors.

In spite of these difficulties, a remarkable improvement has been made in the last years. Theoretically, movements start at the beginning of rainy season and stop during dry season when rain infiltration is poor. It is possible to establish a

triggering threshold, represented by a critical value of pore pressure beyond which a reactivated landslide occurs. Nevertheless, the real behaviour of the soils is essentially viscous and slopes may move even if rainfall is zero. As an example, the relationship among rainfall, groundwater level and velocity of the Vallcebre landslide are shown in Fig.1.11 (Corominas et al., 2000). It is worth noting that in some periods the landslide moves, although rainfall is nil.

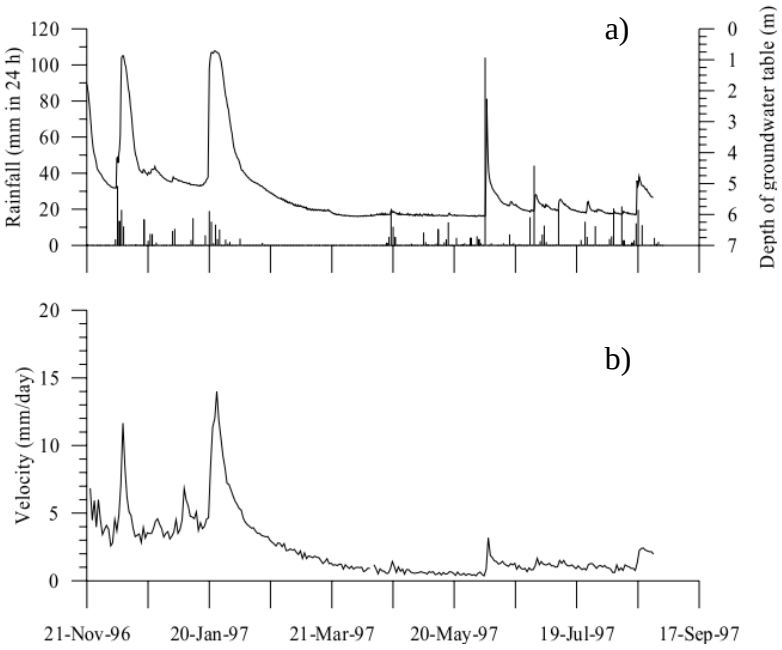

Fig. 1.11 – a): rainfall records (bars) and groundwater level changes at a borehole.
b): velocity of landslide at the same borehole (Corominas et al., 2000)

Two factors should be considered for analyzing active landslides: the viscous behaviour of the soils involved and the shear strength along the pre-existing slip surface that is at residual condition.

1.3.1. Residual shear strength

The residual strength assumes great importance in analyzing slope stability. In particular, it is reached after large displacements when a parallel reorientation of platy to shearing direction is achieved. Residual strength is influenced by several factors, such as mineralogy, shape of particles, normal stress, type of shearing, pore pressure and rate of displacement.

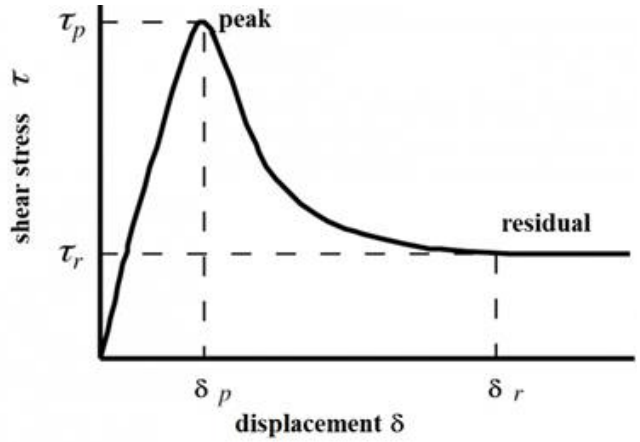

Fig. 1.12 – Brittleness of soils (modified from Leroueil, 2001)

For many clayey soils, the relation between normal effective stress and residual strength is nonlinear (Skempton, 1985; Stark & Eid, 1994). A typical example is shown in Fig. 1.13, which reports some experimental results of laboratory tests on reconstituted specimens of Laviano clay (Picarelli, 1991).

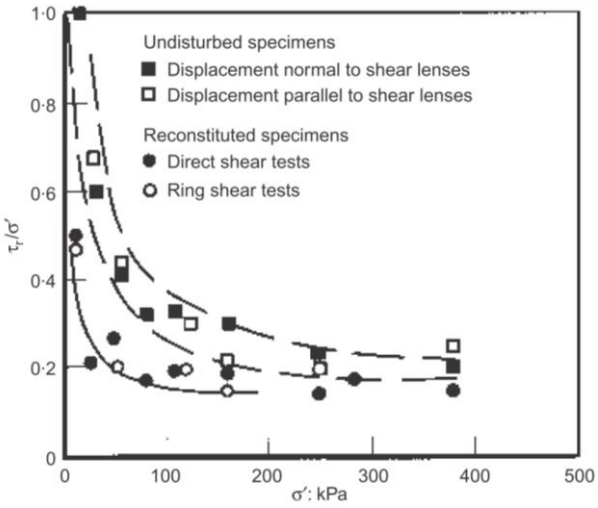

Fig. 1.13– Residual shear strength of Laviano clay (Picarelli, 1991)

Generally, the soil consists of both round and platy particles. In this connection, Lupini et al. (1981) presented the results in Fig. 1.14, from which it is evident that if the percentage of platy particles is small, no reorientation of them (rolling shear) is observed. Therefore, the residual shear angle ϕ'_r is slightly smaller than that at the critical state, ϕ'_{cr}. Conversely, if the percentage of platy particles is large, a reorientation of them is observed. The residual shear angle ϕ'_r is significantly smaller than that corresponding to the critical state, ϕ'_{cr}.

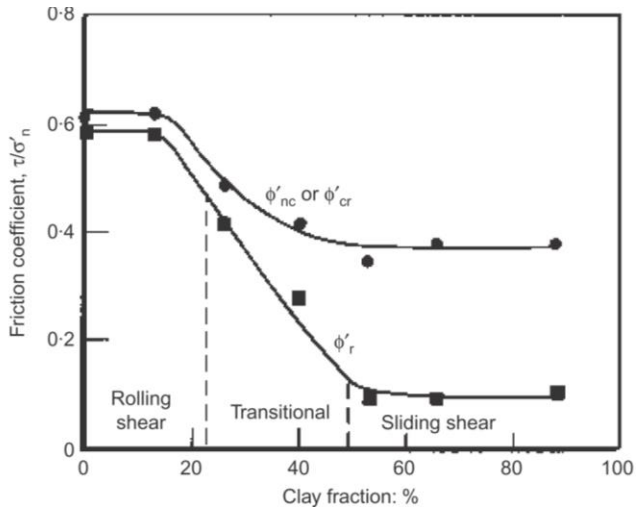

Fig. 1.14 – Ring shear tests on sand-bentonite mixtures (Lupini et al., 1981; Skempton, 1985)

The residual strength increases by a few percent when the rate of displacement increases by one order of magnitude. This is not significant when slope stability is analyzed (Skempton, 1985), but it assumes remarkable consequences for the movements at each reactivation stage. Important effects on the residual shear angle can be ascribed to pore water chemistry (Di Maio, 1996 a,b). In particular, Fig. 1.15 shows some results obtained on three Italian clays and on Ponza bentonite. The specimens were prepared either with saturated NaCl solution or with distilled water.

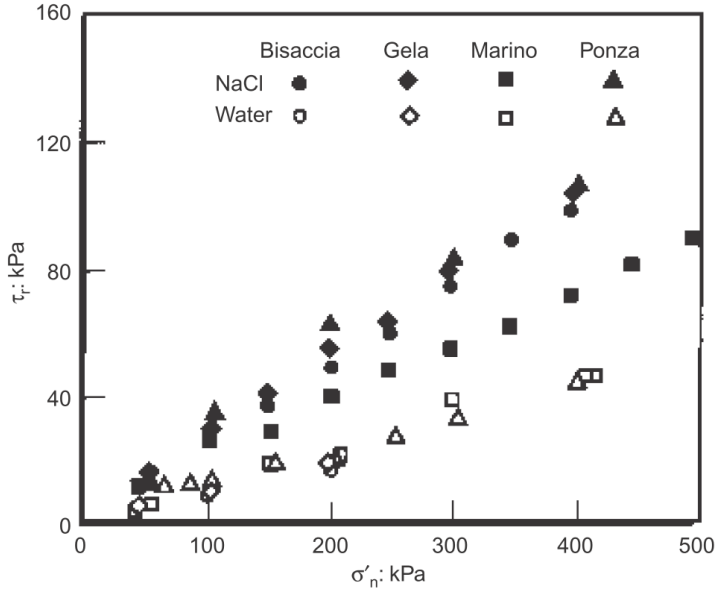

Fig. 1.15 - Residual shear strength plotted against normal stress of specimens reconstituted with water and specimens reconstituted with saturated NaCl solution (Di Maio, 1996a)

As it can be seen, saturating the specimens with NaCl solution leads to higher values of ϕ'_r. Furthermore, ϕ'_r also varies with the concentration of NaCl solution, as shown in Fig. 1.16. As it can be seen, significant changes in ϕ'_r occur for concentration of NaCl between 0 and 35 g/l.

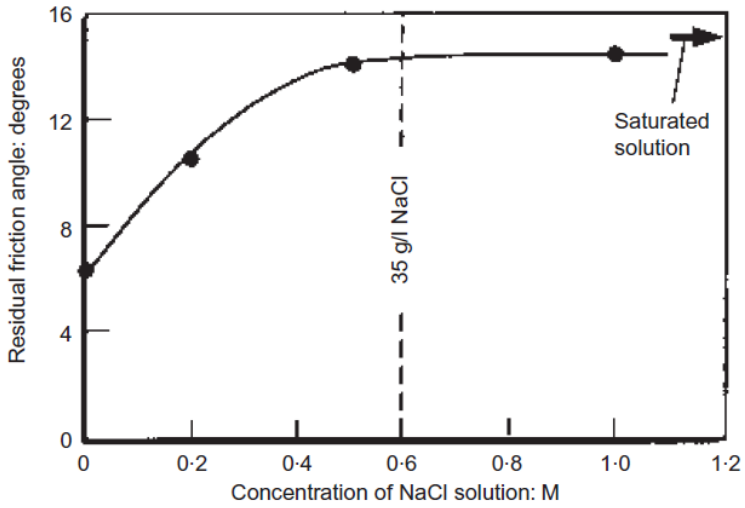

Fig. 1.16 - Residual shear angle for various concentrations of NaCl solution (Di Maio, 1996b)

1.3.2. Viscous behaviour of the soil

Landslide movements can be delayed due to pore pressure redistribution (D'Elia et al., 1985) or viscous effects (Bracegirdle et al., 1992; Savage and Chleborad, 1982; Vulliet and Hutter, 1988; Van Asch and Van Genuchten, 1990; Leroueil and Marques, 1996). Owing to viscous nature of the soils, the velocity may not abruptly vary even if the safety factor tends to unity. The rate of displacement, v, depends on the shear stress, τ, along the slip surface according to the following relationship:

$$v = f\tau \tag{1.4}$$

where f is a function related to viscosity, soil strength and stress acting on slip surface. Evidence of the viscous behaviour of the clayey soils was observed in several tests. The behaviour observed in creep tests can be described by the following equation (Singh & Mitchell, 1968):

$$\dot{\varepsilon}_1 = Ae^{\alpha q}\left(\frac{t_1}{t}\right)^m \tag{1.5}$$

where $\dot{\varepsilon}_1$ represents the axial strain rate, t the time, q is the stress ratio (equal to the applied deviatoric stress divided by the deviatoric stress at failure for conventional compression tests), m is the slope of $\log \dot{\varepsilon}_1$-log t curve, t_1 is a reference time generally equal to 1 min, and α and A are creep parameters.

Bishop & Lovenbury (1969), Larsson (1977), Tavenas et al. (1978), and D'Elia (1991) performed long-term creep tests on clayey soils. In particular, Fig. 1.17 shows the creep test results obtained on Saint Alban clay, for different stress conditions inside the limit state curve.

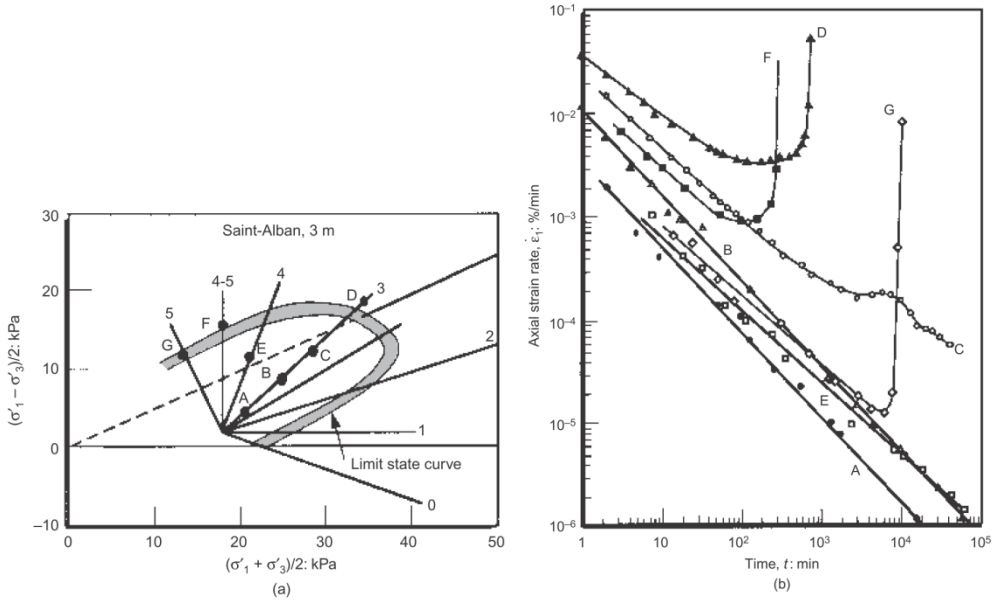

Fig. 1.17 – Axial strain rate vs. time for creep tests on Saint Alban clay (Tavenas et al., 1978)

The results in Fig.1.17b show the development of creep strains with time along linear relationships in a logarithm diagram of axial strain rate versus time. Considering the points D, F, G, the strain rate increases up to failure after reaching a minimum value. Similar results were achieved for the Santa Barbara clay (D'Elia, 1994) and on some shale clays (D'Elia, 1991), as shown in Fig. 1.18.

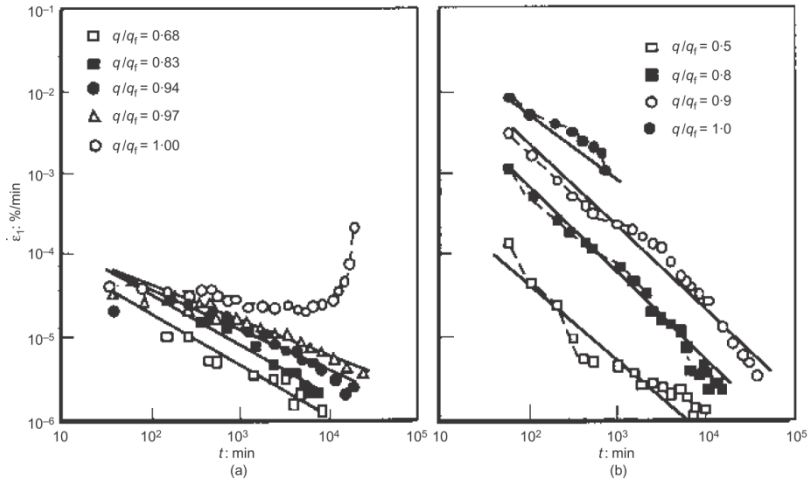

Fig. 1.18 – Axial strain rate vs. time for creep tests at various stress levels (q/q_f) on:
a) Santa Barbara clay (D'Elia, 1994); b) Shale clays (D'Elia, 1991)

Fig. 1.19 shows the results of the tests performed on the stiff Mascouche clay by Marchand (1982). The stress conditions referred to failure are indicated with square and triangle symbols. Long-term triaxial creep tests are also carried out with stress conditions marked as black dots.

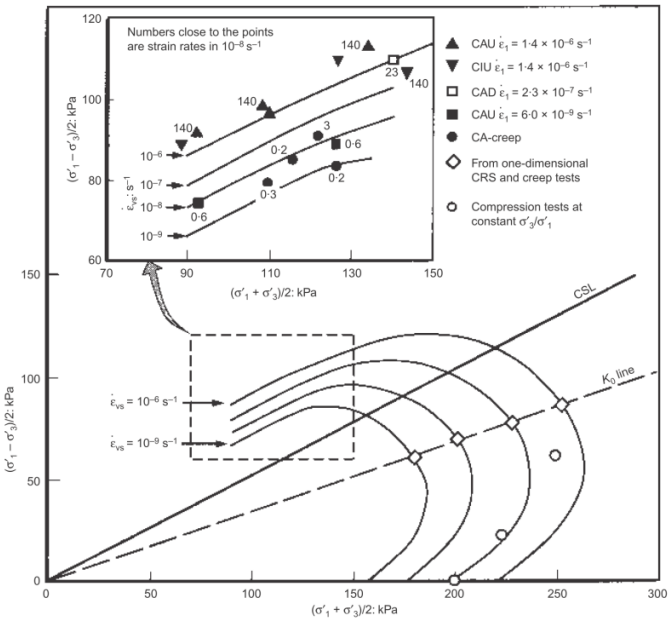

Fig. 1.19 – Influence of strain rate on the limit state curve of Mascouche clay (Leroueil & Marques, 1996 after Marchand, 1982)

Other creep tests were performed with different deviatoric stress (Figs. 1.20-1.22). Also in these tests the behaviour of soil presents strain rate dependence.

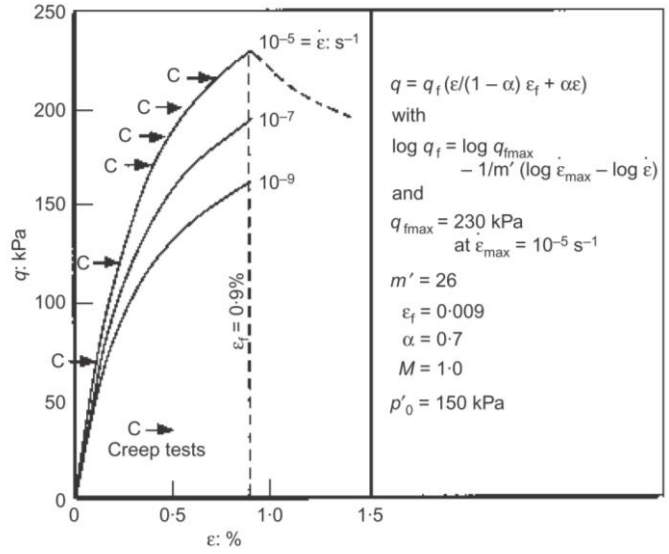

Fig. 1.20 – Strain rate dependence of stress-strain behaviour and input parameters of triaxial creep tests simulation (Leroueil, 1998a)

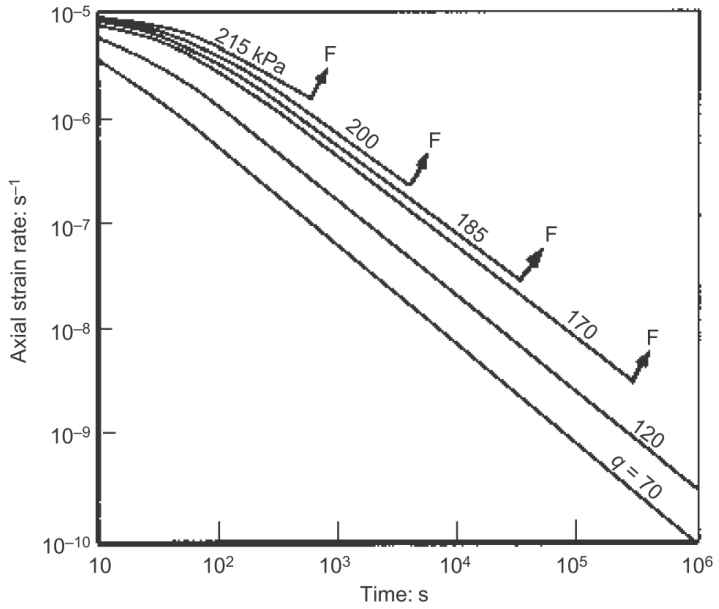

Fig. 1.21 – Simulated creep tests for the conditions from Fig.1.20 (Leroueil, 1998a)

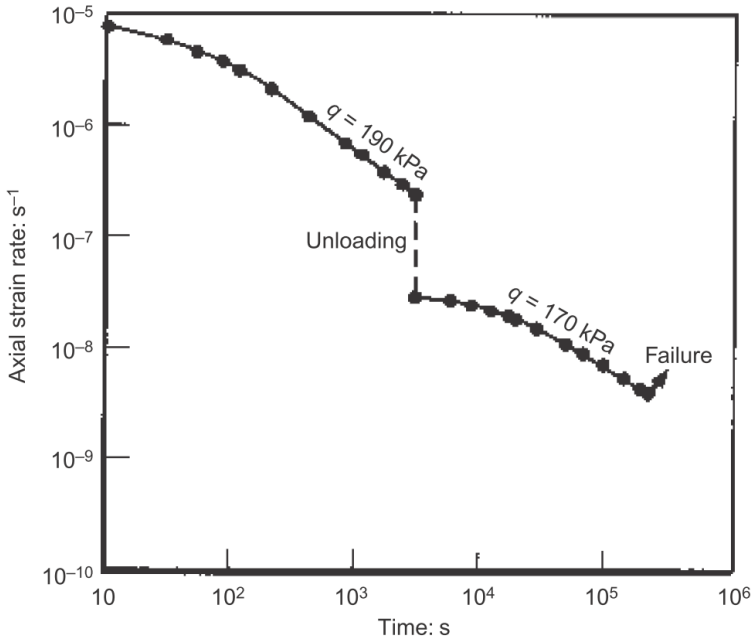

Fig. 1.22– Simulated creep tests in which the deviatoric stress is 190 kPa for 3000 min and then decrease to 170 kPa (Leroueil, 1998a)

The critical accumulated strain seems to assume an important role, because after a slight decrease in deviatoric stress (from 190 to 170 kPa after 50 min), creep strain continues to develop until the soil reaches failure.

1.4. From hydrologic conditions to landslide mobility

An important objective for the geotechnical engineers is to establish a relationship for practical use among hydrologic conditions, pore pressure, soil strength, safety factor and rate of movement. Fig.1.23 shows the conceptual scheme proposed by Leroueil (2001) to illustrate the possible approaches that can be used to relate rainfall to landslide mobility. According to Fig. 1.23, the most complete approaches start from rainfall and include all the intermediate steps, such as pore pressure changes, soil strength and safety factor, and finally rate of movement.

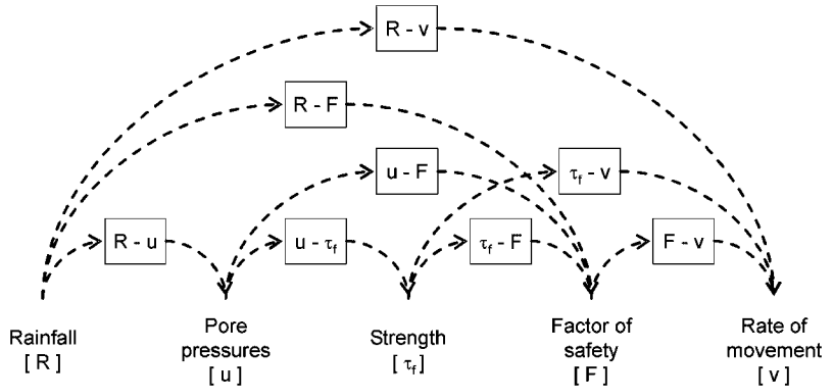

Fig. 1.23 - From hydrologic conditions to safety factor and rate of displacement (modified after Leroueil, 2001)

In the current applications, groundwater pressure regime and slope stability are usually dealt with in an uncoupled manner using some theoretical approaches. Specifically, the differential equations governing pore pressure changes within the slope due to changes in hydraulic conditions at the boundary are first solved. Then, the pore pressures calculated at the potential failure surface are used in a limit equilibrium analysis for assessing slope stability. In this connection, Conte and Troncone (2012a) proposed a simplified method that

utilises the infinite slope model to assess slope stability and an analytical solution (Conte and Troncone 2008) to evaluate the changes in pore pressure at the slip surface from the pore pressure measurements at a piezometer which is installed above this surface. However, the limit equilibrium method is in principle unable to analyse active landslides for which a realistic prediction of the slope movements is required rather than a calculation of the safety factor. Calvello et al. (2008) proposed a numerical procedure in which the changes in pore pressure are first calculated by a physically based analysis. Then, the displacement rate at selected points is related empirically to the changes in the safety factor with time. These changes are evaluated by the limit equilibrium method on the basis of the changes in pore pressure calculated in the previous step. In particular, these authors suggest two empirical relationships between time-dependent safety factor (*SF*) and the velocity along the slip surface, *v(t)*. These relationships are:

$$v(t) = v_{\max} \frac{SF_{\max} - SF(t)}{SF_{\max} - 1} \tag{1.6}$$

$$v(t) = v_{\min} \cdot 10^{\left(\frac{1-\log SF(t)}{\log SF_{\max}}\right) \cdot \log \frac{v_{\max}}{v_{\min}}} \tag{1.7}$$

in which *v(t)* is assumed to be zero when $SF > SF_{max}$. Both expressions assume the existence of a threshold for the safety factor (SF_{max}). The maximum value of *v(t)* corresponding to *SF*=1 (onset failure). These relationships are plotted in Fig. 1.24.

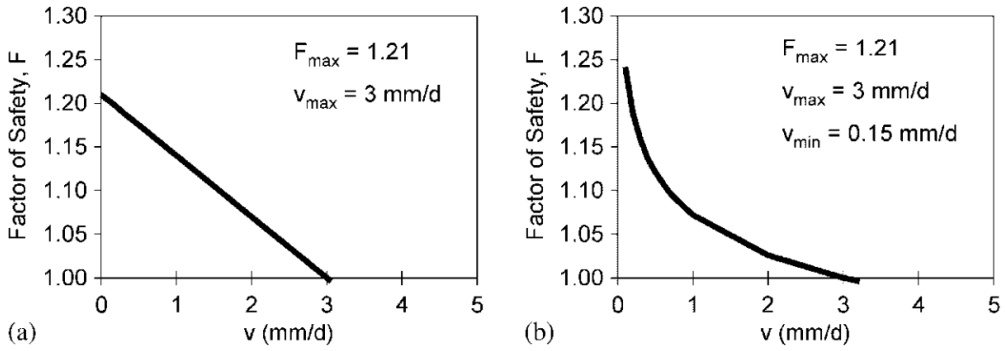

Fig. 1.24 - Empirical relationships between safety factor and velocity:
a) linear function; b)log-log function (Calvello et al., 2008)

Simplified methods were also developed to perform directly an approximate assessment of the landslide velocity (Angeli et al. 1996; Gottardi and Butterfield 2001; Corominas et al. 2005; Maugeri et al. 2006; Herrera et al. 2009; Conte and Troncone 2011, 2012b). In these methods, it is assumed that the landslide body behaves as a rigid block sliding on an inclined plane. The model is similar to that originally proposed by Newmark (1965) for predicting the earthquake-induced permanent displacements of slopes. Unlike this latter model, however, it is assumed that a viscous force is activated when motion of the unstable soil starts. This additional resisting force is applied at the base of the sliding soil mass and should account for, in an approximate manner, the effect of energy dissipation owing to the permanent strains occurring in the shear zone. In this context, a method is used in the subsequent chapters to analyze some case studies documented in literature. Numerical models based on the finite element method or the finite difference method, in which reliable constitutive laws are incorporated, can obviously provide a better understanding of the complex mechanisms of deformation and failure that occur in the slope (Lollino et al. 2010). Considering that in slow-moving landslides the slope

movements are essentially of viscous nature (Savage and Chleborad 1982; Vulliet and Hutter 1988; Van Asch and Van Genuchten 1990; Bracegirdle et al. 1992), Desai et al. (1995) developed a finite element approach for the analysis of natural slopes that exhibit slow and continuous movements under gravity load (creeping slopes). In this approach, an elasto-viscoplastic constitutive model is included to predict the behaviour of both the unstable soil mass and the soil in a finite "shear zone" located between the moving mass and the underlying stable geological formation. A similar constitutive model was also implemented in the finite element program Code_Bright (Olivella et al. 1996; Ledesma et al. 2009). Picarelli et al. (2004) used the constitutive law by Singh and Mitchel (1969) to describe the viscous behaviour of the landslide body, and elasto-plastic interface elements to simulate the slip surface. A different finite element approach is proposed in the present work for evaluating slow-moving landslide mobility owing to groundwater level fluctuations. This approach utilises an elasto-viscoplastic constitutive model in conjunction with a Mohr-Coulomb yield function to model the behaviour of the soil in the shear zone where the landslide displacement occurs. A linear elastic model is on the contrary considered for the other soils involved by the landslide.

In the Chapter 2, the approaches utilized in the present work are widely described.

Chapter 2
Methodology

2.1. Introduction

In this chapter, two different approaches of different complexity are presented to analyse active landslides induced by changes in pore water pressure regime:

- a simplified approach;
- a finite element approach.

The reader should understand that it needs to find a right compromise between difficulties in modeling and accuracy in terms of results achieved. Accordingly, it is well to select the method in relation to the purpose of the analysis to carry out. In the next chapter, the proposed approaches will be applied to evaluate the mobility of three active landslides documented in the literature.

2.2. Simplified approach

The simplified approach is essentially analytical and is based on the assumption that the landslide body behaves as a rigid block sliding on an inclined plane that makes an angle α with horizontal plane. This model is similar to that proposed by Newmark (1965) for predicting earthquake-induced permanent displacement of slopes. The slope stability is assessed by a safety factor (*SF*), defined as:

$$SF(t) = \frac{c' + \left[\gamma h \cos\alpha - u_0 - u(t)\right]\tan\phi'}{\gamma h \sin\alpha} \tag{2.1}$$

where c' is the effective cohesion, ϕ' the shear resistance angle of the soil (at residual condition $c' = c'_r$ and $\phi' = \phi'_r$), γ is the unit weight, h is the depth of

failure surface, α is the slope angle, $u_0 = \gamma_w h_w \cos\alpha$ denotes steady-state pore pressure at failure surface and *u(t)* describes its changes with time.

It is possible to obtain the critical value of *u* (denoted as u_c), assuming *SF*=1:

$$u_c = \frac{c'}{\tan\phi'} + \gamma h\left(\cos\alpha - \frac{\sin\alpha}{\tan\phi'}\right) - \gamma_w h_w \cos\alpha \qquad (2.2)$$

This parameter is a critical threshold which may be considered to establish whether the landslide is triggered by a raising of the groundwater level. Specifically, if the value of u_c is greater than *u* at any time, it is *SF*>1 and hence the slope is stable. On the other hand, when *u* equals u_c a given time, a slope failure occurs at this time (*SF*=1). In the present study, it is assumed that u_c remains constant with time. This assumption is undoubtedly sound for active landslides in which the soil shear strength along the slip surface is at residual conditions.

2.2.1. Changes in pore pressure induced by groundwater fluctuations

The two-dimensional differential equation governing pore water pressure changes in a saturated, homogeneous and isotropic soil is:

$$\frac{\partial u}{\partial t} = c_v\left(\frac{\partial^2 u}{\partial x^2} + \frac{\partial^2 u}{\partial z^2}\right) \qquad (2.3)$$

which *x* and *z* are the spatial coordinates shown in Fig. 2.1, and c_v is coefficient of swelling/consolidation of the soil generally in its overconsolidated domain (Leroueil, 2001). The expression of c_v is:

$$c_v = \frac{k}{\gamma_w\ m_v} \qquad (2.4)$$

where k is the saturated hydraulic conductivity and m_v is the coefficient of volume change of the soil skeleton. It is worth noting that in the present study c_v is assumed to be constant. Although this assumption is in principle an approximation, it is often accepted in practice. This especially occurs when the slope is characterized by the presence of fissures, discontinuities or thin layers of very permeable materials, the effects of which cannot be directly accounted for in the analyses. In these circumstances, the coefficient c_v appearing in Eq. (2.4) should be therefore considered as an operative parameter which controls the overall response of the slope to groundwater fluctuations.

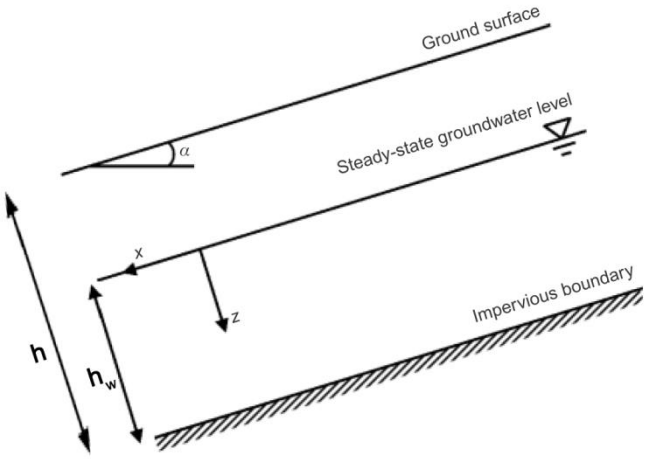

Fig. 2.1 - Infinite slope model with an indication of the failure surface and the steady-state groundwater level (Conte & Troncone, 2011)

For an infinite slope the term $\frac{\partial^2 u}{\partial x^2}$ in Eq. (2.3) is identically zero, and Eq. (2.3) reduces to the following one-dimensional equation:

$$\frac{\partial u}{\partial t} = c_v \frac{\partial^2 u}{\partial z^2} \tag{2.5}$$

in which u is a function of z and t.

The initial condition considered in this study to integrate Eq. (2.5) is:

$$u = 0 \qquad \text{at} \quad t = 0, \text{ and for any } z \tag{2.6}$$

Moreover, the boundary condition at z=0 (and t>0) is:

$$u = f(t) \tag{2.7}$$

where $f(t)$ is a time-dependent function describing the change in pore water pressure at the boundary. In the present study, $f(t)$ expresses the changes in pore pressure measured at a piezometer which is installed at a depth above the slip surface (Fig. 2.2). It is relevant to note that in this case the spatial coordinate z has to be reckoned from the measuring section of the piezometer, as shown in Fig. 2.2. Lastly, under the assumption that at a distance H from this measuring section there is an impervious surface, it is imposed that:

$$\frac{\partial u}{\partial z} = 0 \qquad \text{at} \quad z=H \quad \text{and} \quad t>0 \tag{2.8}$$

where H can be greater or equal to the depth of the failure surface. This latter depth is indicated as z_w in Fig. 2.2.

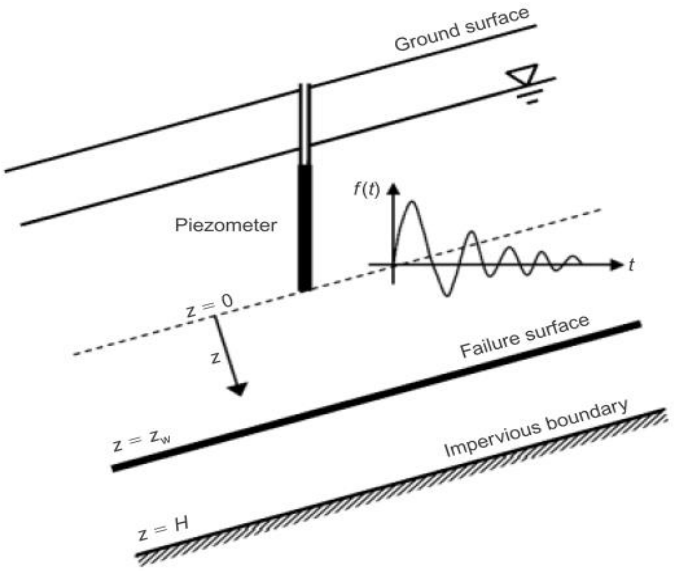

Fig. 2.2 - Infinite slope in which a piezometer is installed above failure surface (Conte & Troncone, 2011)

To achieve a solution to Eq. (2.5) when *f*(*t*) is expressed by an arbitrary time-dependent function, the solution proposed by Conte and Troncone (2008) for solving a different geotechnical problem, may be adopted.

The solution procedure first requires that *f(t)* is expanded in Fourier series, by using a finite number of component *M*, as:

$$f(t) = \frac{A_0}{2} + \sum_{k=1}^{M} \left[A_k \cos(\omega_k t) + B_k \sin(\omega_k t) \right] \tag{2.9}$$

in which the frequency of k^{th} components is:

$$\omega_k = \frac{2k\pi}{T} \qquad \text{with } k = 1,2,...,M \tag{2.10}$$

T is the period of *f(t)*, which should be chosen greater than the final time of analysis as shown in Fig. 2.3).

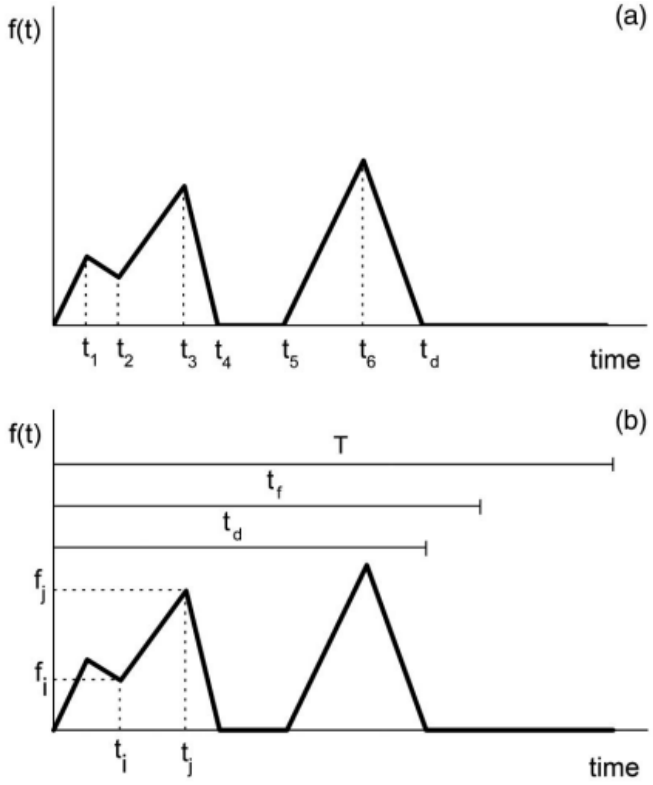

Fig. 2.3 - Function *f(t)*, consisting of a sequence of linear functions with time: a) *f(t)*versus time; b) scheme considered for calculating A_0,A_k and B_k with an indication of the duration t_d, final time t_f and the period T (Conte & Troncone, 2011)

A_k ,B_k and A_0, are the series amplitudes, expressed as follows:

$$A_k = \frac{2}{T}\left[\int_0^{t1} f(t)\cos(\omega_k t)dt + \int_{t1}^{t2} f(t)\cos(\omega_k t)dt + ... + \int_{t6}^{td} f(t)\cos(\omega_k t)dt\right] \quad (2.11)$$

in which:

$$\int_{ti}^{tj} f(t)\cos(\omega_k t)dt = \frac{fi}{\omega_k}\left[\sin(\omega_k t_j) - \sin(\omega_k t_i)\right] + \\ + \frac{1}{\omega_k}\left(\frac{f_j - f_i}{t_j - t_i}\right)\left\{(t_j - t_i)\sin(\omega_k t_j) + \frac{1}{\omega_k}\left[\cos(\omega_k t_j) - \cos(\omega_k t_i)\right]\right\} \quad (2.12)$$

similarly:

$$B_k = \frac{2}{T}\left[\int_0^{t1} f(t)\sin(\omega_k t)dt + \int_{t1}^{t2} f(t)\sin(\omega_k t)dt + ... + \int_{t6}^{td} f(t)\sin(\omega_k t)dt\right] \quad (2.13)$$

where:

$$\int_{ti}^{tj} f(t)\sin(\omega_k t)dt = \frac{fi}{\omega_k}\left[\cos(\omega_k t_j) - \cos(\omega_k t_i)\right] + \\ - \frac{1}{\omega_k}\left(\frac{f_j - f_i}{t_j - t_i}\right)\left\{(t_j - t_i)\cos(\omega_k t_j) - \frac{1}{\omega_k}\left[\sin(\omega_k t_j) - \sin(\omega_k t_i)\right]\right\} \quad (2.14)$$

and:

$$A_0 = \frac{2}{T}\left[\int_0^{t1} f(t)dt + \int_{t1}^{t2} f(t)dt + ... + \int_{t6}^{td} f(t)dt\right] \quad (2.15)$$

$$\int_{ti}^{tj} f(t)dt = \frac{1}{2}(f_i + f_j)\cdot(t_j - t_i) \quad (2.16)$$

Then, the pore pressure changes *u(t)* at the depth of the failure surface (i.e. $z=z_w$, see Fig. 2.2) can be calculated using the following equation:

$$u(t) = \frac{A_0}{2}\bar{u}(t) + \sum_{k=1}^{M} u_k(t) \quad (2.17)$$

where:

$$\bar{u}(t) = 1 - \frac{4}{\pi}\sum_{n=1}^{\infty}\left(\frac{1}{2n-1}\right)\sin\left[\frac{M_n z_w}{H}\right]e^{-M_n^2 T_V} \quad (2.18)$$

$$u_k(t) = 2\sum_{n=1}^{\infty} \frac{M_n \theta_k}{1+\theta_k^2 M_n^4} X_n \sin\left[\frac{M_n z_w}{H}\right] \quad (2.19)$$

and:

$$M_n = \frac{(2n-1)\pi}{2} \quad (2.20)$$

$$T_V = \frac{c_v t}{H^2} \quad (2.21)$$

$$\theta_k = \frac{c_v}{\omega_k H^2} \quad (2.22)$$

$$X_n = \left(B_k - A_k \theta_k M_n^2\right)\left[e^{-M_n^2 T_V} - \cos(\omega_k t)\right] + \left(A_k - B_k \theta_k M_n^2\right)\sin(\omega_k t) \quad (2.23)$$

2.2.2. Landslide mobility

Following several authors (Angeli et al., 1996; Gottardi & Butterfield, 2001; Corominas et al., 2005; Herrera et al., 2009), the motion equation, for infinite slope shown in Fig. 2.4, is:

$$\frac{W}{g}\frac{dv}{dt} = D - R - F \quad (2.24)$$

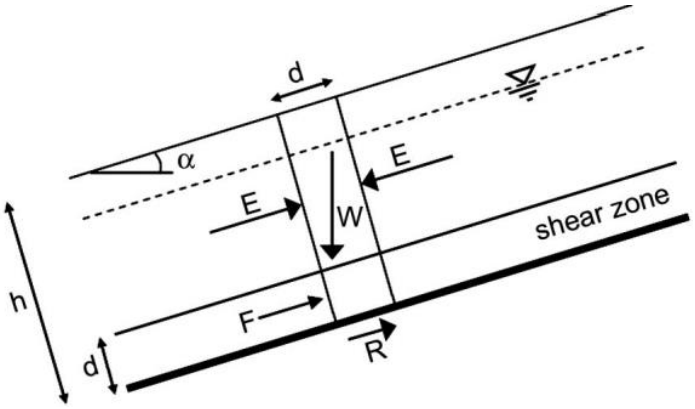

Fig. 2.4 - Sliding-block model considered in this model (Conte & Troncone, 2011)

where *v* is the velocity of unstable soil mass in parallel direction to the inclined plane; *W* the weight of slice; *g* the gravitational acceleration; *D* represents the driving force; *R* is the Mohr-Coulomb resisting force and *F* is a viscous force applied at the base of the sliding soil mass.

In this equation, forces are expressed per unit length in the normal direction to cross section of the slope. According to the scheme in Fig. 2.4, the length of the slice is assumed equal to the thickness of the shear zone for the sake of convenience. Moreover, *W*,*D* and *R* are calculated as follows:

$$W = \gamma h d \tag{2.25}$$

$$D = W \sin\alpha \tag{2.26}$$

$$R = c' d + \left[\gamma h \cos\alpha - \gamma_w h_w \cos\alpha - u(t)\right] d \tan\phi' \tag{2.27}$$

In addition, *F* is evaluated using Bingham's law as illustrated in Fig. 2.5:

$$F = \mu v \tag{2.28}$$

where μ is the viscosity of the soil in the shear zone.

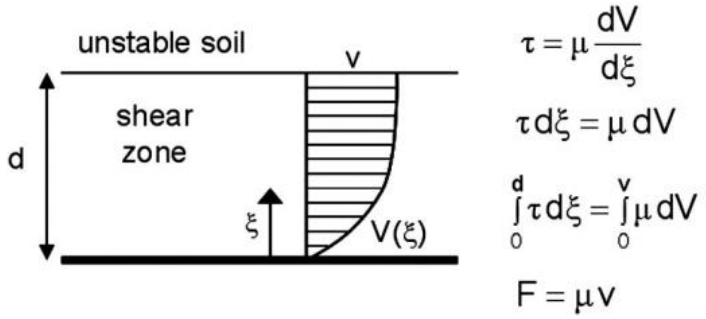

Fig. 2.5 - Velocity profile in the shear zone by using Bingham's law for the viscous force (Conte & Troncone, 2011)

Substituting equations (2.25)-(2.28), into (2.24) and considering (2.3), the following differential equation can be achieved:

$$\frac{\gamma h}{g}\frac{dv}{dt} + \beta v = \left[u(t) - u_c\right]\tan\phi' \tag{2.29}$$

where:

$$\beta = \frac{\mu}{d} \tag{2.30}$$

An evaluation of this latter parameter (although possible) is indeed a very complex operation.

Therefore, the value of β should be calibrated on the basis of field measurements of landslide velocity, as shown in the subsequent section.

To evaluate the landslide velocity, it is convenient to rewrite (2.30) in a compact form, as:

$$\frac{dv}{dt} + \lambda v = [u(t) - u_c]\chi \tag{2.31}$$

where:

$$\lambda = \frac{\beta}{\gamma h} g \tag{2.32}$$

$$\chi = \frac{\tan\phi'}{\gamma h} g \tag{2.33}$$

The solution of Eq.(2.31) can be achieved using Duhamel's theorem, with the condition that the slope is initially at rest and under the reasonable assumption that the soil parameters involved remain unchanged during the slope movements. Application of this theorem leads to the equation:

$$v(t) = \chi \int_{t_s}^{t} [u(\tau) - u_c] \frac{\mathrm{d}\,\bar{v}(t-\tau)}{\mathrm{d}\,t} \mathrm{d}\tau \tag{2.34}$$

where t_s indicates the time at which motion starts, and $\bar{v}$ is the solution to Eq. (2.31) when the term in the square brackets on the right-hand side of this equation is kept at unity at any time.It is easy to show that this latter function is:

$$\bar{v}(t) = \frac{1}{\lambda}\left(1 - e^{-\lambda t}\right) \tag{2.35}$$

After substituting (t-τ) for t in Eq. (2.35) and performing the derivative of $\bar{v}$ with respect to t, Eq. (2.34) takes the following form:

$$v(t) = \chi \int_{t_s}^{t} [u(\tau) - u_c] e^{-\lambda(t-\tau)}\, d\tau \tag{2.36}$$

An analytical solution for $v(t)$ can be obtained either when the function $u(t)$ is defined fitting the piezometric measurements performed directly at the slip surface or when $u(t)$ is calculated (at this surface) using Eqs. (2.17)-(2.23) on the basis of the measurements performed at a piezometer installed above the slip surface. This solution can be put in the form:

$$v(t) = \chi\left\{v_0(t) + \left[\sum_{k=1}^{M} v_k(t)\right] - v_c(t)\right\} \tag{2.37}$$

in which:

$$v_c(t) = \frac{u_c}{\lambda}\left[1 - e^{-\lambda(t-t_S)}\right] \tag{2.38}$$

When the piezometer depth coincides with the failure surface, the expressions of $v_0(t)$ and $v_k(t)$ are respectively:

$$v_0(t) = \frac{A_0}{2\lambda}\left[1 - e^{-\lambda(t-t_S)}\right] \tag{2.39}$$

$$v_k(t) = A_k C + B_k D \tag{2.40}$$

t_s is the time when $SF<1$ and the slope start to move and it could exist more than one value. A_k ,B_k and A_0,are the series amplitudes, expressed by equations (2.11)-(2.16) and:

$$C = \frac{1}{\left(\lambda^2 + \omega_k^2\right)}\left\{\lambda\cos(\omega_k t) + \omega_k \sin(\omega_k t) - \left[\lambda\cos(\omega_k t_s) + \omega_k \sin(\omega_k t_s)\right]e^{-\lambda(t-t_S)}\right\} \tag{2.41}$$

$$D = \frac{1}{\left(\lambda^2 + \omega_k^2\right)}\left\{\lambda\sin(\omega_k t) - \omega_k \cos(\omega_k t) - \left[\lambda\sin(\omega_k t_s) - \omega_k \cos(\omega_k t_s)\right]e^{-\lambda(t-t_S)}\right\} \tag{2.42}$$

Conversely, when the depth of piezometer is located above the failure surface, the expressions of $v_0(t)$ and $v_k(t)$ become respectively:

$$v_0(t) = \frac{A_0}{2}\left\{\left[1 - e^{-\lambda(t-t_S)}\right]\frac{1}{\lambda} - \frac{4}{\pi}\sum_{n=1}^{\infty}\frac{1}{(2n-1)}\frac{L_n}{S_n}\sin\left(\frac{M_n z_w}{H}\right)\right\} \quad (2.43)$$

$$v_k(t) = 2\sum_{n=1}^{\infty}\frac{M_n\theta_k}{1+\theta_k^2 M_n^{\ 4}}(G_n - F_n + E_n)\sin\left[\frac{M_n z_w}{H}\right] \quad (2.44)$$

where M_n is previously reported in the equation (2.20) and:

$$S_n = \lambda - \frac{c_v M_n^{\ 2}}{H^2} \quad (2.45)$$

$$L_n = e^{-M_n^{\ 2} T_V} - e^{\left[-M_n^{\ 2} T_{vs} + \lambda(t_S - t)\right]} \quad (2.46)$$

$$T_{vs} = \frac{c_v t_s}{H^2} \quad (2.47)$$

$$G_n = \frac{L_n}{S_n}\left(B_k - A_k\theta_k M_n^{\ 2}\right) \quad (2.48)$$

$$F_n = C\left(B_k - A_k\theta_k M_n^{\ 2}\right) \quad (2.49)$$

$$E_n = D\left(A_k + B_k\theta_k M_n^{\ 2}\right) \quad (2.50)$$

It should be noted that $v(t)$ has to be calculated when $u(t)$ exceeds u_c. By contrast, if the condition $u < u_c$ persists at any time the slope is stable (i.e., *SF*>1) and hence no slope movement occurs. The time that first yields $u = u_c$ defines the time t_s at which motion starts. Motion stops when v=0. In addition, the positive values of $v(t)$ have to be only considered, because they correspond to slope movements that occur in the downhill direction.

The solution procedure for calculating $v(t)$ is illustrated by the flow chart in Fig. 2.6. After calculated the velocity, the displacement is determined by integration of $v(t)$.

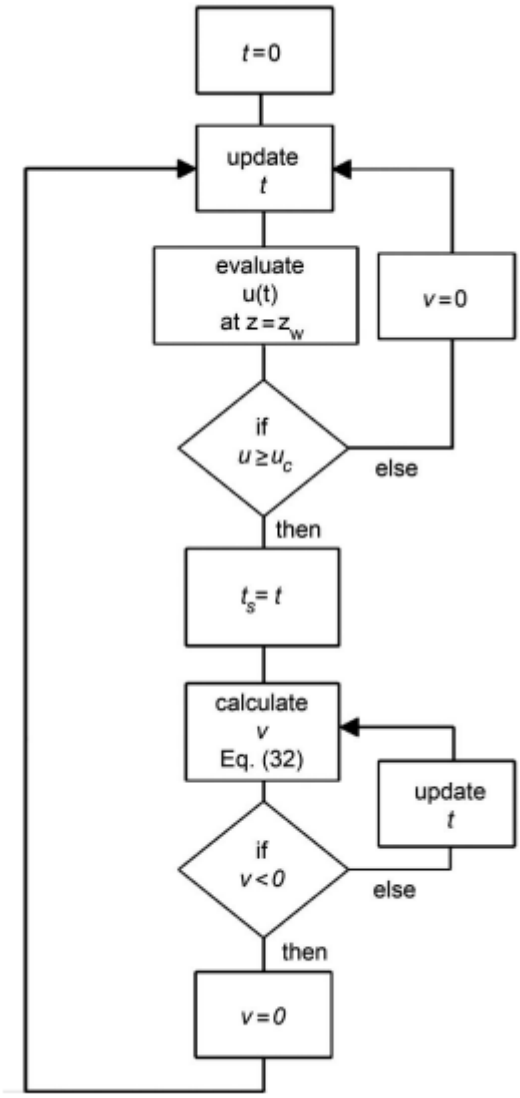

Fig. 2.6- Flowchart illustrating the proposed procedure (Conte & Troncone, 2011)

2.3. Constitutive models used in the finite element analyses

2.3.1. Overview

The soil behaviour is extremely complex: nonlinear, irreversible, anisotropic and time-dependent (in function of loading history). In addition, other factors such as temperature, viscosity, saturation degree and so on, make mathematical modeling very tough. Consequently, the difficulty in using extremely complex models is the determination of a high number of constitutive parameters.

It needs to choose a right compromise between good accuracy and a reasonable number of constitutive parameters for applications.

In the last years, technological developments have provided a great support to elaborate more realistic models based on elasto-plastic formulation.

The finite element method is widely applied in geotechnical engineering and it allows implementing constitutive models more sophisticated.

In the present work the finite element analyses are conducted by means of the code Tochnog (Roddeman, 2013).

2.3.2. The elasto-plastic theory

The formulation establishes that the material strain can be reversible (elastic) and irreversible (plastic). In a certain time this involves that stress and strain depend from the actual loading conditions and from the loading path also.

Essentially, a biunivocal correspondence between stress and strain is not valid, as in elastic behaviour. In particular, the elasto-plastic relationships must be expressed by differential equations, integrated along a loading path (in elastic behaviour the stress state is just function of the initial and the final configuration). In elasto-plasticity, a loading process must be considered incremental, because the superposition principle is inapplicable. In terms of analysis, the calculation time is more costly. In agreement with the main assumption of the elasto-plastic formulation (Hill, 1950), total strain tensor (2.51) and total strain rate tensor (2.52) are composed of two parts: elastic (indicated by apex "*e"*) and plastic (apex "*p"*):

$$\varepsilon_{ij} = \varepsilon_{ij}^{e} + \varepsilon_{ij}^{p} \tag{2.51}$$

$$\dot{\varepsilon}_{ij} = \dot{\varepsilon}_{ij}^{e} + \dot{\varepsilon}_{ij}^{p} \tag{2.52}$$

In this case, elastic and plastic strain is immediately developed. As a result, the time is just an order parameter (Nova, 2002).

The elastic strain rate tensor is related to the effective stress rate tensor by the following equation:

$$\dot{\varepsilon}_{ij}^{\mathrm{e}} = C_{ijhk}^{\mathrm{e}} \dot{\sigma}'_{hk} \tag{2.53}$$

where C_{ijhk}^{e} is the elastic compliance tensor.

Due to symmetry, there are six independent components only. It can be used a compact matrix notation:

$$\underline{\dot{\varepsilon}}^{e} = \underline{\underline{C}}^{e}\,\underline{\dot{\sigma}}' \tag{2.54}$$

where $\underline{\underline{C}}^{e}$ for a linear isotropic material becomes:

$$\underline{\underline{C}}^{e} = \frac{1}{E}\begin{bmatrix} 1 & -\nu & -\nu & & & \\ -\nu & 1 & -\nu & & & \\ -\nu & -\nu & 1 & & & \\ & & & 2\cdot(1+\nu) & & \\ & & & & 2\cdot(1+\nu) & \\ & & & & & 2\cdot(1+\nu) \end{bmatrix} \tag{2.55}$$

Considering the inverse relation of (2.54) and assuming the elastic constitutive matrix as $\underline{\underline{D}}^{e} \equiv \underline{\underline{C}}^{e^{-1}}$, it obtains:

$$\underline{\dot{\sigma}}' = \underline{\underline{D}}^{e}\,\underline{\dot{\varepsilon}}^{e} \tag{2.56}$$

$$\dot{\sigma}'_{hk} = D^{e}_{hkij}\dot{\varepsilon}^{e}_{ij} \tag{2.57}$$

For elastic isotropic material elastic strain rate $\underline{\dot{\varepsilon}}^{e}$ is determined by using (2.54). Plastic strain rate $\underline{\dot{\varepsilon}}^{p}$ is described by means of a yield criterion, a flow rule and a hardening law, which provide existence, direction and module, respectively. The *coaxiality condition* is adopted, i.e. principal directions of stress tensor coincide with those of plastic strain rate tensor.

2.3.3. Yield function

The yield function separates purely elastic from elasto-plastic behaviour. In general, this is a function of effective stress state $\underline{\sigma}'$ and its size can changes in function of the state parameters $\underline{k}$ which can be related to hardening/softening parameters. In case of perfect plasticity $\underline{k}$ is composed of constant parameters.

$$F\left(\underline{\sigma}',\underline{k}\right)=0 \tag{2.58}$$

Following a generic loading path (included in $\underline{k}$ vector), strain can become from elastic to elasto-plastic. In particular, if $F\left(\underline{\sigma}',\underline{k}\right)<0$, strain is elastic, whereas if $F\left(\underline{\sigma}',\underline{k}\right)=0$, strain is elasto-plastic. Lastly, $F\left(\underline{\sigma}',\underline{k}\right)>0$ has no physical sense. In consequence, it is possible to divide the elastic domain in an internal portion inside which there are elastic strains only, and a boundary (elasto-plastic strains), identified by (2.58) and shown in Fig. 2.7.

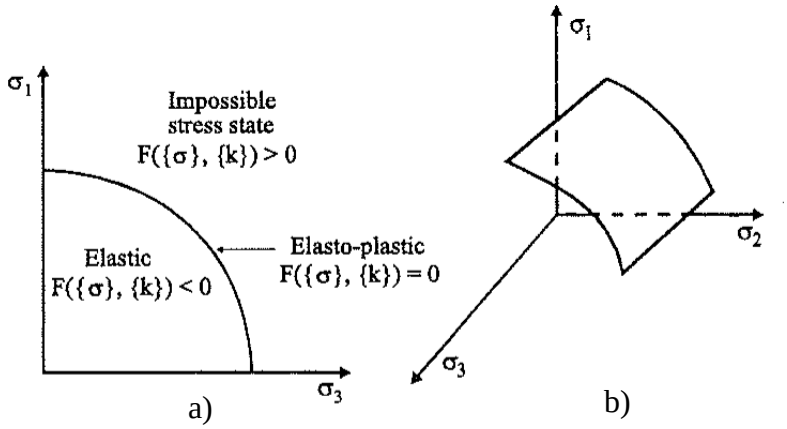

Fig. 2.7 – a) Yield function in plane stress; b) Segment of yield surface (Potts & Zdravkovic, 1999)

2.3.4. Plastic potential function

Direction and verso of incremental plastic strain vector is defined by means of a flow rule. It introduces the *plastic potential P*, such that plastic strain rate is direct along the normal of elastic domain frontier. This involves in Eq. (2.59):

$$\dot{\underline{\varepsilon}}^{P} = \dot{\lambda}\frac{\partial P\left(\underline{\sigma}', \underline{q}\right)}{\partial \underline{\sigma}'} \tag{2.59}$$

The scalar multiplier λ is a plastic multiplier and its variation can be positive, negative or at limit zero (elastic behaviour). It can rewrite (2.59) in the following form, similar to yield criterion in (2.58):

$$P\left(\underline{\sigma}', \underline{q}\right) = 0 \tag{2.60}$$

In a particular case, called *associated flow rule*, the gradient of *P* overlaps with the gradient of *F*:

$$\frac{\partial P\left(\underline{\sigma}', \underline{q}\right)}{\partial \underline{\sigma}'} \equiv \frac{\partial F\left(\underline{\sigma}', \underline{k}\right)}{\partial \underline{\sigma}'} \tag{2.61}$$

That is $P\left(\underline{\sigma}', \underline{q}\right) = F\left(\underline{\sigma}', \underline{k}\right)$ unless a constant. Moreover, $\dot{\underline{\varepsilon}}^{p}$ vector in the principal stress space is normal on the plastic surface. This property is also called *normality condition*. Generally, (2.61) is not valid (*non associated flow rule)*, as shown in Fig. 2.8.

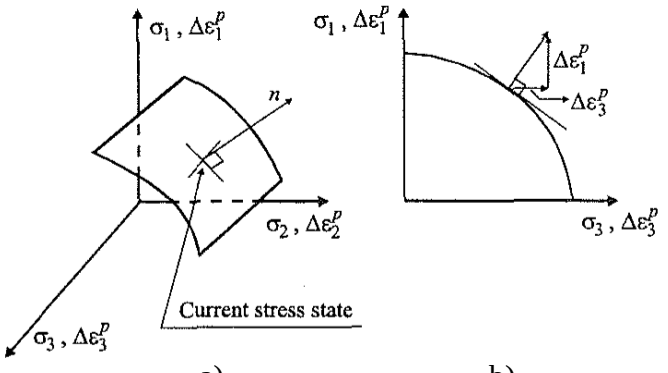

a) b)

Fig. 2.8 – a) Segment of plastic potential surface; b) Plastic potential curve in plane stress state (Potts & Zdravkovic, 1999)

2.3.5. The hardening/softening rules

The hardening/softening rues determine the how the state parameters $\underline{k}$ vary with plastic straining. This leads to quantify the scalar parameter λ in Eq. (2.59) In case of perfectly plastic material, no hardening or softening occurs, therefore, the state parameters $\underline{k}$ are constant. The yield surface can change in size if the material presents a hardening behaviour (expansion) or softening behaviour (contraction). In agreement, it defines the "work hardening" ($W^P>0$) or "work softening" ($W^P<0$) :

$$W^P = \int_{Vol} \underline{\dot{\sigma}}'^T \, \underline{\dot{\varepsilon}}^P dV \tag{2.62}$$

For elasto-perfectly plastic material, the yield surface, identified by (2.58) remains unchanged in size. If the yield surface changes in size but not in position, it comes to *isotropic hardening* , whereas it is called *kinematic hardening* if yield surface moves rigidly in stress space (see Fig. 2.9).

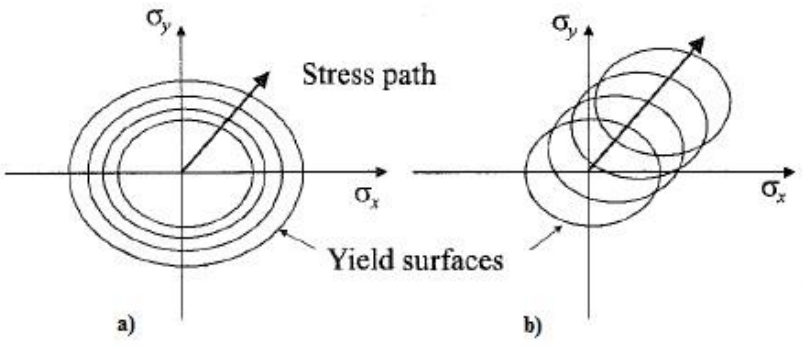

Fig. 2.9 – a) Isotropic hardening b) Kinematic hardening

In general, a yield surface is included or at limit coincident with failure surface. It involves in the following equation:

$$F = F\left(\underline{\sigma}', \underline{k}\right) \leq 0 \tag{2.63}$$

- if $F<0$ or $F=0$ and $dF<0$:

$$\dot{\underline{\varepsilon}} = \dot{\underline{\varepsilon}}^{e} = \underline{\underline{C}}^{e}\,\dot{\underline{\sigma}}' \tag{2.64}$$

- if $F=0$ and $dF=0$:

$$\dot{\underline{\varepsilon}} = \dot{\underline{\varepsilon}}^{e} + \dot{\underline{\varepsilon}}^{p} = \underline{\underline{C}}^{e}\,\dot{\underline{\sigma}}' + \dot{\lambda}\frac{\partial P\left(\underline{\sigma}', \underline{q}\right)}{\partial \underline{\sigma}'} \tag{2.65}$$

According to the principle of effective stresses (Terzaghi, 1936), strain is related to effective stress. Incremental plastic multiplier $\dot{\lambda}$ and $F\left(\underline{\sigma}', \underline{k}\right)$ must satisfy the *Kuhn-Tucker conditions* (2.66) and the *consistency condition* (2.67) for loading and unloading paths:

$$\begin{cases} \dot{\lambda} \geq 0 \\ F\left(\underline{\sigma}', \underline{k}\right) \leq 0 \\ \dot{\lambda} \cdot F\left(\underline{\sigma}', \underline{k}\right) = 0 \end{cases} \tag{2.66}$$

$$\dot{\lambda} \cdot \dot{F} = 0 \tag{2.67}$$

2.3.6. Formulation of the elasto-plastic constitutive matrix

So far, the groundwork of an elasto-plastic model is defined.

The constitutive relation between effective stress rate and strain rate is:

$$\dot{\underline{\sigma}}' = \underline{\underline{D}}^{ep}\,\dot{\underline{\varepsilon}} \tag{2.68}$$

where $\underline{\underline{D}}^{ep}$ is the elasto-plastic constitutive matrix. According to additive decomposition axiom, total strain rate is formed by elastic and plastic part:

$$\dot{\underline{\varepsilon}} = \dot{\underline{\varepsilon}}^{e} + \dot{\underline{\varepsilon}}^{p} \tag{2.69}$$

Therefore, the incremental stress is related to the incremental elastic strain by the elastic constitutive matrix $\underline{\underline{D}}^{e}$, in the form:

$$\dot{\underline{\sigma}}' = \underline{\underline{D}}^{e}\,\dot{\underline{\varepsilon}}^{e} \tag{2.70}$$

Combining (2.65) and (2.66) it gives:

$$\dot{\underline{\sigma}}' = \underline{\underline{D}}^e \left(\dot{\underline{\varepsilon}} - \dot{\underline{\varepsilon}}^p \right) \tag{2.71}$$

in which incremental plastic strain $\dot{\underline{\varepsilon}}^p$ depends from plastic potential $P\left(\underline{\sigma}', \underline{q}\right) = 0$ via the flow rule (2.60). By a series of substitutions, it reaches:

$$\dot{\underline{\sigma}}' = \underline{\underline{D}}^e \left(\dot{\underline{\varepsilon}} - \dot{\lambda} \frac{\partial P\left(\underline{\sigma}', \underline{q}\right)}{\partial \underline{\sigma}'} \right) = \underline{\underline{D}}^e \, \dot{\underline{\varepsilon}} - \dot{\lambda} \underline{\underline{D}}^e \frac{\partial P\left(\underline{\sigma}', \underline{q}\right)}{\partial \underline{\sigma}'} \tag{2.72}$$

When the material is plastic, the stress state must satisfy the yield function $F\left(\underline{\sigma}', \underline{k}\right) = 0$ and appertain at plastic surface $\dot{F}\left(\underline{\sigma}', \underline{k}\right) = 0$:

$$\dot{F}\left(\underline{\sigma}', \underline{k}\right) = \left(\frac{\partial F\left(\underline{\sigma}', \underline{k}\right)}{\partial \underline{\sigma}'} \right)^T \dot{\underline{\sigma}}' + \left(\frac{\partial F\left(\underline{\sigma}', \underline{k}\right)}{\partial \underline{k}} \right)^T \dot{\underline{k}} = 0 \tag{2.73}$$

This equation is known as the *consistency condition*. It can be rewrite to give:

$$\dot{\underline{\sigma}}' = - \frac{\left(\frac{\partial F\left(\underline{\sigma}', \underline{k}\right)}{\partial \underline{k}} \right)^T \dot{\underline{k}}}{\left(\frac{\partial F\left(\underline{\sigma}', \underline{k}\right)}{\partial \underline{\sigma}'} \right)^T} \tag{2.74}$$

Combining (2.72) and (2.74), the incremental plastic multiplier $\dot{\lambda}$ becomes:

$$\dot{\lambda} = \left[\frac{\left(\frac{\partial F\left(\underline{\sigma}', \underline{k}\right)}{\partial \underline{\sigma}'} \right)^T \underline{\underline{D}}^e \, \dot{\underline{\varepsilon}}}{H + \left(\frac{\partial F\left(\underline{\sigma}', \underline{k}\right)}{\partial \underline{\sigma}'} \right)^T \underline{\underline{D}}^e \frac{\partial P\left(\underline{\sigma}', \underline{q}\right)}{\partial \underline{\sigma}'}} \right] \tag{2.75}$$

where:

$$H = \left[-\frac{1}{\dot{\lambda}} \left(\frac{\partial F\left(\underline{\sigma}', \underline{k}\right)}{\partial \underline{k}} \right)^T \dot{\underline{k}} \right] = \left[-\frac{1}{\dot{\lambda}} \left(\frac{\partial F\left(\underline{\sigma}', \underline{k}\right)}{\partial \underline{k}} \right)^T \frac{\partial \underline{k}}{\partial \underline{\varepsilon}^p} \dot{\underline{\varepsilon}}^p \right] \tag{2.76}$$

Substituting (2.75) in (2.72), it obtains:

$$\dot{\underline{\sigma}}' = \underline{\underline{D}}^e \dot{\underline{\varepsilon}} - \frac{\underline{\underline{D}}^e \left(\frac{\partial P(\underline{\sigma}', \underline{q})}{\partial \underline{\sigma}'} \right) \left(\frac{\partial F(\underline{\sigma}', \underline{k})}{\partial \underline{\sigma}'} \right)^T \underline{\underline{D}}^e \dot{\underline{\varepsilon}}}{H + \left(\frac{\partial F(\underline{\sigma}', \underline{k})}{\partial \underline{\sigma}'} \right)^T \underline{\underline{D}}^e \frac{\partial P(\underline{\sigma}', \underline{q})}{\partial \underline{\sigma}'}} = \left\{ \underline{\underline{D}}^e - \frac{\underline{\underline{D}}^e \left(\frac{\partial P(\underline{\sigma}', \underline{q})}{\partial \underline{\sigma}'} \right) \left(\frac{\partial F(\underline{\sigma}', \underline{k})}{\partial \underline{\sigma}'} \right)^T \underline{\underline{D}}^e}{H + \left(\frac{\partial F(\underline{\sigma}', \underline{k})}{\partial \underline{\sigma}'} \right)^T \underline{\underline{D}}^e \left(\frac{\partial P(\underline{\sigma}', \underline{q})}{\partial \underline{\sigma}'} \right)} \right\} \dot{\underline{\varepsilon}} \tag{2.77}$$

The expression of the elasto-plastic constitutive matrix is:

$$\underline{\underline{D}}^{ep} = \left\{ \underline{\underline{D}}^e - \frac{\underline{\underline{D}}^e \left(\frac{\partial P(\underline{\sigma}', \underline{q})}{\partial \underline{\sigma}'} \right) \left(\frac{\partial F(\underline{\sigma}', \underline{k})}{\partial \underline{\sigma}'} \right)^T \underline{\underline{D}}^e}{H + \left(\frac{\partial F(\underline{\sigma}', \underline{k})}{\partial \underline{\sigma}'} \right)^T \underline{\underline{D}}^e \left(\frac{\partial P(\underline{\sigma}', \underline{q})}{\partial \underline{\sigma}'} \right)} \right\} \tag{2.78}$$

$\underline{\underline{D}}^{ep}$ is suitable to describe elasto-plastic behaviour related to H parameter which identifies the type of plasticity, such as: perfect plasticity (H=0) , hardening plasticity (H>0) or softening plasticity (H<0). Generally, $\underline{\underline{D}}^{ep}$ is not a symmetric matrix, unless in case of associated flow rule. As formerly mentioned, for perfectly plasticity $\underline{k}$ is a vector formed by constant parameters, therefore:

$$\left(\frac{\partial F(\underline{\sigma}', \underline{k})}{\partial \underline{k}} \right)^T = \underline{0} \tag{2.79}$$

2.3.7. Mohr-Coulomb model

If the results of laboratory tests are plotted in terms of effective stresses, the Mohr's circles of stress at failure are idealised as shown in Fig.2.10 (Potts & Zdravkovic, 1999a). It is usual to assume that the tangent to failure circles is straight. This line is called Mohr-Coulomb failure criterion, expressed as:

$$\tau_f = c' + \sigma'_{nf} tg\phi' \tag{2.80}$$

where τ_f e σ'_{nf} are the shear and normal effective stresses on the failure plane, respectively. The material parameters are c' (effective cohesion) and ϕ' (angle of shearing resistance).

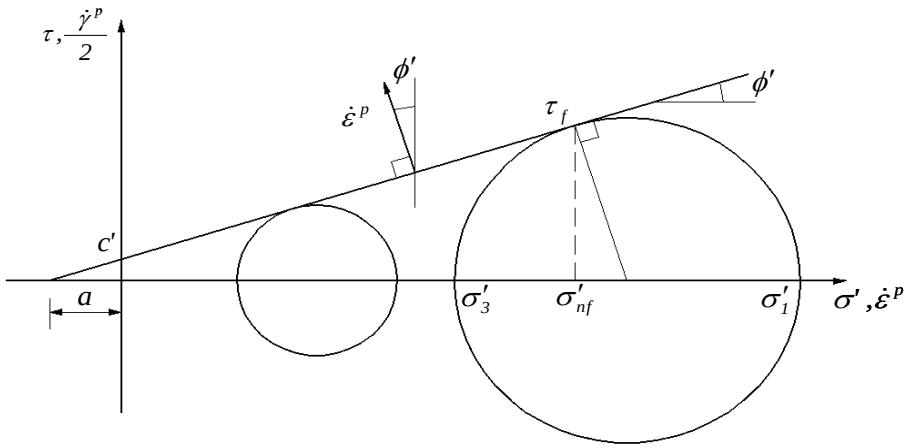

Fig. 2.10 – Mohr's circles of effective stress (Potts & Zdravkovic, 1999a)

The expression of the Mohr-Coulomb yield criterion (2.80) rewrited in terms of principal effective stress becomes:

$$F(\underline{\sigma}', \underline{k}) = (\sigma'_1 - \sigma'_3) - (\sigma'_1 + \sigma'_3) \cdot \sin\phi' - 2 \cdot c' \cdot \cos\phi' \tag{2.81}$$

Eq. (2.81) is referred to plane stress state. In general, Eq. (2.81) is:

$$|\sigma'_i - \sigma'_k| - (\sigma'_i + \sigma'_k) \cdot \sin\phi' - 2 \cdot c' \cdot \cos\phi' \leq 0 \qquad i,k=1,2,3 \tag{2.82}$$

Two illustrations of this criterion are shown in Fig. 2.11.

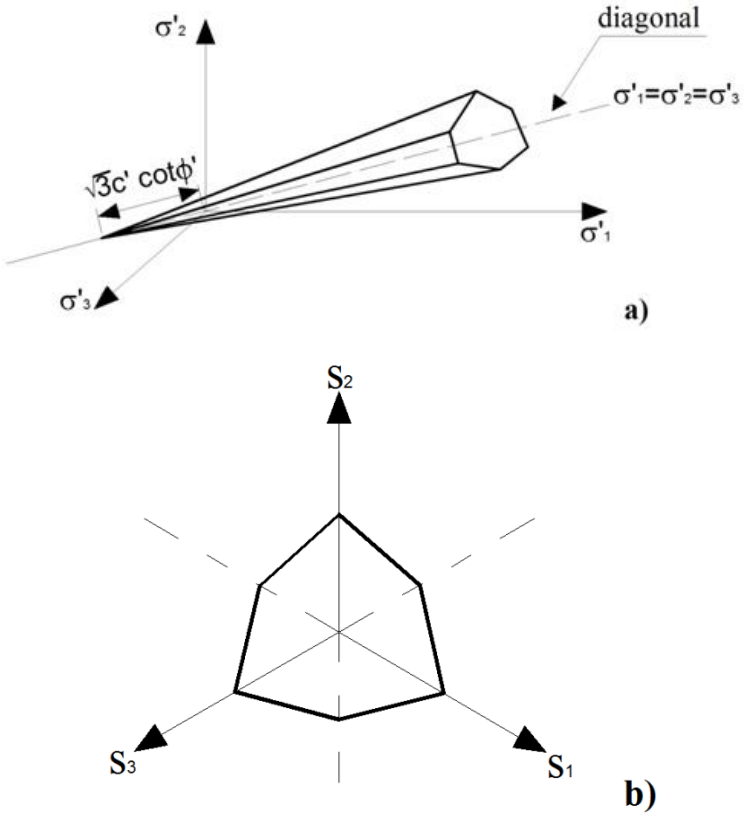

Fig. 2.11 – a) Mohr-Coulomb yield surface in principal stress space
b) Mohr-Coulomb yield surface in deviatoric plane

Inasmuch as the soil cannot sustain traction efforts, the pyramid in Fig.2.11a is cut off according to following conditions:

$$\sigma'_1 \geq 0; \quad \sigma'_2 \geq 0; \quad \sigma'_3 \geq 0 \tag{2.83}$$

Suitably, when it works using the Finite Element Method, it can argue in terms of invariants p', J and ϑ (Potts & Zdravković, 1999a) defined by following relationships.

- *Mean effective stress*

$$p' = \frac{1}{3}(\sigma_1' + \sigma_2' + \sigma_3') \tag{2.84}$$

- *Deviatoric stress*

$$J = \frac{1}{\sqrt{6}}\sqrt{(\sigma_1' - \sigma_2')^2 + (\sigma_2' - \sigma_3')^2 + (\sigma_3' - \sigma_1')^2} \tag{2.85}$$

- *Lode's angle*

$$\vartheta = \arctan\left[\frac{1}{\sqrt{3}}\left(2\frac{(\sigma_2' - \sigma_3')}{(\sigma_1' - \sigma_3')} - 1\right)\right] \tag{2.86}$$

The geometric meaning of the invariants is shown in Fig. 2.12 (adapted by Potts & Zdravkovic, 1999a):

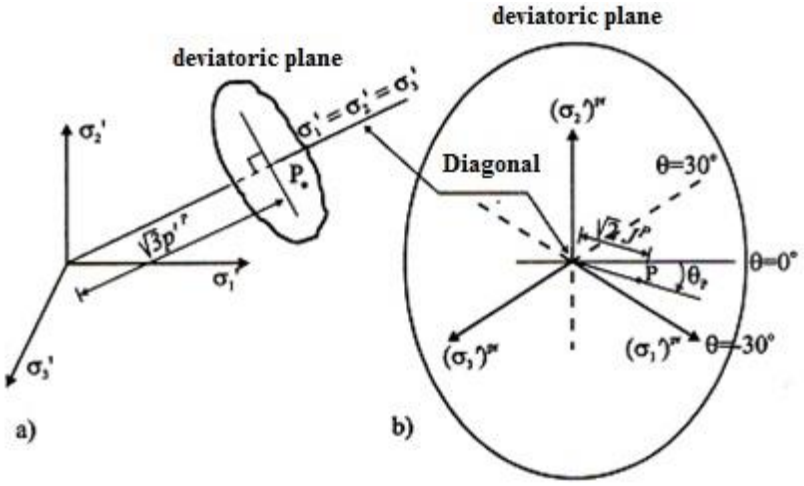

Fig. 2.12 – Geometric meaning of p', J, ϑ invariants in principal stress space

In case of $\sigma_1'^p \geq \sigma_2'^p \geq \sigma_3'^p$ (Fig.2.12b), point P is restricted to move between $\vartheta = -30°$ and $\vartheta = +30°$.

These limits correspond to triaxial compression $\left(\sigma_1'^p \geq \sigma_2'^p = \sigma_3'^p\right)$ and triaxial extension $\left(\sigma_1'^p = \sigma_2'^p \geq \sigma_3'^p\right)$ respectively.

The principal stress state can be expressed in terms of invariants p', J and ϑ:

$$\begin{Bmatrix}\sigma'_1\\ \sigma'_2\\ \sigma'_3\end{Bmatrix} = p'\begin{Bmatrix}1\\1\\1\end{Bmatrix} + \frac{2}{\sqrt{3}}J\begin{Bmatrix}\sin\left(\vartheta+\frac{2\pi}{3}\right)\\ \sin\vartheta\\ \sin\left(\vartheta-\frac{2\pi}{3}\right)\end{Bmatrix} \tag{2.87}$$

Similarly, the yield function F in terms of invariants becomes:

$$F(\underline{\sigma}', \underline{k}) = J - \left(\frac{c'}{\tan\phi'} + p'\right)g(\vartheta) = 0 \tag{2.88}$$

where:

$$g(\vartheta) = \frac{\sin\phi'}{\cos\vartheta + \frac{\sin\vartheta\sin\phi'}{\sqrt{3}}} \tag{2.89}$$

For associate flow rule (2.61) and perfect plasticity the vector $\underline{k} = \{c', \phi'\}^T$ is composed of constant parameters, i.e. they not depend of plastic strain. As shown in Fig.2.10, the plastic strain increment vector is inclined at an angle ϕ' to the vertical and indicates negative direct plastic strains. This in turn results in a dilatant plastic volumetric strain. For this situation the angle of dilation, ψ, is:

$$\psi = sin^{-1}\left(-\frac{\dot{\varepsilon}_1^P + \dot{\varepsilon}_3^P}{\dot{\varepsilon}_1^P - \dot{\varepsilon}_3^P}\right) \tag{2.90}$$

Fig. 2.13 illustrates the angle of dilation in function of plastic strain rates.

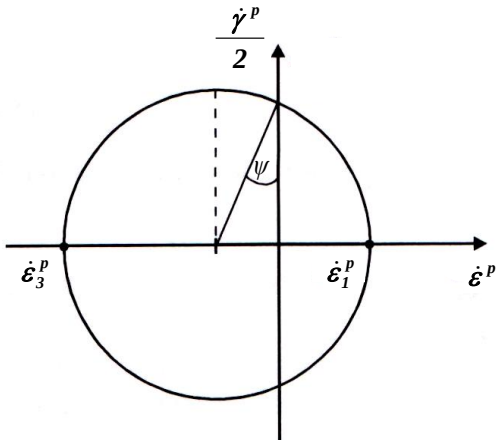

Fig. 2.13 – Mohr's circle of plastic strain (adapted by Potts & Zdravkovic, 1999a).

The volumetric change of soil is controlled by the dilation angle (Rowe,1962). According to (2.61), for associated flow rule, ψ is equal to ϕ' and it can be verified by these relations:

$$\dot{\varepsilon}_1^P = \dot{\lambda}\frac{\partial P(\underline{\sigma}',\underline{q})}{\partial \sigma_1'} = \dot{\lambda}\frac{\partial F(\underline{\sigma}',\underline{k})}{\partial \sigma_1'} \;;\; \dot{\varepsilon}_3^P = \dot{\lambda}\frac{\partial P(\underline{\sigma}',\underline{q})}{\partial \sigma_3'} = \dot{\lambda}\frac{\partial F(\underline{\sigma}',\underline{k})}{\partial \sigma_3'} \quad (2.91)$$

However, real behaviour of soils is not in agreement with (2.61). In fact, experimental results show that volumetric variation of soils is smaller than that obtained in associated flow condition. As a result, it can affirm that:

$$\psi << \phi' \quad (2.92)$$

For example, for normal consolidated clay $\psi = 0°$, whereas $\phi' = 20° \div 30°$. Furthermore, for dense sands, ψ is of order of 10° and ϕ' can be higher than 40° (Nova, 2002). Another expression of the plastic potential *P* can be derived in function of the dilatancy angle and it is valid for non-associated flow rule:

$$P(\underline{\sigma}',\underline{q}) = J - (a_{pp} + p')\; g_{pp}(\vartheta) = 0 \quad (2.93)$$

$$a_{pp} = \left(\frac{c'}{\tan\phi'} + p_c'\right)\frac{g(\vartheta_c)}{g_{pp}(\vartheta_c)} - p_c' \quad (2.94)$$

$$g_{PP}(\vartheta) = \frac{\sin\psi}{\cos\vartheta + \frac{\sin\vartheta\sin\psi}{\sqrt{3}}} \quad (2.95)$$

where:

p_c', J_c and ϑ_c are the invariants of current stress state.

a_{pp} is the distance between the plastic potential surface and the origin of the effective principal stress space, as shown in Fig. 2.14.

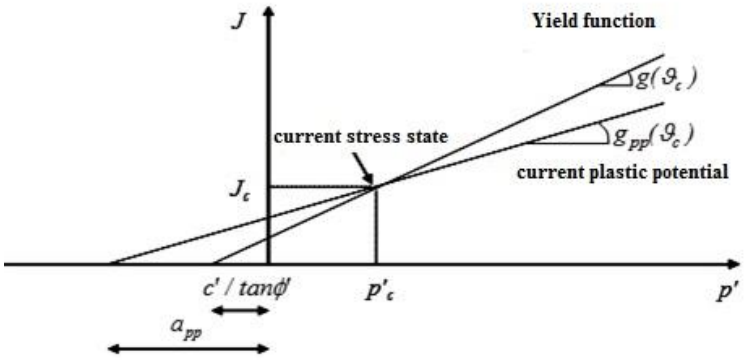

Fig. 2.14 – Relationship between yield and plastic potential functions (adapted by Potts & Zdravkovic, 1999)

Rewriting Eq. (2.93), it becomes:

$$P(\underline{\sigma}', \underline{q}) = J - \left[\left(\frac{c'}{\tan\phi'} + p'_c \right) \frac{g(\vartheta_c)}{g_{pp}(\vartheta_c)} - p'_c + p' \right] g_{pp}(\vartheta) = 0 \qquad (2.96)$$

The yield function does not change in p'- J - ϑ space, whereas the plastic potential surface changes in function of the current stress state. If $\psi = \phi'$, (2.96) coincides with (2.88). This particular case is valid for undrained condition and the dilatancy angle is nil. For non-associated flow rule $\psi < \phi'$, the elasto-plastic matrix $\underline{\underline{D}}^{ep}$ is defined by the partial derivatives of yield function and plastic potential:

$$\frac{\partial F(\underline{\sigma}', \underline{k})}{\partial \underline{\sigma}'} = \frac{\partial F(\underline{\sigma}', \underline{k})}{\partial p'} \frac{\partial p'}{\partial \underline{\sigma}'} + \frac{\partial F(\underline{\sigma}', \underline{k})}{\partial J} \frac{\partial J}{\partial \underline{\sigma}'} + \frac{\partial F(\underline{\sigma}', \underline{k})}{\partial \vartheta} \frac{\partial \vartheta}{\partial \underline{\sigma}'} \qquad (2.97)$$

$$\frac{\partial P(\underline{\sigma}', \underline{q})}{\partial \underline{\sigma}'} = \frac{\partial P(\underline{\sigma}', \underline{q})}{\partial p'} \frac{\partial p'}{\partial \underline{\sigma}'} + \frac{\partial P(\underline{\sigma}', \underline{q})}{\partial J} \frac{\partial J}{\partial \underline{\sigma}'} + \frac{\partial P(\underline{\sigma}', \underline{q})}{\partial \vartheta} \frac{\partial \vartheta}{\partial \underline{\sigma}'} \qquad (2.98)$$

where:

$$\frac{\partial F(\underline{\sigma}', \underline{k})}{\partial p'} = -g(\vartheta); \qquad \frac{\partial F(\underline{\sigma}', \underline{k})}{\partial J} = 1 \qquad (2.99)$$

$$\frac{\partial F(\underline{\sigma}', \underline{q})}{\partial \vartheta} = \left(\frac{c'}{\tan\phi'} + p' \right) \frac{\sin\phi'}{\left(\cos\vartheta + \frac{\sin\vartheta \sin\phi'}{\sqrt{3}} \right)^2} \left(\sin\vartheta - \frac{\cos\vartheta \sin\phi'}{\sqrt{3}} \right) \qquad (2.100)$$

$$\frac{\partial P(\underline{\sigma}', \underline{q})}{\partial p'} = -g_{pp}(\vartheta); \qquad \frac{\partial P(\underline{\sigma}', \underline{q})}{\partial J} = 1 \tag{2.101}$$

$$\frac{\partial P(\underline{\sigma}', \underline{q})}{\partial \vartheta} = (a_{pp} + p') \frac{\sin\psi}{\left(\cos\vartheta + \frac{\sin\vartheta\sin\psi}{\sqrt{3}}\right)^2} \left(\sin\vartheta - \frac{\cos\vartheta\sin\psi}{\sqrt{3}}\right) \tag{2.102}$$

The terms $\frac{\partial p'}{\partial \underline{\sigma}'}$, $\frac{\partial J}{\partial \underline{\sigma}'}$ and $\frac{\partial \vartheta}{\partial \underline{\sigma}'}$ are model-independent and listed below:

- *Mean effective stress*

$$p' = \frac{1}{3}(\sigma_1' + \sigma_2' + \sigma_3') = \frac{1}{3}(\sigma_x' + \sigma_y' + \sigma_z') \tag{2.103}$$

- *Deviatoric stress*

$$J = \frac{1}{\sqrt{6}} \sqrt{(\sigma_x' - \sigma_y')^2 + (\sigma_x' - \sigma_z')^2 + (\sigma_y' - \sigma_z')^2 + \tau_{xy}^2 + \tau_{zx}^2 + \tau_{yz}^2} \tag{2.104}$$

- *Lode's angle*

$$\vartheta = \arctan\left[\frac{1}{\sqrt{3}}\left(2\frac{(\sigma_2' - \sigma_3')}{(\sigma_1' - \sigma_3')} - 1\right)\right] = -\frac{1}{3}\arcsin\left(\frac{3\sqrt{3}}{2}\frac{\det s}{J^3}\right) \tag{2.105}$$

where:

$$det\,\underline{\underline{s}} = \begin{vmatrix} \sigma_x' - p' & \tau_{xy} & \tau_{xz} \\ \tau_{yx} & \sigma_y' - p' & \tau_{yz} \\ \tau_{zx} & \tau_{zy} & \sigma_z' - p' \end{vmatrix} \tag{2.106}$$

$$\begin{aligned} \det\underline{\underline{s}} = {} & (\sigma_x' - p')(\sigma_y' - p')(\sigma_z' - p') - (\sigma_x' - p')\tau_{yz}^2 + \\ & - (\sigma_y' - p')\tau_{zx}^2 - (\sigma_z' - p')\tau_{xy}^2 + 2\tau_{xy}\tau_{yz}\tau_{zx} \end{aligned} \tag{2.107}$$

therefore:

$$\frac{\partial \vartheta}{\partial \underline{\sigma}'} = \frac{\sqrt{3}}{2\cos(3\vartheta)J^3}\left[\frac{det\,\underline{\underline{s}}}{J}\left(\frac{\partial J}{\partial \sigma'}\right) - \frac{\partial(det\,\underline{\underline{s}})}{\partial \sigma'}\right] \tag{2.108}$$

For non-associated flow rule and plane stress, the expression of P is similar to (2.81):

$$P(\underline{\sigma}', \underline{q}) = \frac{1}{2}(\sigma_1' - \sigma_3') - \frac{1}{2}(\sigma_1' + \sigma_3')\sin\psi \tag{2.109}$$

2.3.8. The elasto-viscoplastic model

Likewise (2.52), assuming small strains, the total strain rate tensor $\dot{\varepsilon}_{ij}$ for an elasto–viscoplastic material can be additively decomposed into an elastic component $\dot{\varepsilon}_{ij}^{\mathrm{e}}$ and a viscoplastic component $\dot{\varepsilon}_{ij}^{\mathrm{vp}}$ as follows:

$$\dot{\varepsilon}_{ij} = \dot{\varepsilon}_{ij}^{\mathrm{e}} + \dot{\varepsilon}_{ij}^{vp} \tag{2.110}$$

The tensor $\dot{\varepsilon}_{ij}^{\mathrm{e}}$ was already defined in (2.53) as:

$$\dot{\varepsilon}_{ij}^{\mathrm{el}} = C_{ijhk}^{\mathrm{el}}\, \dot{\sigma}'_{hk} \tag{2.53}$$

where $\dot{\sigma}'_{hk}$ is the effective stress rate tensor, and C_{ijhk}^{el} is the elastic compliance tensor that is independent on time. According to Perzyna (1963), the viscoplastic strain rate tensor is expressed as:

$$\dot{\varepsilon}_{ij}^{\mathrm{vp}} = \Phi(F)\, m_{ij} \tag{2.111}$$

where Φ is the viscous nucleus that depends on the yield function F, and m_{ij} is the gradient to the plastic potential function P:

$$m_{ij} = \frac{\partial P}{\partial \sigma'_{ij}} \tag{2.112}$$

The gradient of P defines the direction of the viscoplastic strain rate tensor, and the yield function influences the modulus of this tensor by means of Φ.

The choice of the viscous nucleus Φ is crucial for describing reliably the time-dependent behaviour of the material. In this connection, Di Prisco and Imposimato (2002, 2003) proposed the following relationship for Φ:

$$\Phi\left(p', F\right) = p' \cdot \widehat{\Phi}(F) = \bar{\gamma} \cdot p' \cdot e^{\bar{\alpha} F} \tag{2.113}$$

where $\bar{\gamma}$ and $\bar{\alpha}$ are constitutive parameters and p' is the mean effective stress.

Through (2.111) it has been introduced the flow rule, without need to use consistency condition as incremental formulation. In particular, the viscoplastic strain rate is directly proportional with the viscous nucleus. In this model, the yield function can be positive also, or rather, stress state can be out of the yield surface. Moreover, the viscous nucleus is a controller parameter of the soil mechanic response in function of the time and it is always positive even if $F<0$. The Eq. (2.111) is easy to implement in a finite element code and capable to well reproduce experimental evidence (di Prisco e Imposimato, 1996). In addition, Eq. (2.110) in conjunction with Eq. (2.113) allows the effectively occurrence of viscoplastic strains under constant effective stress. The parameter $\bar{\gamma}$ significantly influences the strain rate and consequently the rapidity with which strain occurs owing to a given stress increment. In particular, strain rate increases with increasing the value of $\bar{\gamma}$. The values of $\bar{\alpha}$ and $\bar{\gamma}$ are generally determined by matching the experimental results from specific creep tests with those obtained from numerical analysis simulating numerically these tests. Considering that the viscous parameters from laboratory tests can strongly differ from those obtained from back-analysis of observed landslide velocity (Van Asch et al., 2007), in the present study the value of $\bar{\gamma}$ was back-calculated on the basis of field measurements of the displacements experienced by the landslide body, whereas a constant value of $\bar{\alpha}$=61 (di Prisco and Imposimato, 1996; Troncone, 2005; Conte et al., 2010) was assumed in all the analyses performed for the sake of simplicity. In other words, in this study it is assumed that the viscous behaviour of the soil is essentially controlled by the

parameter $\bar{\gamma}$. This latter takes into account rapidity to achieve asymptotic value of deformation, as illustrated in Fig. 2.15. Based on the value of $\bar{\gamma}$, initial slope of the curve increases or decreases directly, following (2.111). As limit $\bar{\gamma} \to +\infty$ it reaches $\Delta\varepsilon_{ij}^{p}$. If the viscoplastic strain is assumed to increase only when the state of stress is outside the yield function, i.e. F>0, it is demonstrated by Di Prisco and Imposimato (1996) that:

$$\int_0^{+\infty} \dot{\varepsilon}_{ij}^{vp}\, dt = \Delta\varepsilon_{ij}^{p} \tag{2.114}$$

where $\Delta\varepsilon_{ij}^{p}$ is the plastic strain increment tensor. In other words, in this case the viscoplasticity can be seen as an extension of incremental plasticity.

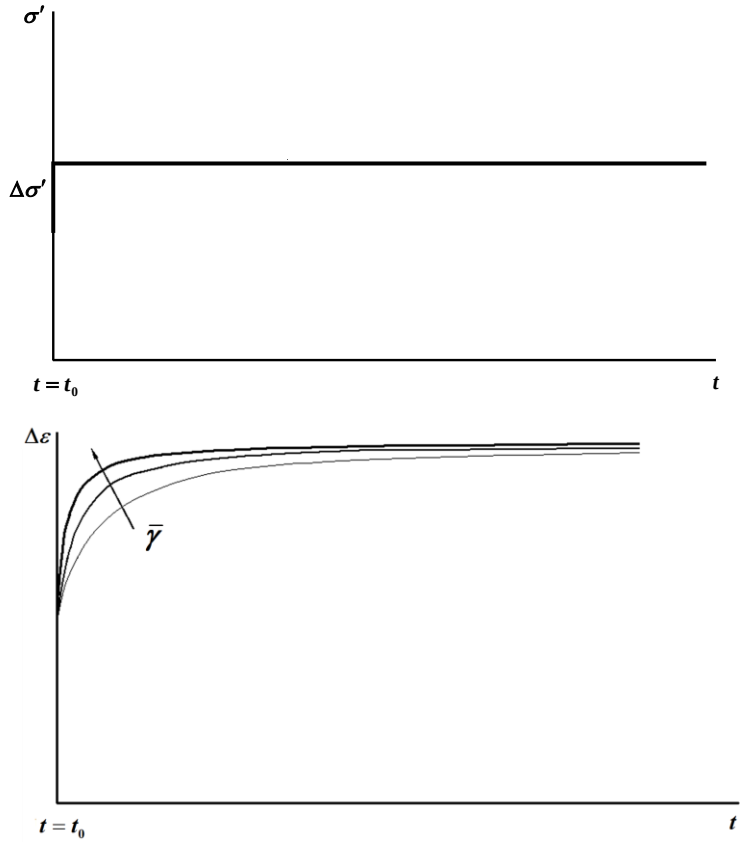

Fig. 2.15 – Incremental strain due to incremental effective stress, in function of $\bar{\gamma}$ variations (Di Prisco & Imposimato, 1996)

Replacing $\dot{\varepsilon}_{ij}^{vp}$ in (2.114), with (2.111) and (2.113), it obtains:

$$\lim_{t\to+\infty}\int_{0^+}^{t}\dot{\varepsilon}_{ij}^{vp}(\tau)d\tau=\lim_{t\to+\infty}\int_{0^+}^{t}p'\cdot\hat{\Phi}(F)\cdot m_{ij}d\tau=+\infty \tag{2.115}$$

As a result, plastic strain tends to infinite theoretically, with increasing of *F*. In order to overcome this disadvantage, di Prisco and Imposimato (1996, 2002) propose that a maximum value of 3 should be assumed for the product $\bar{\alpha}F$ to prevent the exponent in Eq. (2.113) becomes excessively large.

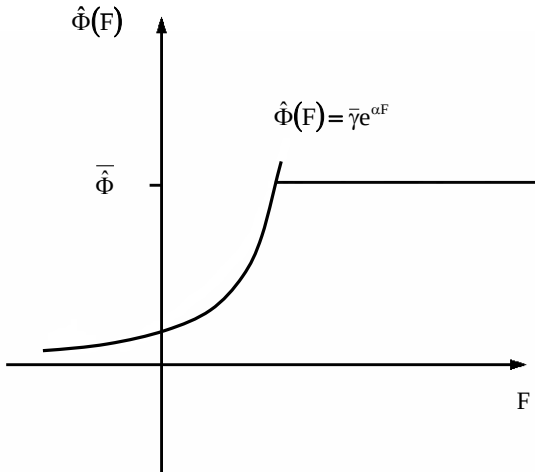

Fig. 2.16 – Viscous nucleus function with upper-bound (Di Prisco & Imposimato, 2002)

It is worth noting that for active slow-moving landslides the soil in the shear zone is described by ϕ' which is the friction angle at residual, ϕ'_r, c' generally negligible and ψ null. The described constitutive model therefore requires few soil parameters as input data, most of which can be readily obtained by conventional geotechnical tests. Specifically, the required parameters are Young's modulus E', Poisson's ratio ν', the residual friction angle, ϕ'_r, and the viscous parameter $\bar{\gamma}$. This is a significant advantage of the present model, especially when there is a lack of specific experimental data. In these circumstances, the use of more sophisticated constitutive models, which involve a greater number of parameters may not be fully justified.

Chapter 3
Case histories

3.1. Overview

In this chapter, the simplified method proposed by Conte & Troncone (see §2.2.) and the finite element approach described in the previous chapter are applied to three case studies: The Vallcebre landslide (Corominas et al., 2005), the Fosso San Martino landslide (Bertini et al., 1984) and the Steinernase landslide (Laloui et al., 2009).

These landslides are active landslides that involve essentially clayey soils and move with low displacement rate. The movements are controlled by the groundwater level fluctuations and deformations are essentially concentrated in distinct shear zones. In addition, in all these landslides, an evident synchronism was observed between groundwater fluctuations and displacement rate. In other words, the response of the landslide body to groundwater fluctuations can be considered immediate. Location and thickness of the shear zones are established from the inclinometer profiles which also document the progress of horizontal displacement with time at different locations. Groundwater level measurements are also available for a sufficiently long period of observation.

The primary objective of this analysis is to assess the capability of the proposed approaches of capturing the main features of the landslide kinematics, and obtaining representative values of some constitutive parameters (in particular,

the viscous parameters β, for simplified model, and $\bar{\gamma}$ for the finite element approach) the experimental evaluation of which is not a simple operation.

The finite element analyses are performed by the finite element code Tochnog (Roddeman, 2013) in which the constitutive model described in the previous section is implemented. These analyses also accounted for the effect of hydro-mechanical coupling. The mesh adopted in calculations consists of triangular elements with three nodes and one Gauss point (CST element). Triangular elements with three nodes and four Gauss points and triangular elements with six nodes and four Gauss points were also used. However, the differences in terms of results were not significant with respect to those obtained using the CST elements. Therefore, the triangular elements were not used in the analyses due to the higher computational costs required. The base of the mesh is assumed to be fully impervious and fixed, and the lateral sides are constrained by vertical rollers. A hydraulic head is also imposed at the lateral boundaries. This head is governed by the measurements performed at the piezometer close to the upstream boundary or by the water level of a stream at the foot of the slope. Considering the uncertainties for defining the geologic history of the site and the lack of specific geotechnical data, the initial stress state within the slope is reproduced by increasing progressively the gravity acceleration up to 9.81 m/s^2 (gravity loading) under the assumption that the soil in the shear zone behaves as an elastic-perfectly plastic material with Mohr–Coulomb failure criterion.

The behaviour of the other involved soils is assumed elastic, for the sake of simplicity. At the end of the gravity loading, the associated displacements and strains are reset to zero. Then, the groundwater fluctuations measured at the piezometers installed in the slope are imposed to calculate the associated movement of the landslide. Considering that in all the case studies analysed the water table was close to the ground surface, the assumption of completely saturated soil is made. In addition, for each case study considered, a part of the soil parameters used in the analysis derives from the field and laboratory tests conducted in the original works (Bertini et al., 1984; Corominas et al., 2005; Laloui et al., 2009). The parameters which cannot be found in these works are evaluated in the present study by matching the available monitoring data with those obtained from the numerical simulations. The resulting parameters from this calibration could be used to predict the future movements of the landslide body owing to expected groundwater fluctuations.

3.2. The Vallcebre landslide

The Vallcebre landslide is a slow-moving translational slide affecting an area of about 0.8 km^2 in the Eastern Pyrenees, 140 km north of Barcelona in Spain (Corominas et al., 2005).

Fig.3.1 - The Vallcebre landslide (Corominas et al., 2005)

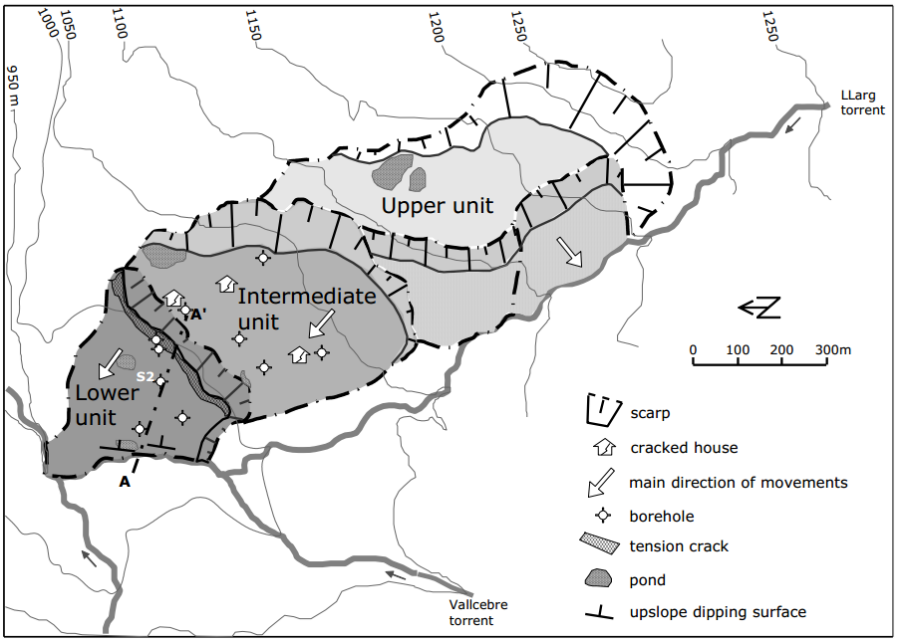

Fig.3.2 – Geomorphology map of the Vallcebre landslide (Corominas et al., 2005)

The average slope of the landslide is about 10°. Fig. 3.3 shows a geological cross-section of the slope where two slide units are indicated: the intermediate unit and the lower unit. The subsoil of the lower unit consists of a thick layer of clayey siltstone with inclusions of gypsum and fissured shale resting on a formation of limestone (bedrock). Gypsum is affected by solution processes which cause the formation of fissures and pipes. A layer of fissured shale is interbedded between the layer of clayey siltstone and the bedrock. The thickness of this latter layer is about 5 m. A similar stratigraphic profile was found for the intermediate unit which is however covered by a layer of colluvial debris, unlike the lower unit. A complete description of the site from a geological viewpoint can be found in Corominas et al. (2005).

The Vallcebre landslide was monitored by installing a significant number of piezometers, inclinometers and wire extensometers. Systematic measurements of groundwater level and displacement of the landslide body were performed since November 1996. The monitoring data showed that there is a close relationship among rainfall, groundwater fluctuations and displacement rate (Fig.3.4). This should be ascribed to the presence of some preferential drainage ways (owing to the fissures and pipes in the upper soil layers) which make the response of the slope to rain infiltration practically immediate (Corominas et al., 2005). The thickness of the lower slide unit ranges from 10 to 15 m, whereas that of the intermediate unit reaches about 34 m. Displacement occurs in a shear zone which largely develops in the layer of fissured shale (Fig.3.3).

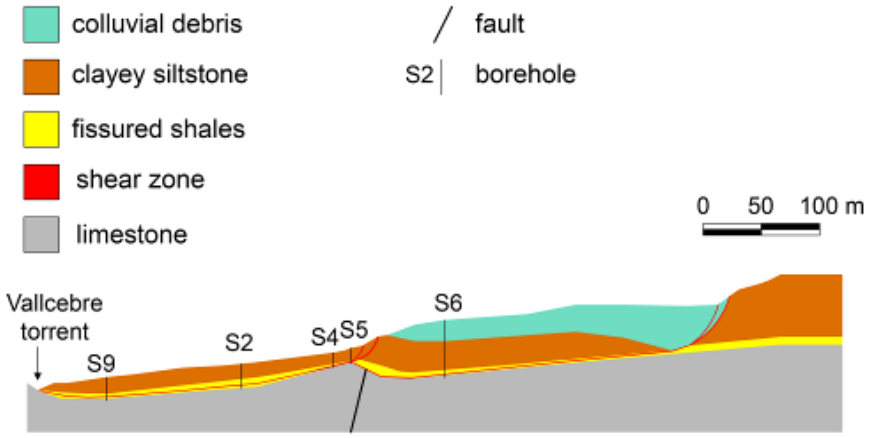

Fig.3.3 - Main section of Vallcebre landslide (Conte et al., 2014)

Deformation of the upper layers of clayey siltstone and colluvial debris is negligible. The available piezometric measurements are plotted in Fig.3.4.

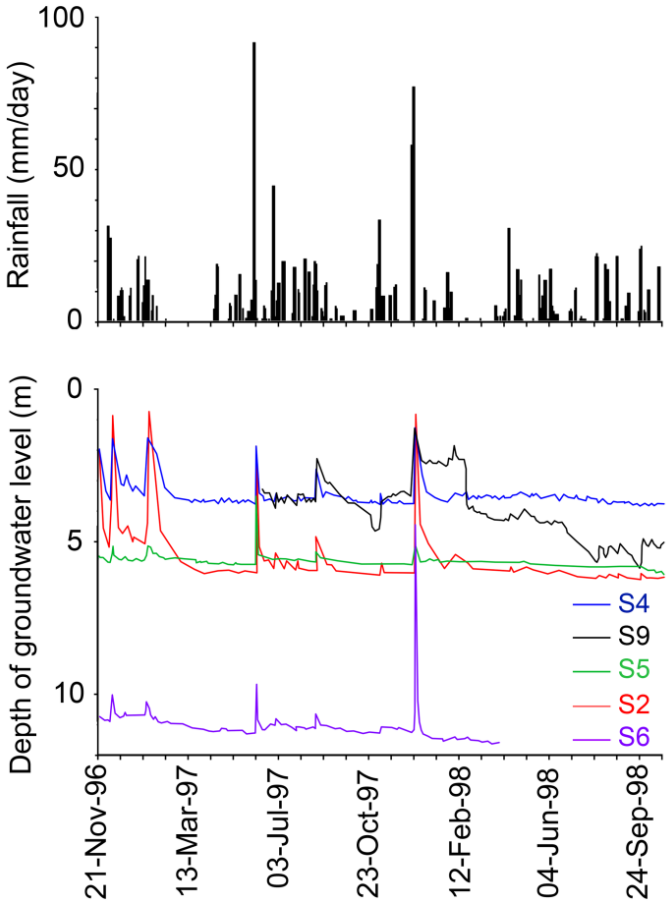

Fig.3.4 - Rainfall and piezometric measurements (Conte et al., 2014)

These measurements are used in the present study as input for predicting the mobility of the Vallcebre landslide. Some direct shear tests were performed by Corominas et al. (2005) on pre-existing shear surfaces observed in the fissured shale, from which a friction angle of 7.8° and an effective cohesion equal to zero were obtained. These parameters should characterize the residual shear strength of the fissured shale. In addition, it can be assumed that the residual friction angle of the clayey siltstone is 14.7° and the cohesion is nil (Corominas et al., 2005). The unit weight, γ, and the hydraulic conductivity, k, of the soils range from 20 to 22 kN/m^3, and from 10^{-9} to 10^{-11} m/s, respectively.

3.2.1. Simplified analysis

Referring to the scheme shown in Fig. 3.5, the geometric data used in the analysis are shown in Table 3.1. In the same table, the geotechnical parameters are also indicated.

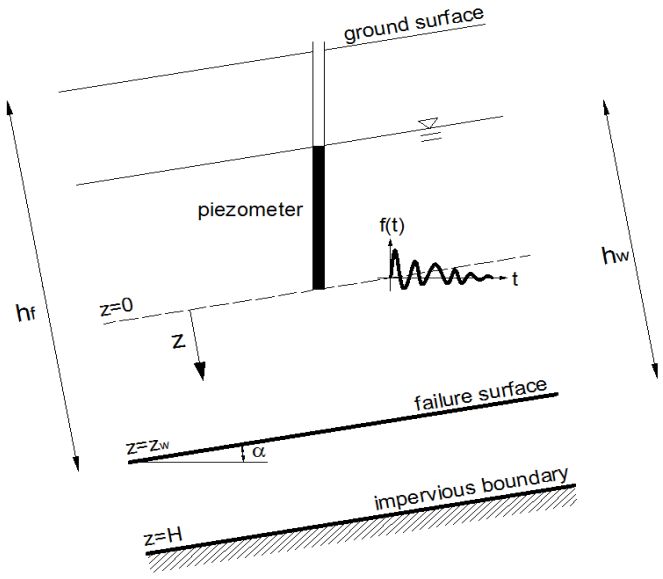

Fig. 3.5 – Schematic representation of an infinite slope with an indication of some geometric parameters (modified from Conte & Troncone, 2011)

Considering the difficulties to obtain experimental values of β and c_v, these parameters are estimated by matching the available measurements with the theoretical results provided by the present method. The best agreement between measured and calculated results is achieved using c_v=5 m^2/day and β=7.7·10^7 kN·day/m^3.

GEOMETRIC DATA					
h_f (m)	z_w (m)	h_w (m)	H (m)	α (°)	L_{ref} (m)
14.77	6.2	8.59	6.2	10	6.28
GEOTECHNICAL PARAMETERS					
γ (kN/m^3)	c' (kPa)	ϕ'_r (°)	c_v (m^2/day)	β (kN·day/m^3)	
21	0	13.7	5	7.7·10^7	

Tab. 3.1 – Data used in the analysis

The groundwater level variations measured at a given piezometers located above the slip surface are the remaining input data. In order to use the simplified method by Conte & Troncone (2011), the function expressing these latter recordings, has to be decomposed in Fourier series (five hundreds harmonic components are considered for this case study). In addition, L_{ref} is a reference level which coincides with the minimum piezometric level recorded. A water flow parallel to the slope surface is assumed, and an impervious boundary is imposed at the bedrock. Under these assumptions, the pore water pressure changes at the slip surface can be evaluated using the analytical solution described in the previous chapter. As previously said, Corominas et al. (2005) provide values of ϕ'_r=7.8° and c'_r=0 kPa. However, using these parameters and along with the infinitive slope model a value of the safety factor *SF*=0.57 is obtained. In view of this result, the analysis is performed imposing *SF*=1 in Eq. (2.1),so that an operative value of the shear strength angle ϕ'**=1**3.7°

is obtained, as already indicated in Table 3.1. The borehole S2 is considered in this analysis as representative of the lower landslide unit (Fig.3.3), which is characterized by a higher mobility than the other landslide units. The following figures show the results in terms of pore pressure changes at the failure surface $z=z_w$, safety factor, measured and calculated landslide velocity and the associated displacement with time.

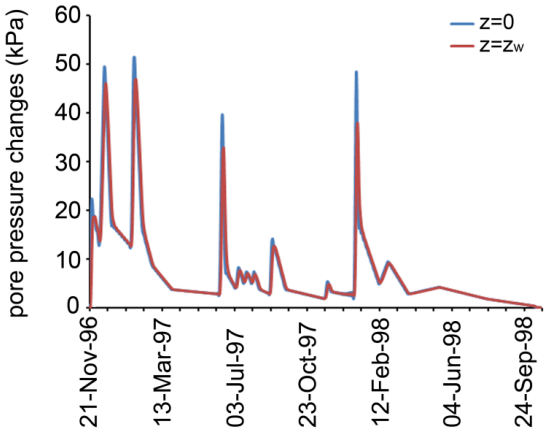

Fig. 3.6 – Pore pressure changes at piezometer S2 (z=0) and at the failure surface ($z=z_w$)

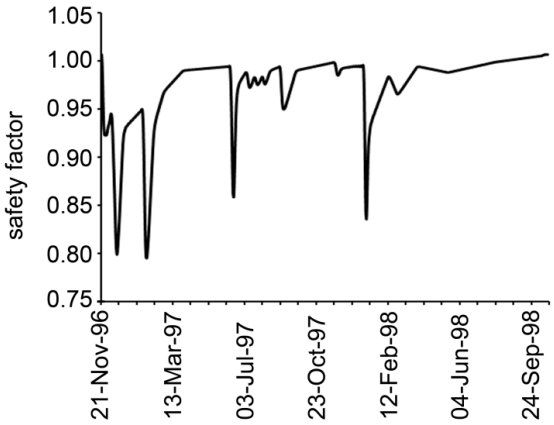

Fig. 3.7 – Safety factor versus time

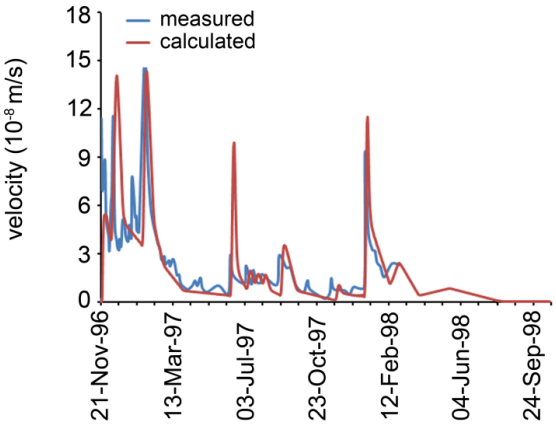

Fig. 3.8 – Comparison between measured and calculated velocity

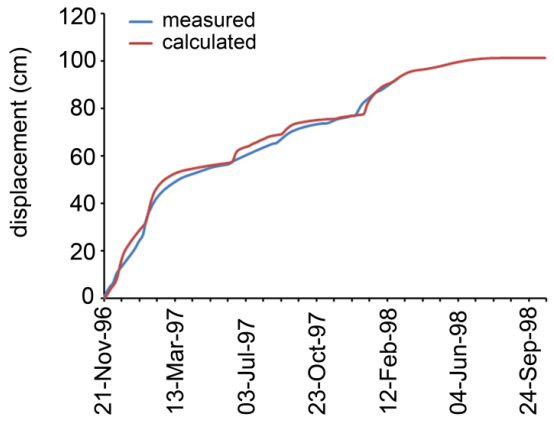

Fig. 3.9 – Comparison between measured and calculated displacement

As it can be observed from Figs. 3.8 and 3.9, a good agreement between observation and prediction is attained.

3.2.2. Finite Element Analysis

In the finite element analysis, the elasto-viscoplastic model is used. This requires additional constitutive parameters (i.e., the elastic parameters E' and v', and the viscous parameter $\bar{\gamma}$) with respect to those indicated in Table 3.1. Considering that these parameters are not available, they are evaluated by matching the measured landslide displacements to those calculated using the present approach. The mesh adopted in the calculation is shown in Fig. 3.10.

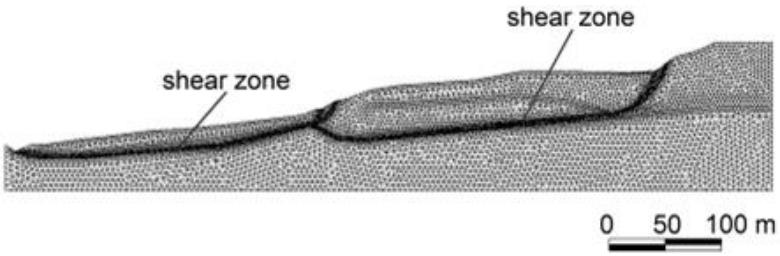

Fig.3.10 - Mesh adopted (Conte et al., 2014)

The shear zone is simulated by a 1 m thick layer which is located for the most part in the layer of fissured shale. At the extremities of the landslide body, this shear zone also develops in the clayey siltstone and colluvial debris (Fig. 3.10). The soil of the shear zone is modelled as an elasto-viscoplastic material with residual shear strength defined by the values of ϕ'_r (i.e. ϕ'_r=7.8° for the portion of the shear zone located in the fissured shales, and ϕ'_r=14.7° for the remaining parts located in the upper soil layers). The best agreement between measured and calculated results is achieved using the parameters shown in Tab. 3.2.

Material	γ **(kN/m^3)**	E' **(MPa)**	v'	ϕ'_r **(°)**	$\bar{\gamma}$ **(day)$^{-1}$**	k **(m/day)**
colluvial debris	20.5	15	0.33			$9\cdot10^{-5}$
clayey siltstone	20.5	15	0.40			$9\cdot10^{-6}$
fissured shales	21.5	10	0.40			$9\cdot10^{-5}$
shear zone	21.5	10	0.40	7.8-14.7	$4.5\cdot10^{-7}$	$9\cdot10^{-5}$
limestone	22.0	100	0.40			$9\cdot10^{-7}$

Tab.3.2 - Material parameters adopted

In this connection, Fig. 3.12 compares the accumulated displacements measured at the top of the boreholes S2, S5 and S6 (see Fig. 3.3 for their location) with those calculated using the present approach. It is worth noting that in this case study the updated Lagrange formulation (Roddeman, 2013) was used owing to the large displacements occurred. The agreement between predicted and observed displacements can be deemed satisfactory for all the locations considered, although some rapid increases in displacement are not exactly reproduced in the theoretical time–displacement curves. In addition, Fig. 3.11 shows the total displacement field calculated at the final time of analysis. These results confirm the evidence that the lower unit is the most active slide.

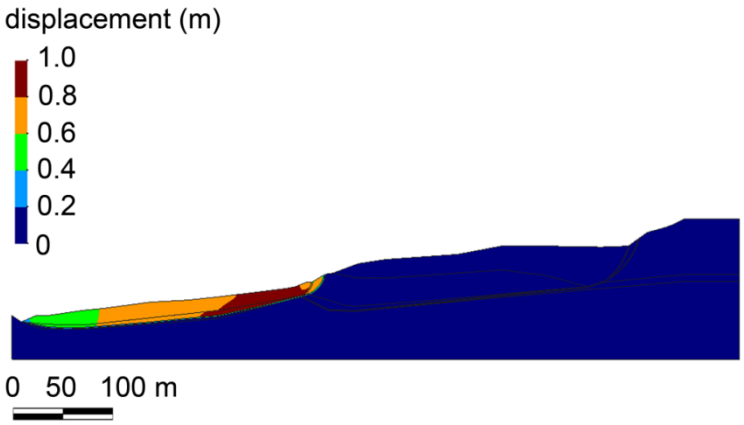

Fig.3.11 –Displacement field obtained from the numerical analysis (Conte et al., 2014)

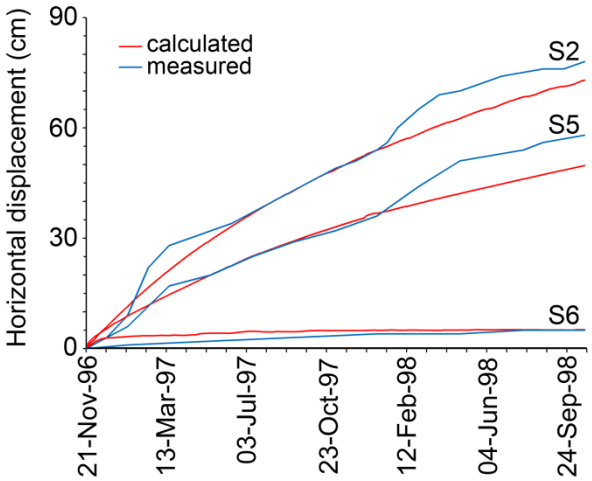

Fig.3.12 - Comparison between measured and calculated superficial displacements

3.3. The Fosso San Martino landslide

The second case study concerns the Fosso San Martino landslide which is an active slide periodically mobilized by groundwater fluctuations, as documented by Bertini et al. (1984). This case study was analysed by several authors using different approaches (Bertini et al., 1986; D'Elia et al., 1998; Picarelli et al., 2004; Calvello et al., 2008; Conte and Troncone, 2012a). The landslide is located in central Italy and is characterized by very slow movements. A representative geological cross-section of the slope is shown in Fig. 3.13.

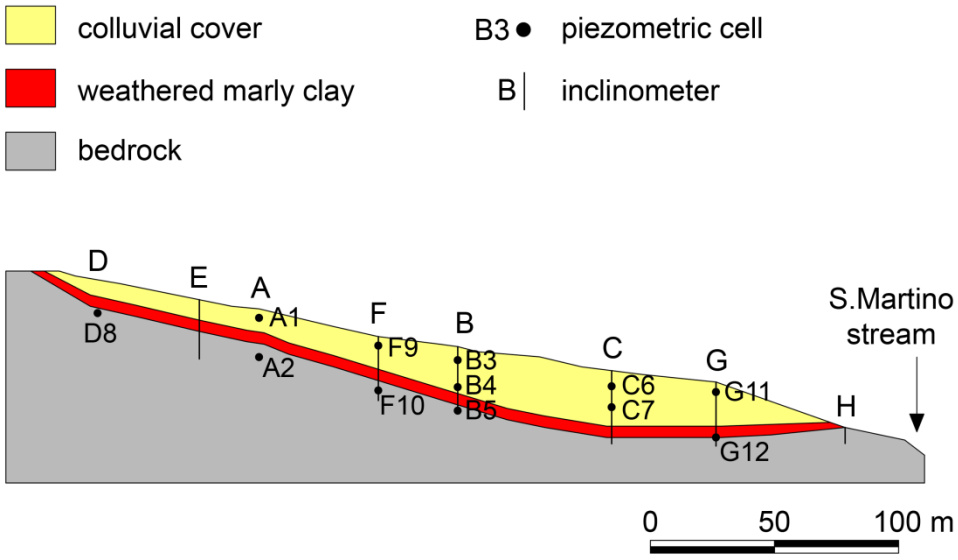

Fig.3.13 - Main section of San Martin landslide (Conte et al., 2014)

As it can be seen, the subsoil essentially consists of a marly clay formation (bedrock) covered by a thick layer of clayey silt (colluvial cover). The shear zone is located immediately below the colluvial cover at an average depth of about 20 m, and it involves a weathered marly clay layer the thickness of which varies from 2 to 5 m (Bertini et al., 1986; Calvello et al., 2008).

3.3.1. Simplified analysis

The simplified method described in paragraph §2.2.2, is first applied to the Fosso San Martino landslide. Referring to Fig. 3.5, geometric and geotechnical data are shown in table 3.3.

GEOMETRIC DATA					
h_f (m)	z_w (m)	h_w (m)	H (m)	α (°)	L_{ref} (m)
19.69	14.77	16.74	14.77	10	3.1
GEOTECHNICAL PARAMETERS					
γ (kN/m^3)	c' (kPa)	ϕ'_r (°)	c_v (m^2/day)	β (kN·day/m^3)	
21	0	16.5	75	$2 \cdot 10^8$	

Tab. 3.3 – Data adopted in the analysis

The groundwater level variations measured at the piezometric cell B3 (Fig.3.4) are considered as representative of the whole slope. The location of this piezometer is indicated in Fig. 3.13.

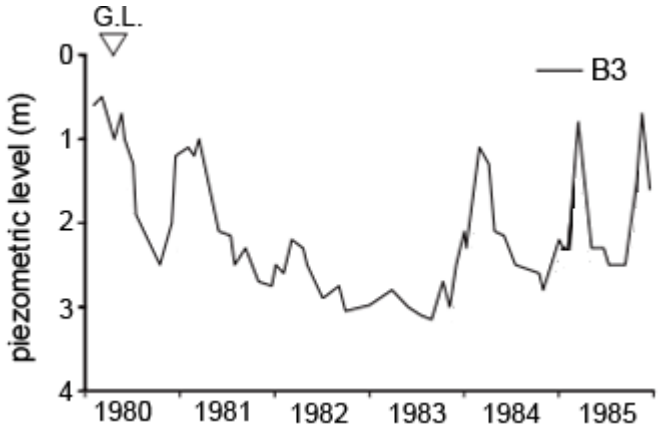

Fig.3.14 – Piezometric recordings (modified from Bertini et al., 1986).

The following figures show the corresponding results in terms of pore pressure changes at the piezometer B3 ($z=0$) and at the failure surface ($z=z_w$), safety factor, measured and calculated landslide velocity and permanent displacement.

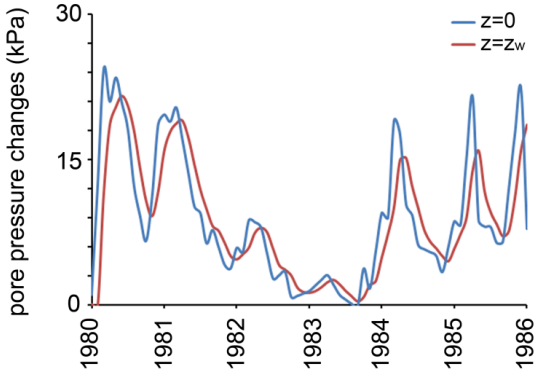

Fig. 3.15– Pore pressure changes at the piezometer B3 (z=0) and at failure surface ($z=z_w$)

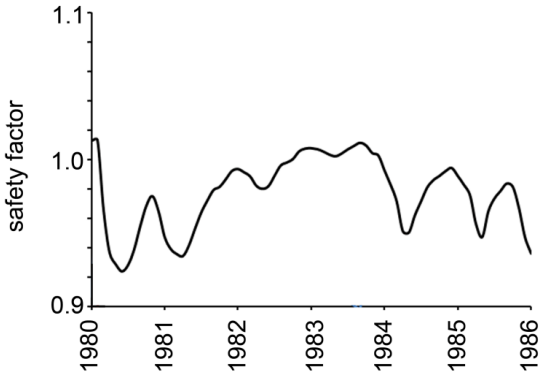

Fig. 3.16 – Safety factor versus time

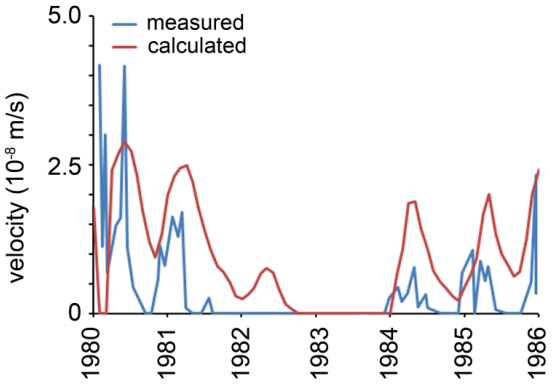

Fig. 3.17 – Comparison between measured and calculated velocities

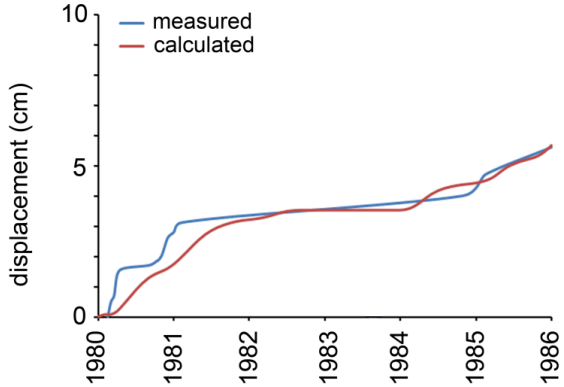

Fig. 3.18 – Comparison between measured and calculated displacement

The comparison between measured and calculated results can be considered satisfactory.

3.3.2. Finite Element Analysis

Table 3.4 reports the geotechnical parameters used in the analysis. Some of these parameters were obtained from laboratory and field tests by Bertini et al. (1984), whereas the others ($\bar{\gamma}$, E',ν') are just calibrated on the basis of the field measurements. In this table, k_x and k_y are the hydraulic conductivities in the horizontal and vertical directions, respectively.

Material	γ **(kN/m^3)**	E' **(MPa)**	ν'	ϕ'_r **(°)**	$\bar{\gamma}$ **(day)$^{-1}$**	k_x **(m/day)**	k_y **(m/day)**
colluvial cover	20.5	70	0.35			0.05	0.05
weathered marly clay	20.5	15	0.40	16.5	10^{-8}	0.05	0.05
bedrock	20.5	100	0.45			0.3	0.01

Tab.3.4 - Material parameters adopted

Several piezometric cells and inclinometers were installed within the slope. Their location is indicated in Fig. 3.13. The piezometric levels measured from 1980 to 1982 at the cells located close to the ground surface (Fig. 3.19) are used in the present study to describe the groundwater fluctuations. Following Bertini et al. (1986), these fluctuations were responsible of the landslide mobility in the above-mentioned period of observation.

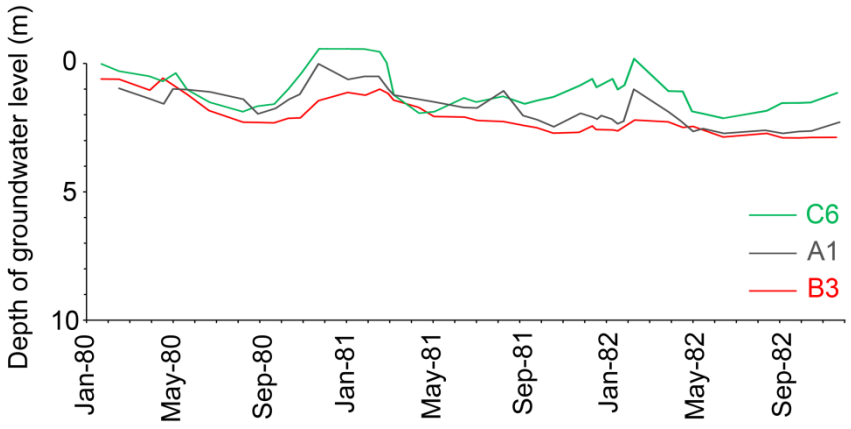

Fig. 3.19 - Piezometric levels used as input (Conte et al., 2014)

In addition, Figs. 3.20a and 3.20b show the displacement profiles at inclinometers B and C which were installed in the central part and near the foot of the slope, respectively. These profiles reveal that the landslide body essentially moves as a rigid body sliding over the underlying bedrock, whereas the overlying colluvial cover is affected by deformations of no great concern.

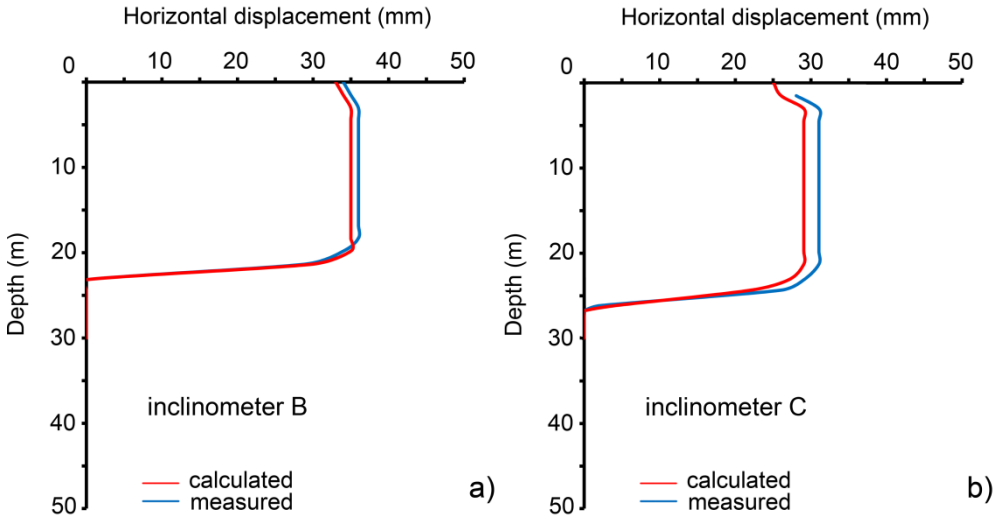

Fig.3.20 - Comparison between measured and calculated inclinometric profiles (Conte et al., 2014)

The mesh adopted in the calculations is shown in Fig. 3.21 where the shear zone is also indicated.

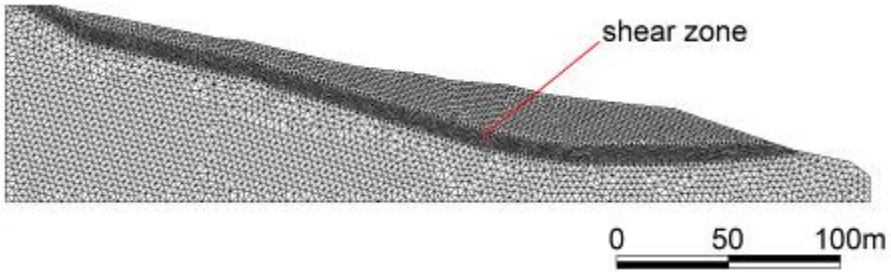

Fig.3.21 - Mesh adopted in the analysis (Conte et al., 2014)

Some comparisons between measured and calculated results are shown in Figs. 3.20, 3.22 and 3.23 in terms of displacement profiles for inclinometers B and C at the final time of observation, and in terms of horizontal displacement versus time at the top of the same inclinometers, respectively (Fig. 3.13).

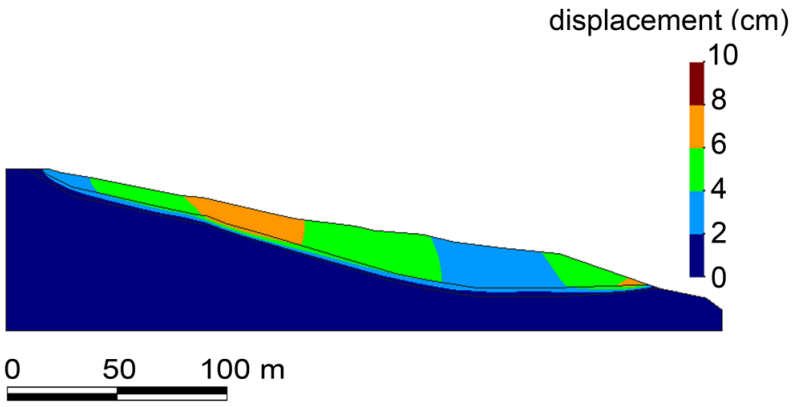

Fig.3.22 – Displacement field obtained from the numerical analysis (Conte et al., 2014)

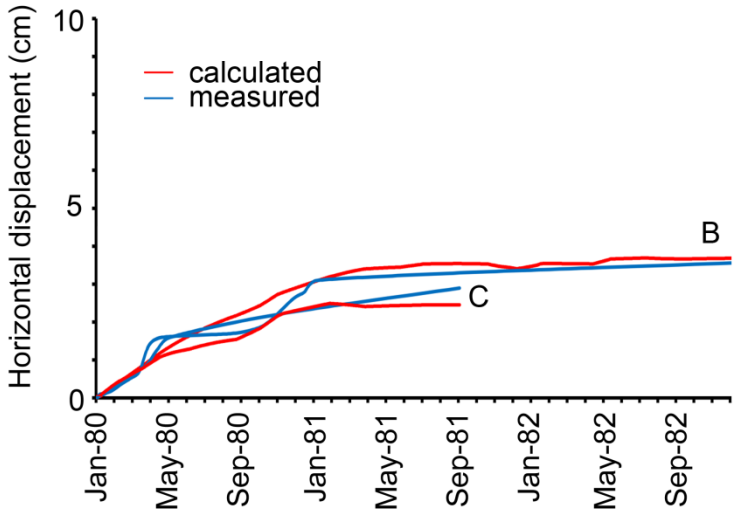

Fig. 3.23 - Comparison between measured and calculated superficial displacements (Conte et al., 2014)

In addition, Fig. 3.24 shows a comparison between recorded and computed piezometric levels at some piezometric cells located at different depths within

the slope. There is a fairly good agreement between experimental and theoretical results for all the verticals considered.

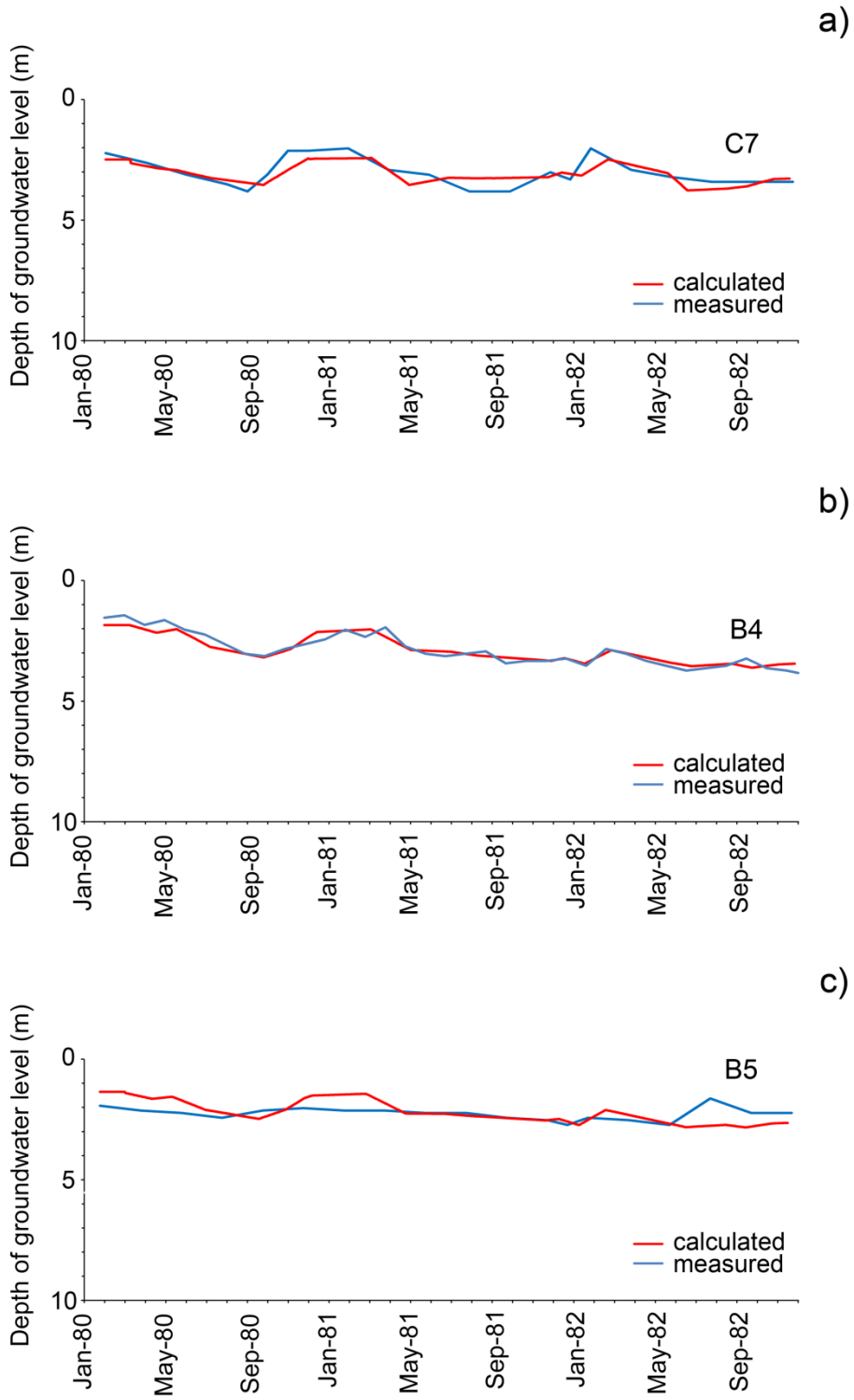

Fig.3.24 - Comparison between observed and predicted piezometric levels (Conte et al., 2014)

3.4. The Steinernase landslide

The last case study concerns the Steinernase landslide (Laloui et al., 2009) which is a slide located in the Aargau canton, in Switzerland (Fig.3.25)

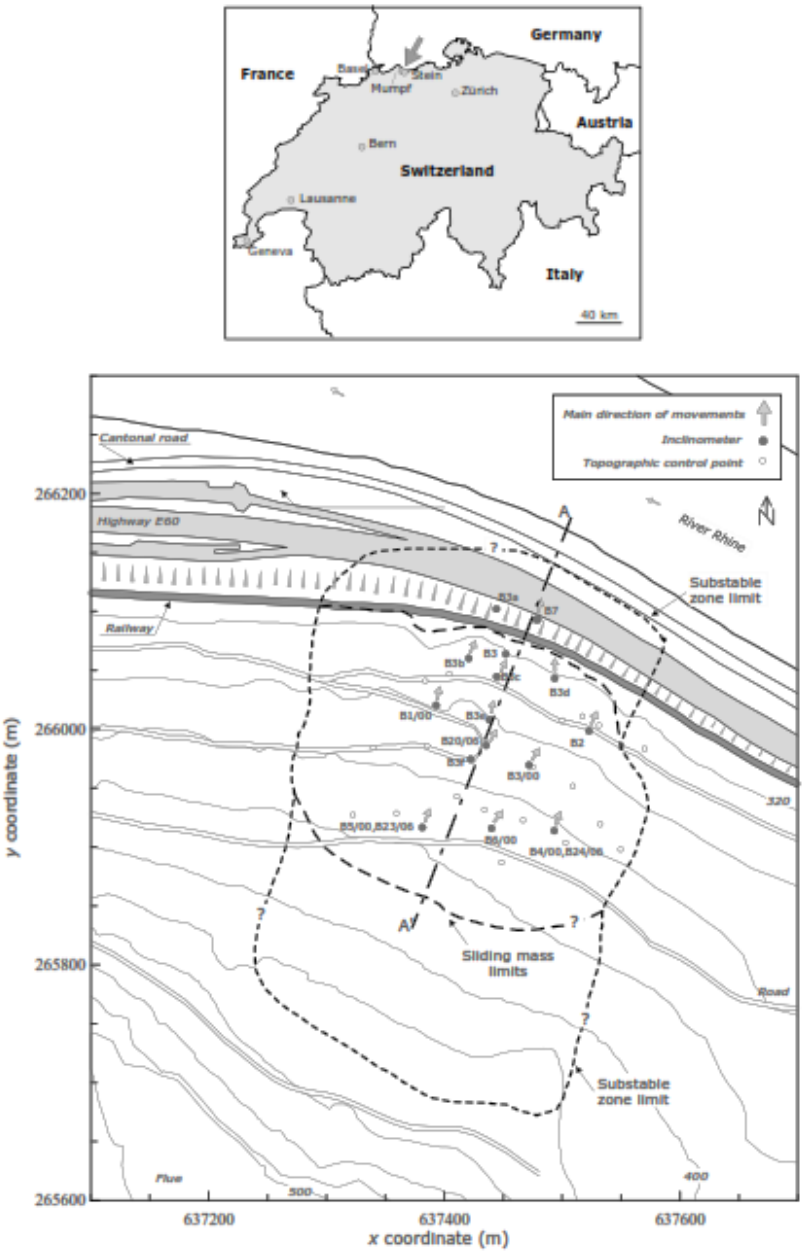

Fig. 3.25 - Location of Steinernase landslide in Switzerland (Laloui et al., 2009)

Pore pressure changes owing to groundwater fluctuations within the slope, ware recognized as the main cause for the continuous reactivation of this landslide.

As an example, Fig. 3.26 shows the piezometric level fluctuations measured at a depth of 10 m of the borehole B3c, from July 1997 to December 2006.

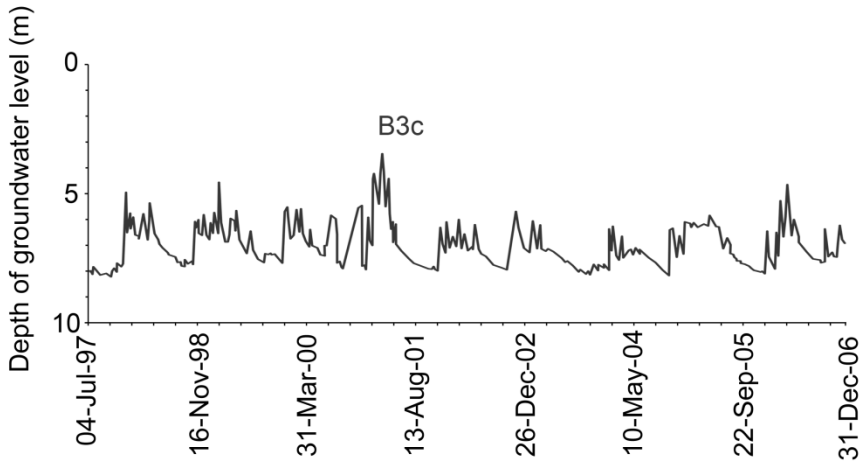

Fig.3.26 - Measured piezometric level (Conte et al., 2014)

A representative geological cross-section of the slope is presented in Fig. 3.27, from which it can be observed that the subsoil consists of an upper layer denoted as soil cover resting on a formation of limestone (bedrock). The soil cover is principally composed of colluvial clay. In addition, a deposit of alluvium of the Rhine River is present at the foot of the slope.

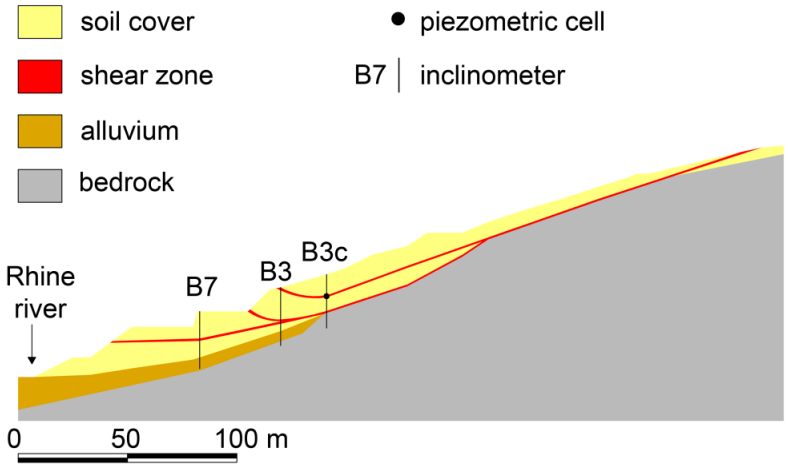

Fig. 3.27 - Main section of the Steinernase landslide (Conte et al., 2014)

Three shear zones are also indicated in Fig. 3.27. Their location was carefully reconstructed on the basis of the displacement profiles recorded at the inclinometers installed in the slope. The shear zones completely develop in the soil cover and give rise to a multiple surface failure mechanism (Ferrari et al., 2008). Direct shear tests performed on specimens from the shear zones provided values of the friction angle ranging from 24° to 27° and an effective cohesion close to zero. Slightly lower values were found by Laloui et al. (2009) for the soil in the most superficial shear zone. On the basis of these data, the values of the soil friction angle assumed in the present analysis are 23°, 26° and 27° for the upper shear zone, the intermediate shear zone and the lower shear zone (Fig. 3.27), respectively.

3.4.1. Simplified analysis

The simplified method is applied also to the Steinernase landslide. Referring to Fig. 3.5, the assumed geometric and geotechnical data are listed in Tab.3.5.

GEOMETRIC DATA					
h_f (m)	z_w (m)	h_w (m)	H (m)	α (°)	L_{ref} (m)
17	8	9	8	18	8
GEOTECHNICAL PARAMETERS					
γ (kN/m^3)	c' (kPa)	ϕ'_r (°)	c_v (m^2/day)	β (kN·day/m^3)	
20	0	24	25	$1.55 \cdot 10^{10}$	

Tab. 3.5 – Data adopted in the analysis

The input is represented by the groundwater level variations at the piezometric cell B3c (described by two hundreds Fourier components), and shown so far in Fig. 3.26. Its location is indicated in Fig. 3.27. The following figures show the results obtained in terms of pore pressure changes at the failure surface and safety factor of the slope.

The piezometric cell used as representative for the whole slope is located close to the failure surface. Therefore, the pore pressure changes at $z=0$ and $z=z_w$ coincide. No data in terms of landslide velocity is available, hence a comparison is provided in terms of permanent displacement.

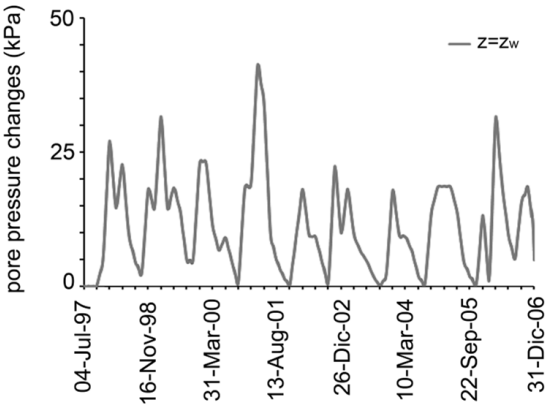

Fig. 3.28– Pore pressure changes at the failure surface ($z=z_w$)

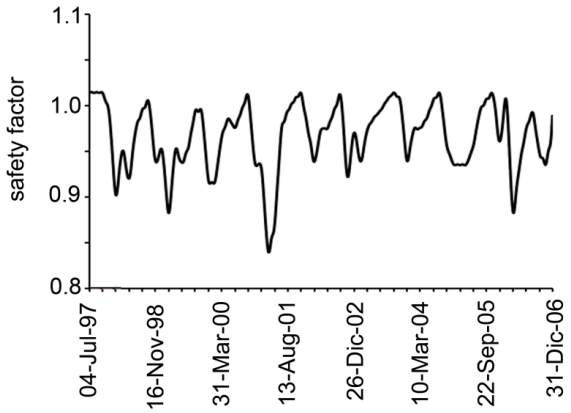

Fig. 3.29 – Safety factor versus time

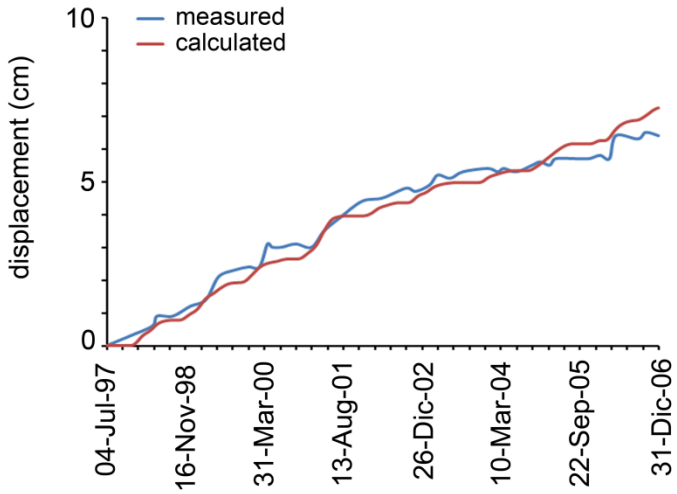

Fig. 3.30 – Comparison between measured and calculated displacement

Also for the present case study, the results show that the simplified method is capable of account for the main aspects of the landslide mobility owing to the changes in the pore water pressure regime.

3.4.2. Finite Element Analysis

Fig. 3.31 and table 3.6 show the mesh and the soil parameters adopted in the analysis, respectively.

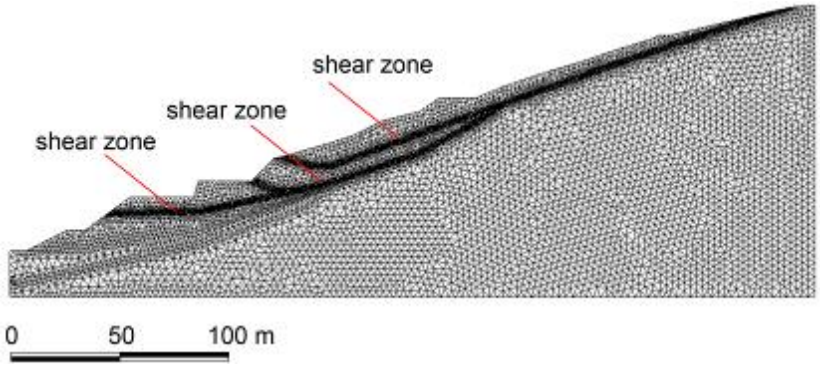

Fig.3.31 - Mesh adopted in the analysis (Conte et al., 2014)

Material	**γ (kN/m^3)**	**E' (MPa)**	**ν'**	**ϕ'_r (°)**	**$\bar{\gamma}$ (day)$^{-1}$**	**K (m/day)**
soil cover	19	15	0.40			1
shear zone	19	10	0.40	23-27	$9 \cdot 10^{-9}$	1
alluvium	19	200	0.40			1
bedrock	20	500	0.40			1

Tab.3.6 - Material parameters adopted in the analysis

Some comparisons between measured and calculated results are shown in Fig. 3.32 in terms of the horizontal displacement at the top of the inclinometers B and C versus time. As it can be seen, the finite element results compare reasonably well with the measured displacements at the top of the inclinometers considered.

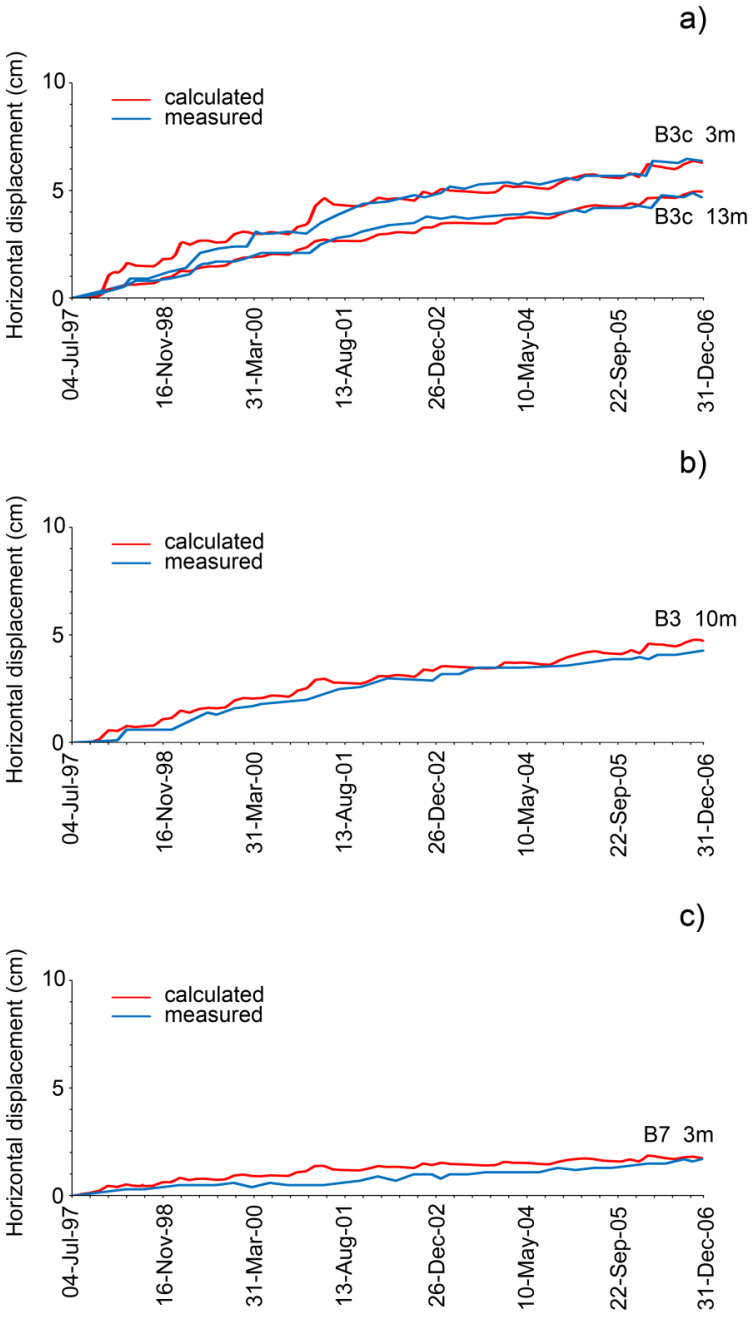

Fig.3.32- Comparison between measured and calculated displacement
a) inclinometer B3c; b) inclinometer B3; c) inclinometer B7 (Conte et al., 2014)

In addition, Fig. 3.33 shows another comparison in terms of the displacement profile at the inclinometer B3c which was installed in the central part of the slope (Fig.3.27).

In particular, this profile shows the presence of two slip surfaces: the first one at a depth of 8 m and the deeper one at a depth of 20 m from the ground surface.

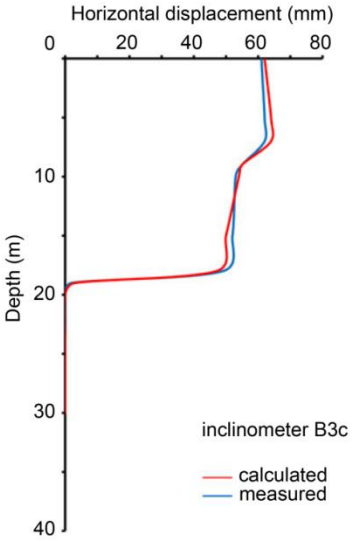

Fig.3.33 - Comparison between measured and calculated inclinometer profile (Conte et al., 2014)

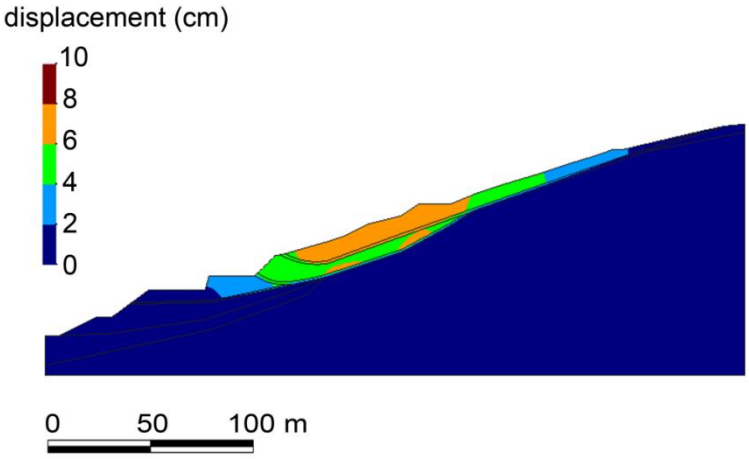

Fig.3.34 - Displacement field obtained from the numerical analysis (Conte et al., 2014)

As it can be seen, the finite element results compare reasonably well with the measured displacement. In addition, the calculated displacement field (Fig.3.34) accounts for the multi-surface failure mechanism documented by the inclinometer profile.

3.5. Concluding remarks

A simplified method and a finite element approach have been adopted to evaluate the mobility of active slow-moving landslides owing to changes in the pore pressure regime. The first one is an analytical method that permits to calculate the landslide velocity on the basis of the piezometric measurements that are known at a representative borehole. This method utilises the Fourier series and some analytical expressions that may be readily implemented in a common spreadsheet. Therefore, the computational costs are very low.

The finite element approach permits a more comprehensive modelling of the landslide. In particular, it includes an elasto-viscoplastic constitutive model which is used in the present study to model the behaviour of the soil in the shear zone. For the other soils involved by the landslide, an elastic model is assumed for the sake of simplicity. Both the approaches require few parameters as input data, the most of which can be readily obtained by conventional geotechnical tests. The rest of the required parameters (in particular, the viscous parameters β and $\bar{\gamma}$) should be calibrated on the basis of field measurements concerning the change in the piezometric levels and the associated movements of the landslide body. After being calibrated and validated, the proposed approaches can be applied to situations similar to those considered in the present study to predict future landslide movements owing to expected groundwater fluctuations or to assess the effectiveness of drainage systems used as preventive measures to control the landslide mobility.

Chapter 4

The Maierato landslide

4.1. Overview

4.1.1. Introduction

The village of Maierato is located in Calabria (Southern Italy) and is far about 10 km from Vibo Valentia (Fig.4.1).

The Maierato landslide considered in this study occurred on 15th February 2010 and affected the localities denoted as "Draga", "Mosto" and "Giardino". The elevation of the study area ranges from 100 to 450 m asl.

Fig.4.1 – Location of Maierato

4.1.2. Antecedent landslides in the Maierato territory

The Maierato territory is affected by a big deep-seated gravitational slope deformation (DGSD) with an extension of about 26 km^2, which is bounded by Fosso Scotrapiti and Fosso Ceramida (Fig.4.2).

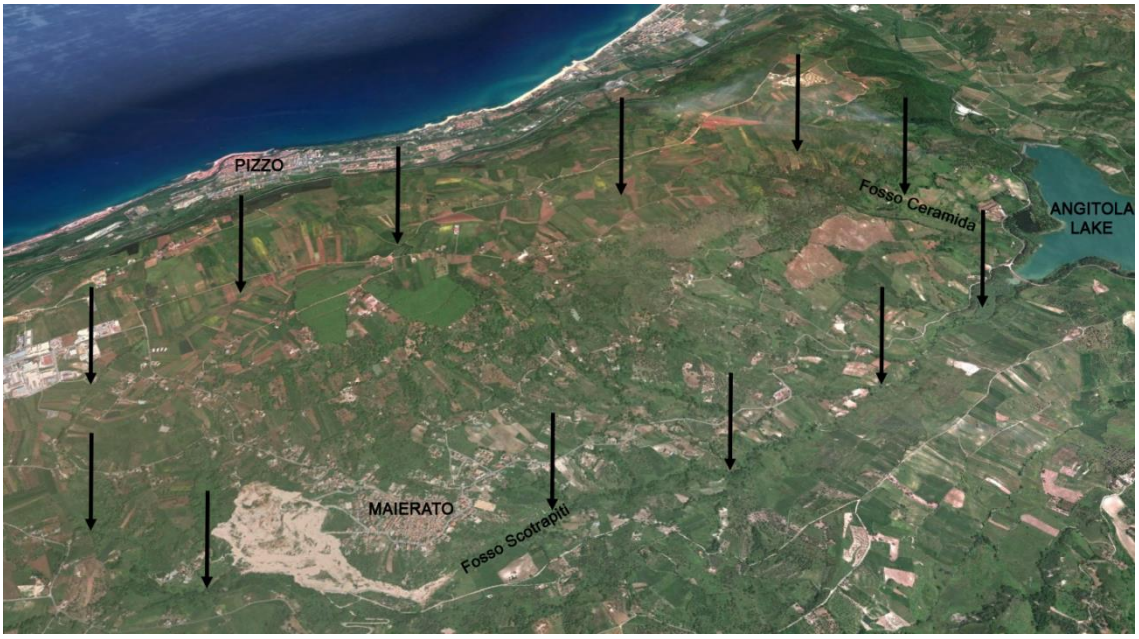

Fig.4.2 –The area affected by the DGSD (delimited by black arrows) with a view of the Maierato landslide (from Guerricchio et al., 2010)

Likely, the big DGSD was originated by a marine regression during the last glacial period, between the end of Pleistocene and the begin of Holocene (Cotecchia et al., 1969). In fact, in that period of time, the sea level was lower than nowadays and caused deep erosion processes. The sea retreat during the Pleistocene period conditioned the morphology of Fosso Scotrapiti, which became deeper and caused failure processes of the slope falling in its hydrographic basin (Guerricchio et al., 2010).

As a result of the DGSD, the study area is characterized by several landslides, also documented by the maps from the PAI (Hydrological asset plan of Regione Calabria) and the IFFI (Landslides list in Italy), as shown in Figs.4.3 and 4.4.

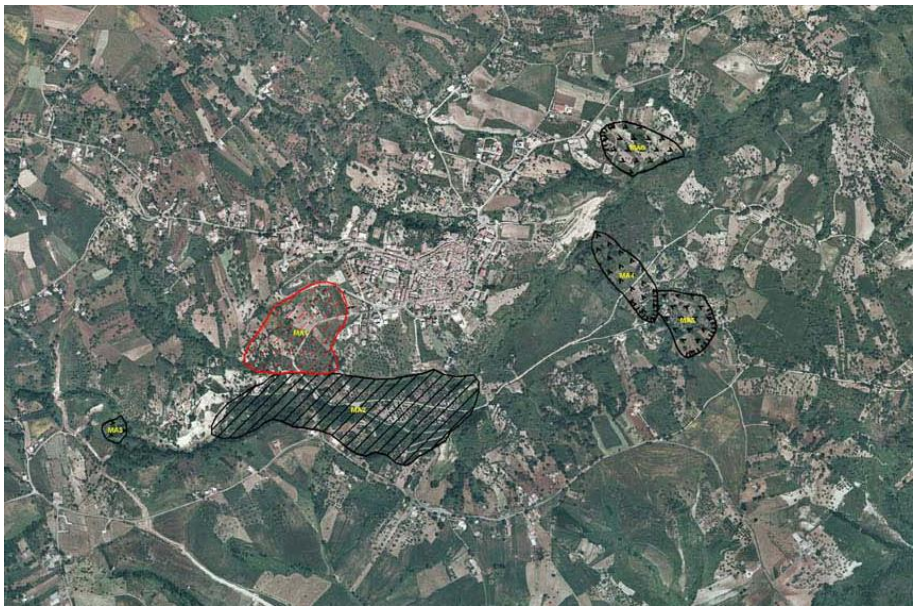

Fig.4.3 – Location of the antecedent landslides according to PAI
1) red area: active shallow landslide; 2) black striped area: quiescent deep landslide;
3) black with arrows: quiescent soil slips

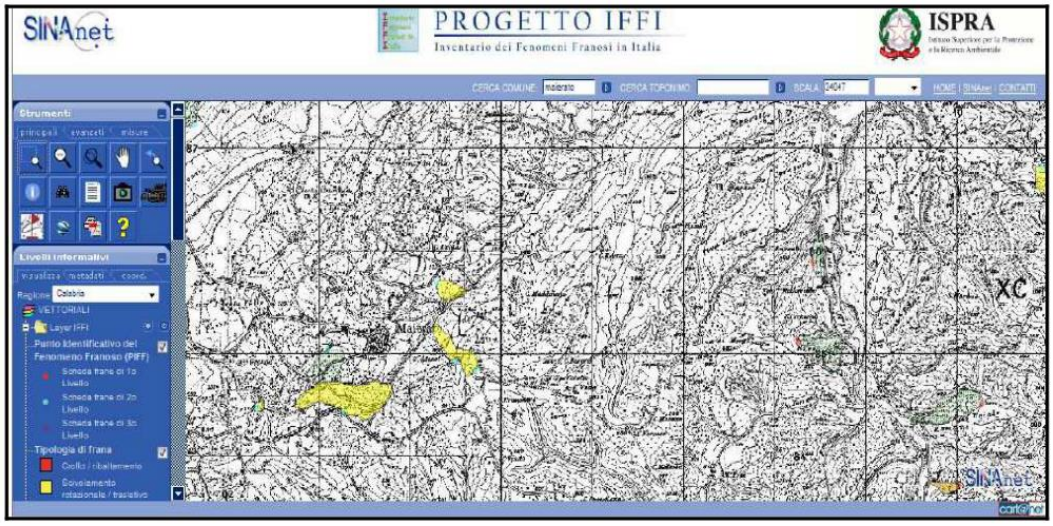

Fig.4.4 – Map of landslide risk (yellow) on the Maierato area, according to IFFI

The first documented landslide events are related to the 1783 earthquake which was completely destroyed the Maierato (Guerricchio et al., 2010).

Another previous documented landslide occurred in 1932. It affected the "Draga" location (Fig 4.5). This event produced an obstruction of the Fosso Scotrapiti, in which a lake called "Maretto" was created.

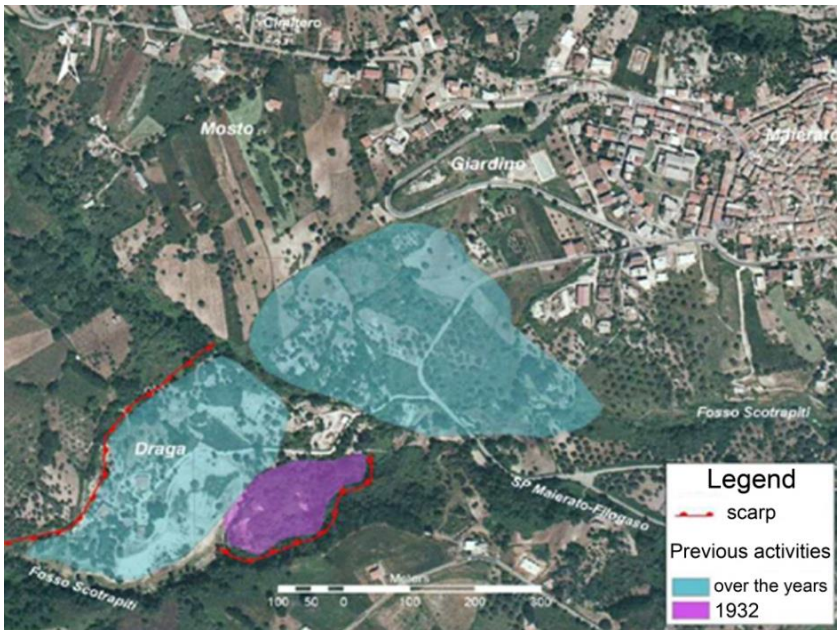

Fig.4.5 – Main documented landslide events (from ISPRA, 2010)

Referred to Figs.4.6 and 4.7 by Borrelli et al. (2014), other slides had been mapped which involved the shallow evaporitic limestone formation.

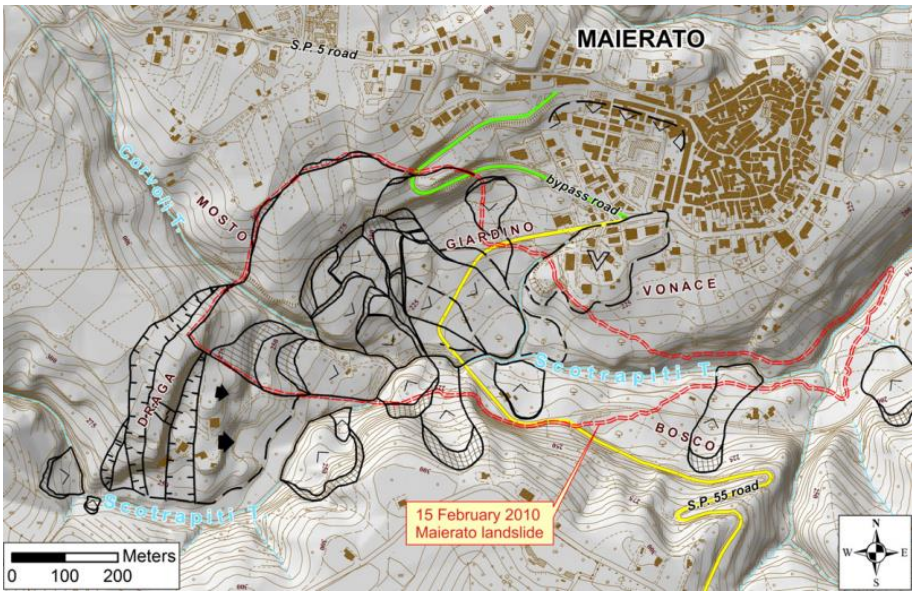

Fig.4.6 – Map of the landslides in the Maierato area (from Borrelli et al., 2014)

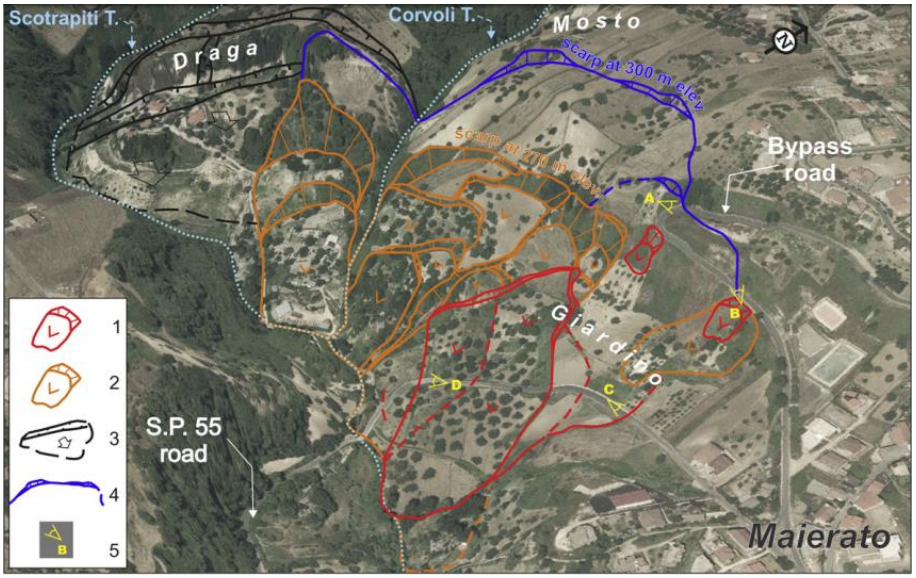

Fig.4.7 – Pre-2010 event landslides map with state of activity assessed through a comparison of multitemporal aerial photos (photos of 2001 compared with photos of 1991 and 1955), official landslide maps (PAI, Piano stralcio per l'Assetto Idrogeologico della Calabria, 2001), as well as consulting documents filed at the municipal and provincial records. Legend: 1) active slide; 2) dormant slide; 3) dormant block-slide and relative trenches; 4) slope failure (900 m long) made evident by an old, long, discontinuous scarp in incipient development stage (from Borrelli et al., 2014)

The landslide that occurred in 2010 was preceded by several landslide events which mainly affected the S.P.55 Filogaso-Maierato road, as shown in Fig.4.8. In particular, two clear lateral cuts occurred on the road (Figs.4.9 b,c) and a hairpin road collapsed (Figs.4.9 d).

Fig.4.8 – Localization of several important instability events in the area

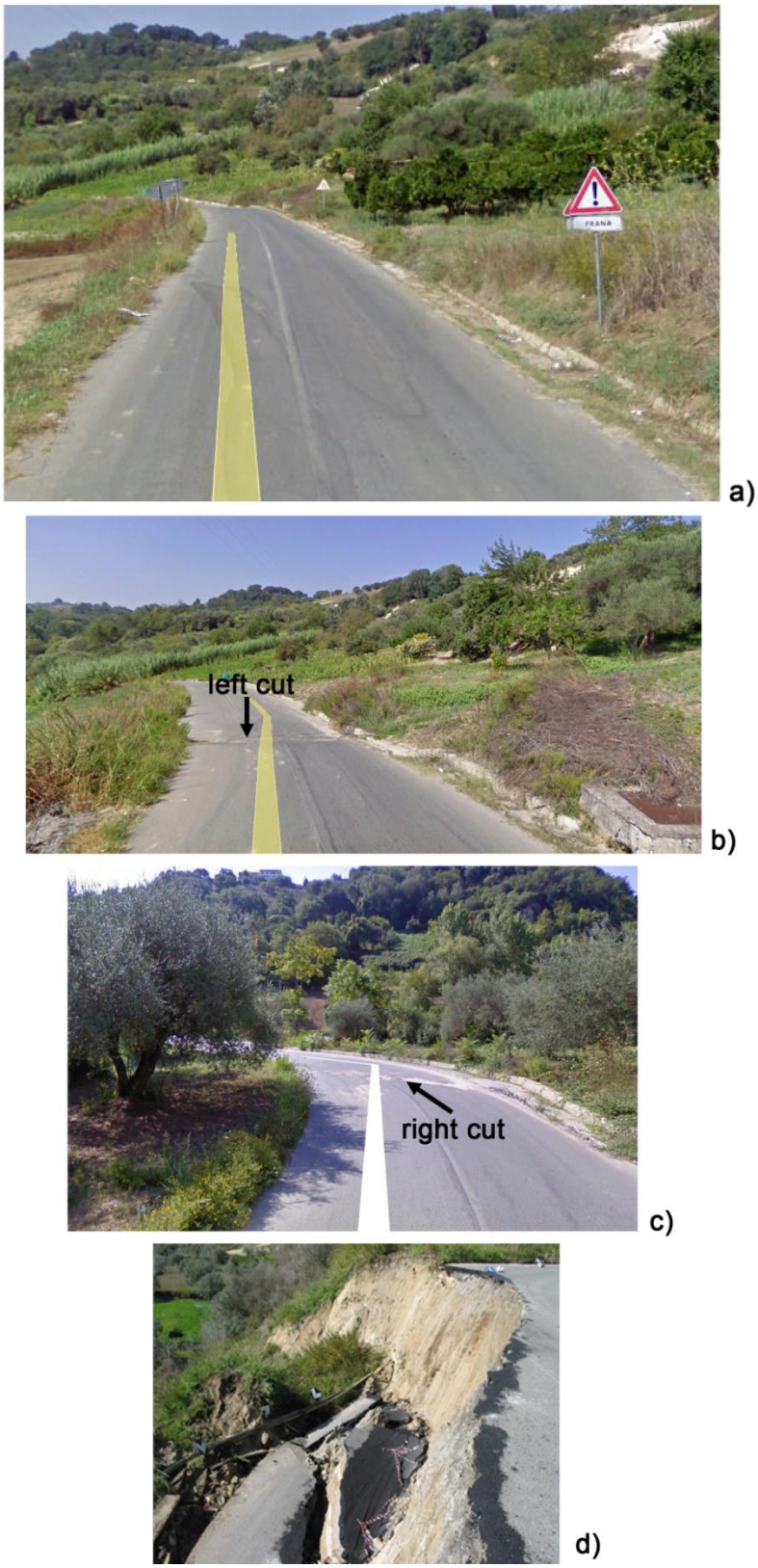

Fig.4.9 – Some events preceding the landslide: a) a view of the SP55 road with an indication of active landslides by a signpost; b) left cut on the road; c) right cut on the road; d) collapse of a hairpin road

4.1.3. Brief description of the landslide

The main event occurred on the 15th of February 2010 after a long period of heavy rainfall which caused an increase in the groundwater levels within in the subsoil.

Fig.4.10 – The Maierato landslide (orthophoto)

This event can be classified as a complex slide that evolved in a flow. It involved rock and soil formation, as following described. In spite of antecedent activity, this landslide was not monitored before the failure.

A view of above of the landslide is shown in Figs. 4.10 (orthophoto) and 4.11 a,b (from NASA satellite).

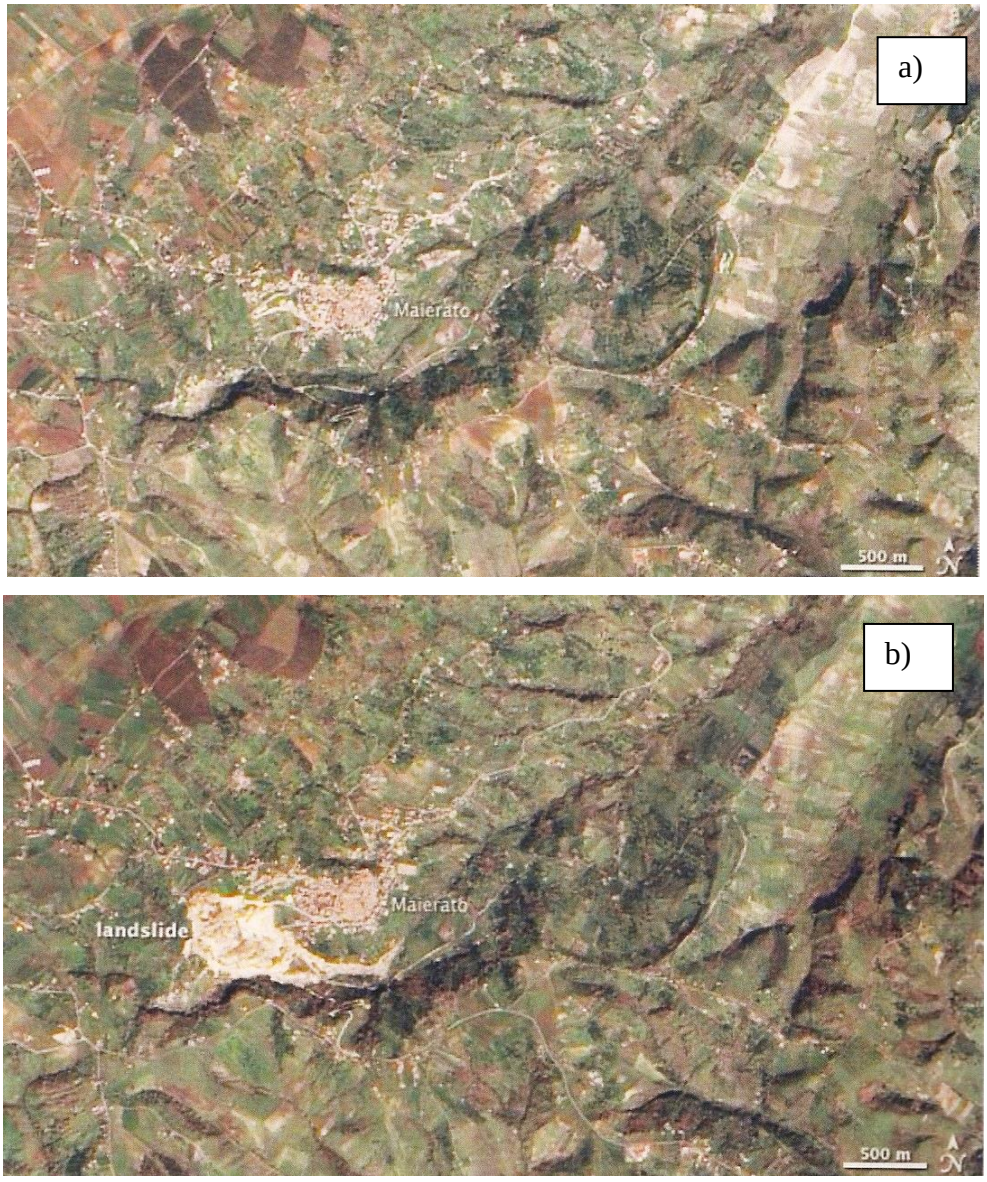

Fig.4.11 – The Maierato area from NASA satellite: a) before the event; b)after the event

The landslide volume was about 6 million cubic meters extended over 1 km in length and about 0.5 km in width, respectively. The landslide produced a small lake in the Fosso Scotrapiti and caused a loss of 18 ha of farmland. In addition, some services such as the water and methane pipelines (located in the upper part of the slope) were destroyed.

The landslide was preceded by severe deformations in the lower part of the slope. Due to this, the area was under survey and the activation phase was filmed. On the base of the images available, it appears that the landslide movement propagated backward causing a series of breaks and detachments as a sort of multiple rotational slide. The failure process timeline is documented in the following photos.

Fig.4.12 a) 9.47am: cuts on the road S.P. 55 Filogaso-Maierato (Draga locality)

Fig.4.12 b) 11.29am: deformations on the road S.P. 55 Filogaso-Maierato (Bosco locality)

Fig.4.12 c) 3.15pm: deformations on the road S.P. 55 Filogaso-Maierato (Bosco locality)

Fig.4.12 d) 2.06pm: pre-existing scarp on the evaporitic limestone gains further at 270 m asl (Pantano locality)

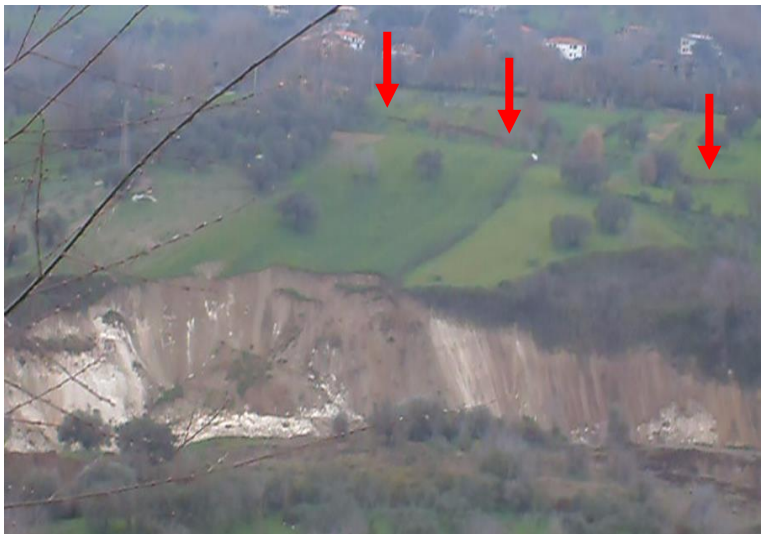

Fig.4.12 e) 4.21pm: main scarp formation (red arrows) at 300 m asl

Fig.4.12 f) 4.24pm: main scarp (red arrows) at 300 m asl and secondary scarp formation (blue arrows) at 285 m asl

Fig.4.12 g) 4.26pm: main scarp (red arrows) at 300 m asl, secondary scarp (blue arrows) at 285 m asl and a possible pre-existing slip surface at 310 m asl (orange arrows)

Immediately after the event occurred in 2010, the landslide presented a sub-vertical main scarp at 300 m asl with a height of about 50 m (Fig. 4.13).

A secondary scarp was observed at an elevation of 285 m asl. On 20th February 2010, a retreat of the main scarp of about 80 m occurred in central part of the slope.

Fig. 4.13 - Photos shot the day after the landslide (16-Feb-2010): (A) view of the phenomenon (from SW), with an indication of the building shifted by about 110 m; (B) secondary earth slide flow developed along the left flank of the landslide (from SE); (C) main scarp (from NE); (D) and (E) bulges and lateral levees, respectively, along the left flank (from Borrelli et al., 2014)

4.2. Geologic and geomorphologic aspects

Comprehensive geological studies were presented by Gattinoni et al. (2012) and Borrelli et al. (2014). Following these authors, the main outcropping geological formations from top to bottom are listed below:

- Pleistocene colluvial deposits variable in thickness (0-10 m) which present a predominance of conglomerates in a silt-sandy matrix;
- Pliocene deposits 5-25 m thick, composed of clayey sand and silt-clayey layers;
- Upper-Miocene evaporitic limestone and marl-clayey layers with a variable thickness from 25 to 45 m;
- Miocene clay and marl with a thickness of 3-20 m;
- Miocene sandstone and sandy clay thick from 10 to 40 m;
- Miocene conglomerates composed of rounded clasts and blocks of bedrock in thickness (0-5 m);
- Paleozoic weathered bedrock formed by gneiss and schists.

Borrelli et al. (2014) divided the landslide in three different parts: upper, intermediate and lower, as illustrated in Fig. 4.14.

Fig.4.14 – Partition of the Maierato landslide (Borrelli et al., 2014)

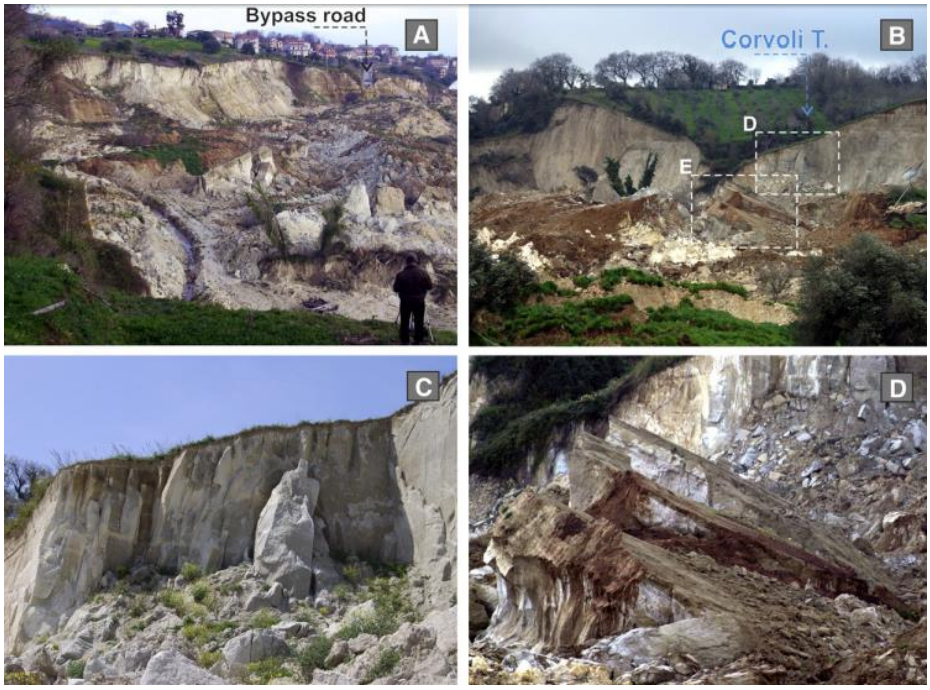

Fig.4.15a-d - Upper sector: (A) Main scarp (~600 m) that extends from NE to SW, making a gentle curve; (B) valley of the Corvolì Torrent that split the main scarp into two parts; (C) band of parallel joints (~15 m wide), NE–SW trending, related to the decompression that occurred during landslide movement along the main scarp; (D) large rock blocks rotated backward.

Fig.4.15e-h - Intermediate sector : (E) Very large rock block of evaporitic limestone, little deformed, translated downstream; (F) laminated marl strata, interbedded inside the evaporitic limestone, (G) secondary sliding surfaces exposed on the remnant marl strata; (H) toe of the failure surface of the Maierato landslide daylighting (for about 20 m) in the terminal part of the intermediate sector. (from Borrelli et al., 2014)

Fig.4.15k-o - Lower sector: K) panoramic view of the trenches, typical of a translational sliding, that caused the spreading of the limestone bank and the sinking of the overlying M) Pliocene deposits (N) decimetric brownish-red and green laminated marl layer, interbedded within the evaporitic limestone, and showing evidence of ductile deformation (O) with a folding that could have been caused by a translational movement of the overlying limestone bank (from Borrelli et al., 2014).

Figs. 4.15 (a-o) show the soils involved in these sectors of the landslide body. The Paleozoic gneissic bedrock is evident only in a small outcrop in the bed of the Scotrapiti torrent, in the proximity of the flow tongue and presents a high grade of weathering. In the same area, the Tortonian conglomerate transgressive on the gneissic basement crops out, with a thickness of about 1 m.

It is composed of poorly sorted conglomerate with clasts deriving from the underlying substratum. The overlying sandstone unit has a visible thickness of about 40 m and forms the fault scarp located at the base of the left flank of the Scotrapiti torrent. Along the edge of the fault scarps the overlying unit formed of upper Tortonian-early Messinian thin-bedded blue or bluish-gray emipelagic marls follows with a sharp contact. This unit shows a thickness from a few meters to 20 m. In the shallowest layers, marls are decolorized as a result of weathering. In the surrounding areas of Maierato, the marls pass upward through a discontinuity to the Messinian evaporitic limestone and made of highly porous, weak, yellowish-white, fine-grained, calcareous banks interbedded by brownish-red and green laminated marls. The evaporitic limestone shows a layering with a generally sub-horizontal attitude. The visible thickness of the unit is about 40 m. The landslide main scarp shows the stratigraphic succession lying on the evaporitic limestone. It is possible to measure the thicknesses of the lithological unit. In particular, on the outcropping evaporitic limestone at the base of the main scarp, a silty-clayey unit of the lower Pliocene lies in slight angular discordance and its thickness is about 15 m. Toward the edge of the main scarp, the silty-clayey unit is gradually substituted by fossiliferous grayish-yellow sand formation of the medium-upper Miocene, with thin intercalations of soft sandstones. It has a visible outcropping about 10 m in thickness. A sandy-gravelly deposit of the Pleistocene, about 5 m in thickness is visible only in the central part of the scarp.

4.3. Geotechnical properties

4.3.1. Site investigation

A site investigation consisting of boreholes and field tests was performed after the landslide [1]. Their location is indicated in Fig.4.16. In particular, $S_{UNICAL}1$ borehole is located close to the landslide crown and extended 80 m in depth, $S_{UNICAL}2$ on the left side of the landslide and extended 60 m in depth, $S_{UNICAL}3$ at the middle of the landslide body near the Maierato-Filogaso road and extended 32 m in depth. In addition, boreholes indicated with V1 and V2 are located close to $S_{UNICAL}1$ and $S_{UNICAL}2$, respectively. Other boreholes were carried out by Borrelli et al. and their position is also shown in Fig.4.16.

Boreholes $S_{UNICAL}1$ and $S_{UNICAL}2$ were instrumented with inclinometers. Open pipe piezometers with uptakes at different depths were installed along the verticals indicated as $S_{UNICAL}3$, V1 and V2.

During drilling, standard penetration tests (SPT) and Mènard pressuremeter tests (PMT) were carried out. In addition, some undisturbed specimens were taken to carry out laboratory tests.

[1] Data and information in the present study have been collected within the frame-work of the activities carried out for the action Regione Calabria — Supporto tecnico-scientifico al Commissario delegato O.P.C.M. n. 3862/2010.

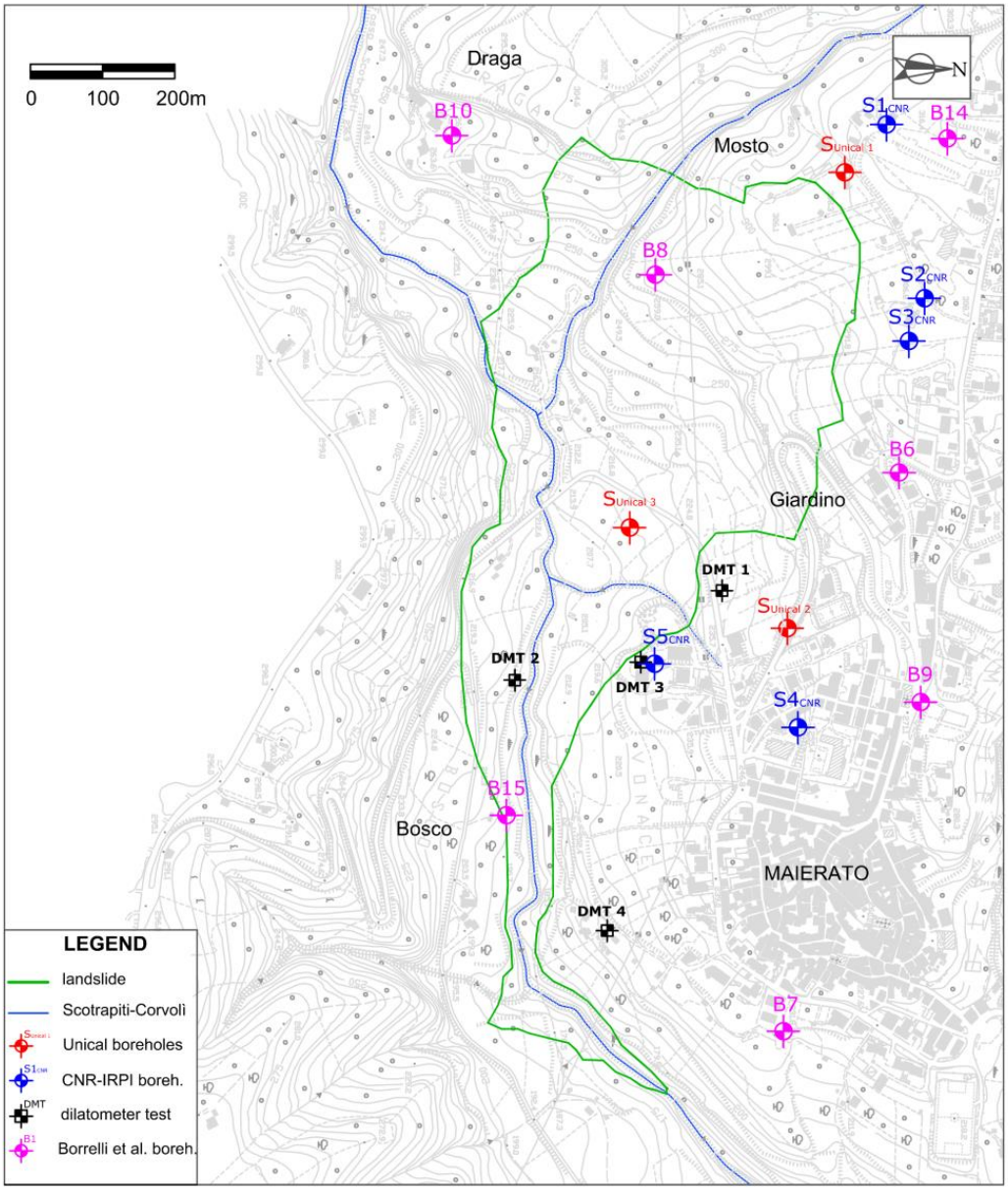

Fig.4.16 - Position of the investigations

In the following, a brief description of the stratigraphic profile relative to the S_{UNICAL} boreholes is provided.

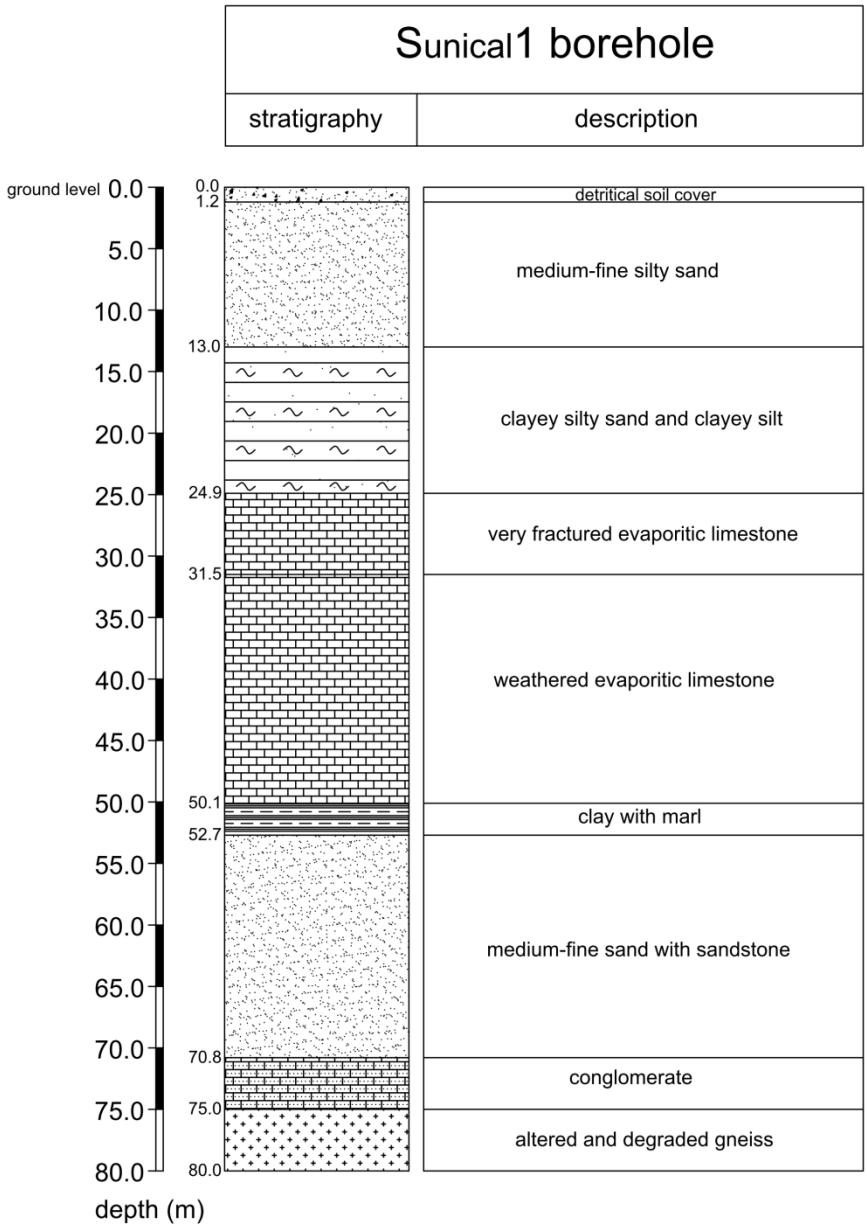

Fig.4.17 – $S_{UNICAL}1$ borehole

The $S_{UNICAL}1$ profile consists of a Pliocene silty sand layer 25 m thick, overlying an evaporitic limestone formation that extends to 50 m in depth. At greater depth, a Miocene clay layer (about 3 m in thickness) was found above a layer of sand with sandstone of Miocene origin, which in turn overlies a conglomeratic layer with a thickness of 4 m, and in succession a gneiss-schists formation.

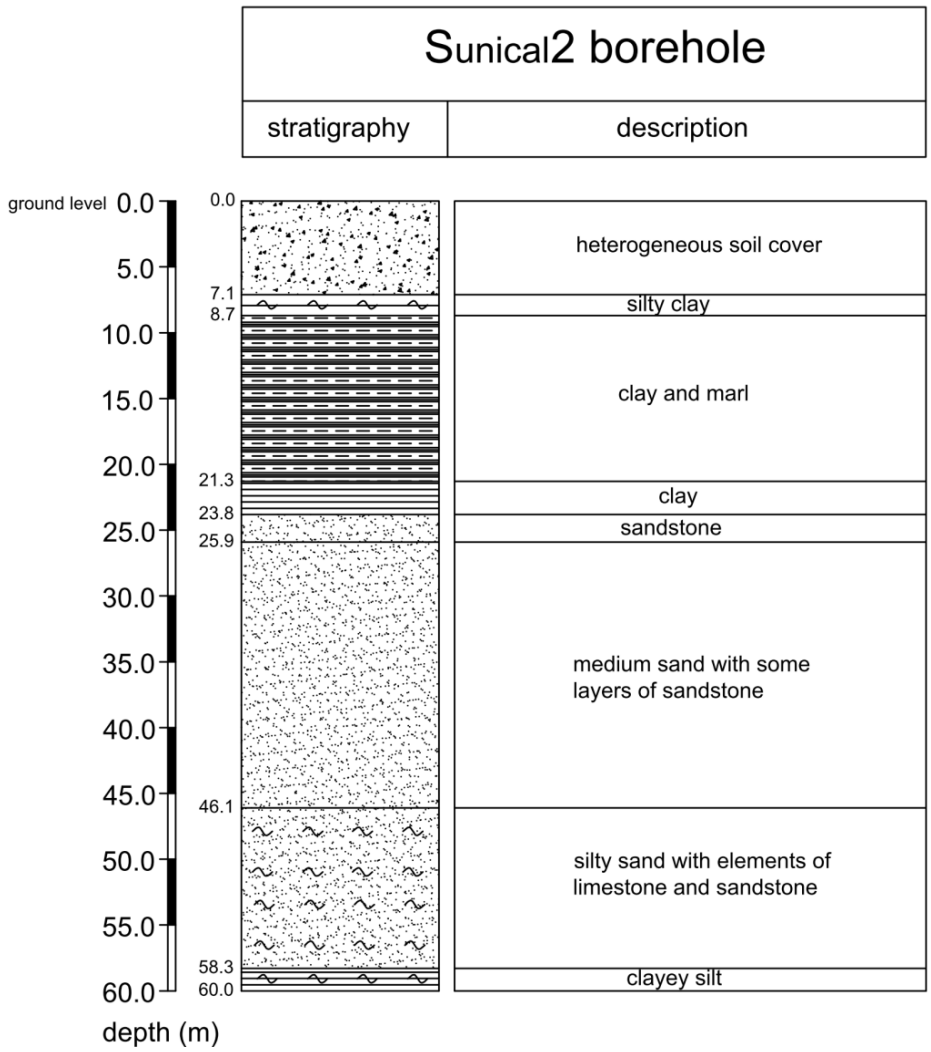

Fig.4.18 – $S_{UNICAL}2$ borehole

A Miocene clay layer 16 m thick was found at a depth of 7 m from the top of the vertical $S_{UNICAL}2$. This layer is interbedded between a soil cover and a sequence of Miocene sand layers and sandstone. It is worth noting that the evaporitic limestone formation was not found in this borehole, probably due to the occurrence of antecedent shallow landslides.

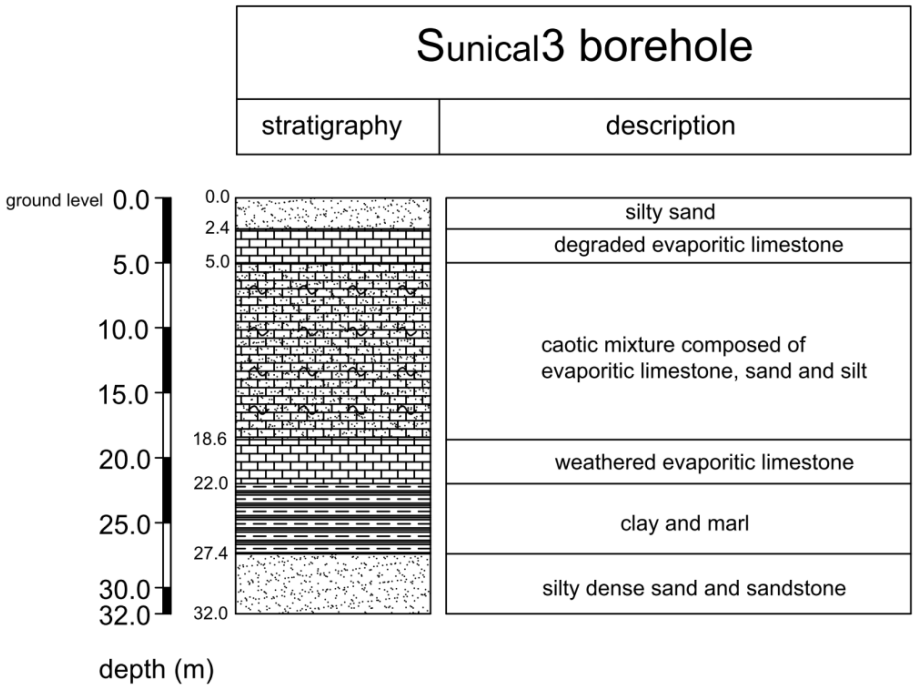

Fig.4.19 – $S_{UNICAL}3$ borehole

Finally, $S_{UNICAL}3$ borehole is characterized by a "chaotic mixture" composed of sand, silt and weathered evaporitic limestone. It extends to a depth of 18.6 m and is the landslide material. Above this, a layer of limestone 3.5 m thick, and a Miocene clay layer 5.4 m thick are present. Below the depth of 27.4 m, dense sand and sandstone are found.

The profiles of the boreholes provided by Borrelli et al. (2014) are schematically shown in Fig. 4.20 along with some photos of the soils taken during drilling.

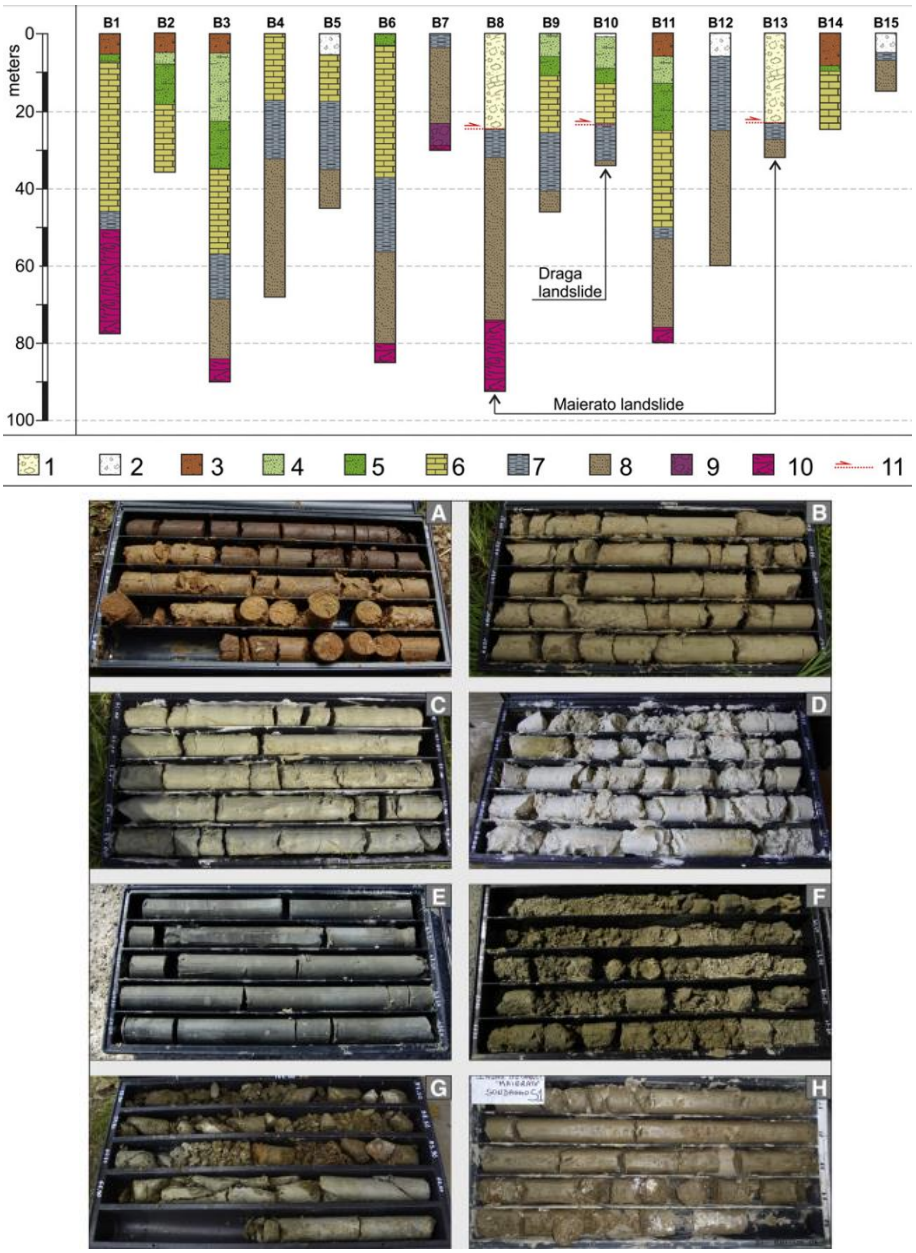

Fig.4.20 – Stratigraphy from the geotechnical boreholes carried out inside the landslide body and in the surrounding areas and photos of the principal rock types detected (A–H). Legend: 1) Maierato landslide debris; 2) anthropic cover; 3) Pleistocene gravels and sands (photo A); 4) Pliocene sands (photo B); 5) Pliocene silty clays (photo C); 6) Messinian evaporitic limestone (photo D); 7) upper Tortonian/early Messinian hemipelagic marls (photo E); 8) Tortonian sandstones (photo F); 9) Tortonian conglomerates; 10) Paleozoic gneissic basement moderately (photo G) and completely (photo H) weathered; 11) sliding surfaces (from Borrelli et al., 2014)

4.3.2. Standard penetration tests

The SPT tests were performed in the sandy layers, i.e. in the Pliocene soil cover and in the Miocene sandstone. All the results are illustrated in Figs.4.21-4.23 Values of N_{SPT} ranging from 20 to 40 blows/30cm were found in the Pliocene sand. On the contrary, the tests in the deeper Miocene sandstone provided rejection after few centimeters of penetration due to the high mechanical properties of the soil.

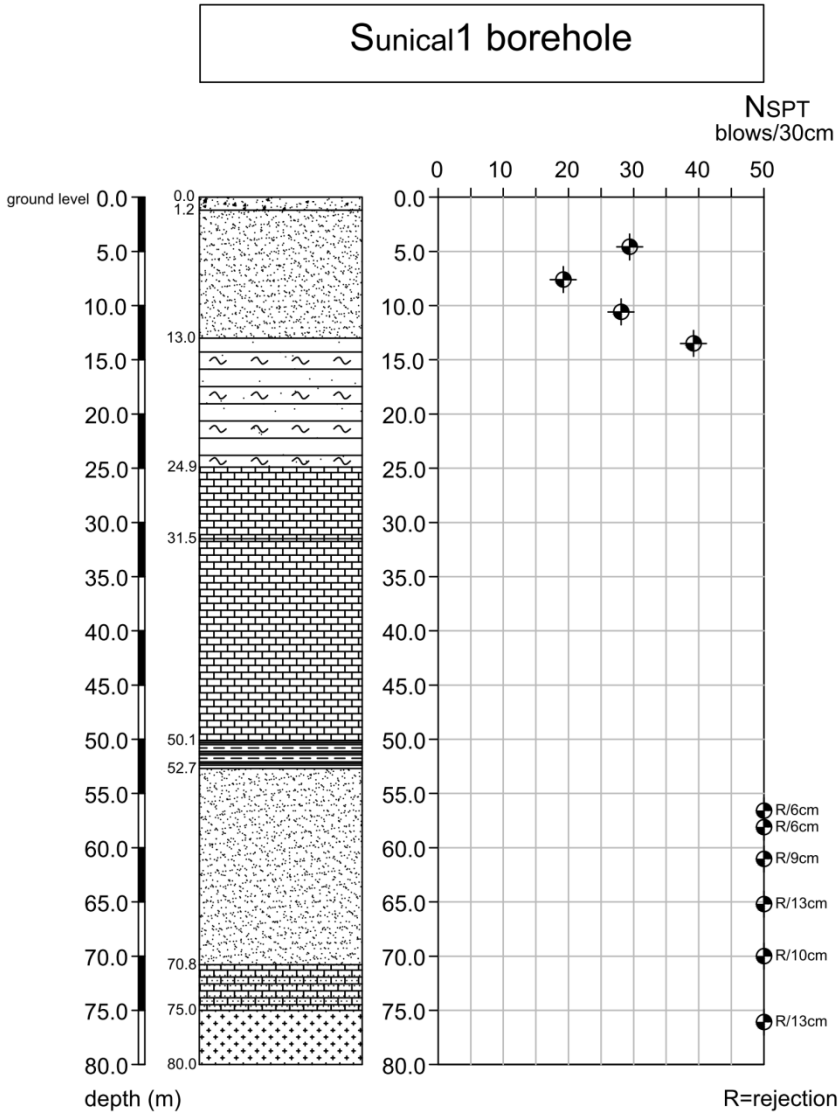

Fig.4.21 – Standard penetration test results at $S_{UNICAL}1$ borehole

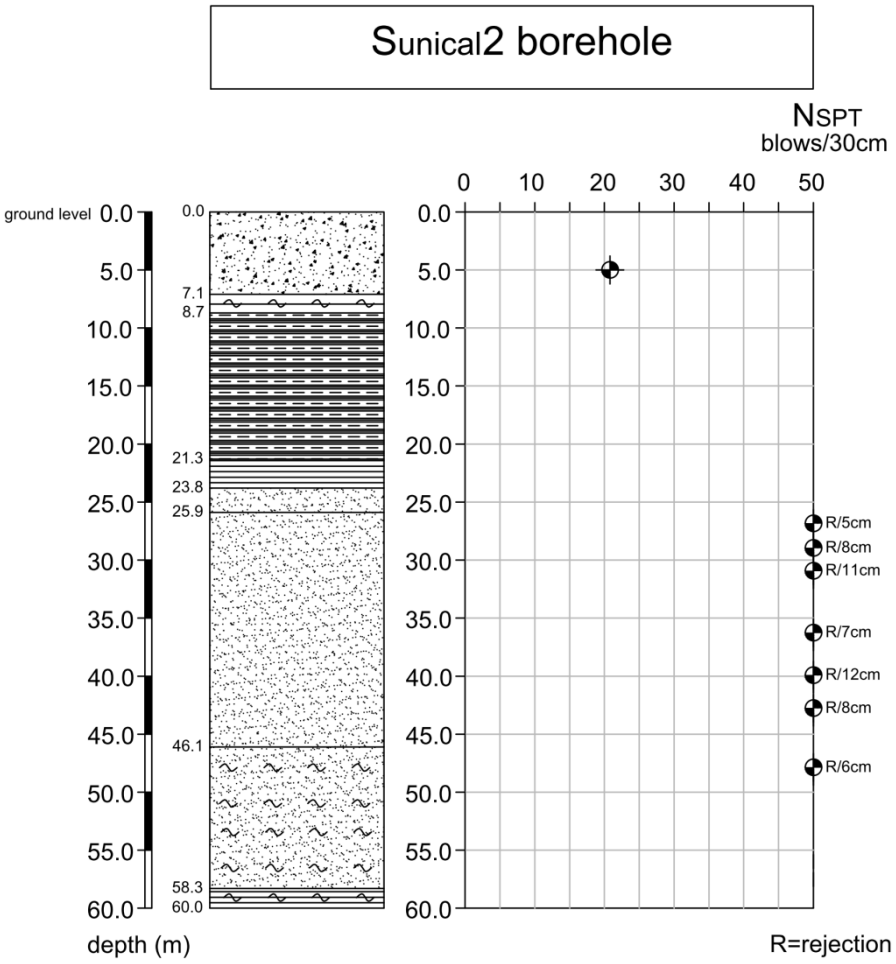

Fig.4.22 – Standard penetration test results at $S_{UNICAL}2$ borehole

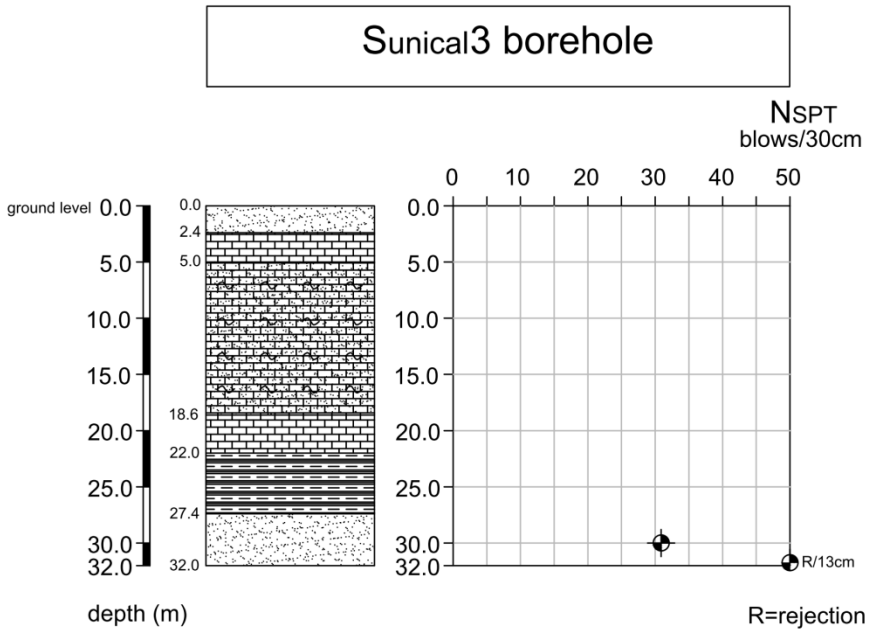

Fig.4.23 – Standard penetration test results at $S_{UNICAL}3$ borehole

4.3.3. Mènard pressuremeter tests

The Mènard pressuremeter tests were carried out in the evaporitic limestone and in the Miocene sandstone formation:

These tests provide the pressiometric modulus, E_M , and the limit pressure, p_{LIM}. The first one is calculated using Eq. (4.1) and refers to the "pseudo-elastic" part of the pressure-volume curve:

$$E_M = 2.66\, V_m \frac{\Delta p}{\Delta V} \tag{4.1}$$

where ΔV is the volume variation of the pressiometric cell owing to pressure variation applied Δp, and V_m is the average volume of the cell associated to ΔV .

The second parameter is calculated from the "high strains" part of the pressure-volume curve and using the "inverse of volumes" method.

The resulting values of E_M and p_{LIM} are reported in the Figs. 4.24 and 4.25.

In particular, for evaporitic limestone E_M varies from 10.2 to 27.8 MPa, whereas p_{LIM} ranges between 1.4 and 3.7 MPa. These values increase with depth.

For Miocene sand, E_M ranges between 25 and 47 MPa, whereas p_{LIM} varies between 3 and 4.5 MPa. The lowest values of E_M and p_{LIM} are obtained at depth greater than 45 m, along the vertical $S_{UNICAL}2$, where the soil is characterized by a high fine percentage.

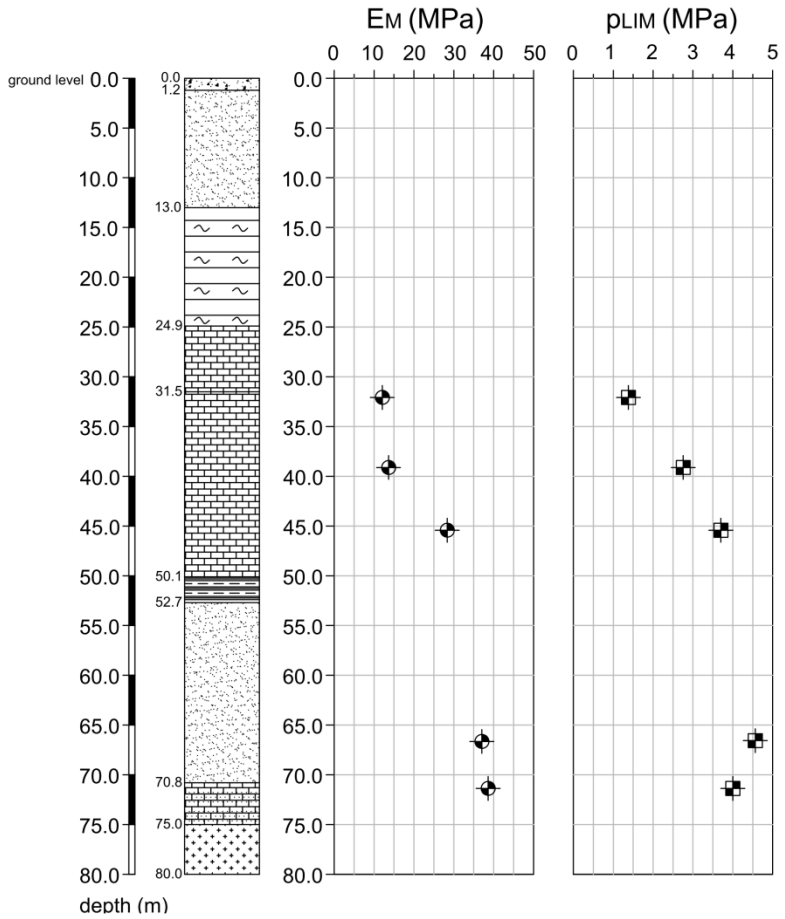

Fig.4.24 – Mènard pressuremeter test results at the vertical $S_{UNICAL}1$

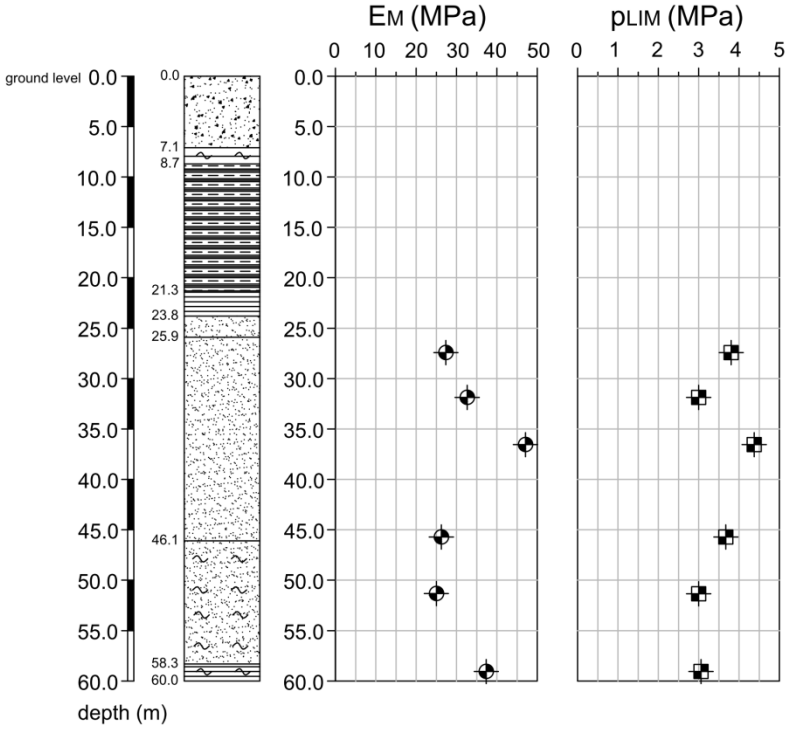

Fig.4.25 – Mènard pressuremeter test results at the vertical $S_{UNICAL}2$

4.3.4. Marchetti dilatometer tests

Four Marchetti dilatometer tests were carried out in the locations indicated in Fig. 4.16. The maximum depth of each test is reported in the following table.

test	max depth (m)
DMT1	10
DMT2	19
DMT3	19.4
DMT4	4.6

Tab.4.1 - Maximum depth reached by DMT tests

These locations were chosen in order to detect the main formations involved by the landslide. In particular, DMT1 mainly concerned the clay formation, DMT2 and DMT3 the evaporitic limestone and DMT4 the Miocene sandstone.

The parameters obtained from these tests are the soil index I_d, the horizontal pressure index K_d and the dilatometric modulus E_D. The first one takes account of the soil nature, the second one provides information about the loading history and the last one is related to soil deformability. By using some empirical relationships (Marchetti, 1980) several geotechnical parameters such as the undrained cohesion Cu and the overconsolidation ratio OCR for the cohesive soils, as well as the shear strength angle for the cohesionless soils, can be evaluated. In addition, the oedometric modulus M can be estimated for both soil types. DMT1 was located at the side of the Filogaso-Maierato road. As shown in Fig. 4.26, K_d is about 15 for the silty clay. This soil is characterized by values of the oedometric modulus M of order of 100 MPa, with Cu that ranges from 200 to 400 kPa. DMT2 was located close to the landslide toe. As shown in Fig. 4.27, the probe passed through a weak silty-clayey layer with M=2-6 MPa and Cu=10-20 kPa, which forms the landslide material.

Below a depth of 16 m, the soil can be classified as silty sand with mechanical properties (M=100-200 MPa) better than the upper layers.

As shown in Fig. 4.28, DMT3 profile shows the presence of a silty layer with a thickness of 6 m overlying the evaporitic limestone formation that extends to a depth of 17m. At the bottom of the profile, a clay layer is found. The I_d value for the evaporitic limestone is similar to that of DMT2, although in the former test the mechanic properties of the soils are higher than those of DMT2. For example, the oedometric modulus M exceeds 100 MPa. Lastly, DMT4 (Fig.4.29) only concerned the Miocene sand to a depth of 4.6 m, because the probe did not penetrate at greater depth due to a high resistance of this formation. According to the SPT and MPT results, this soil is characterized by good mechanical properties (e.g. M is of order of 500 MPa).

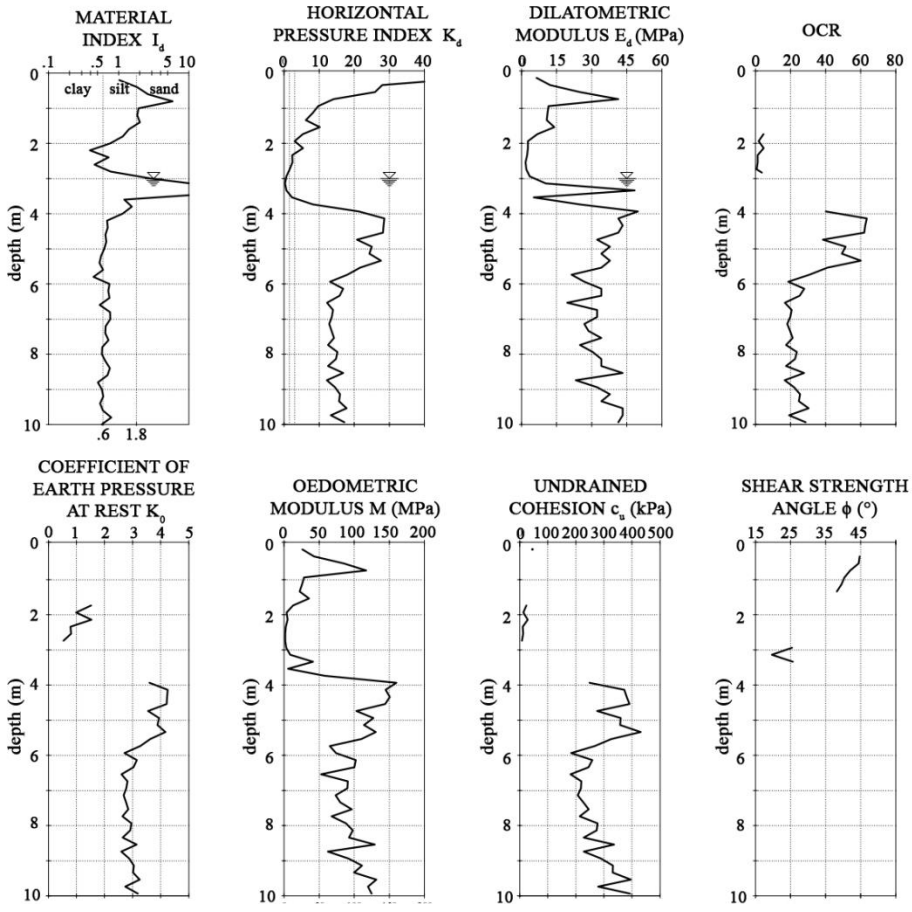

Fig.4.26 – DMT1 test results

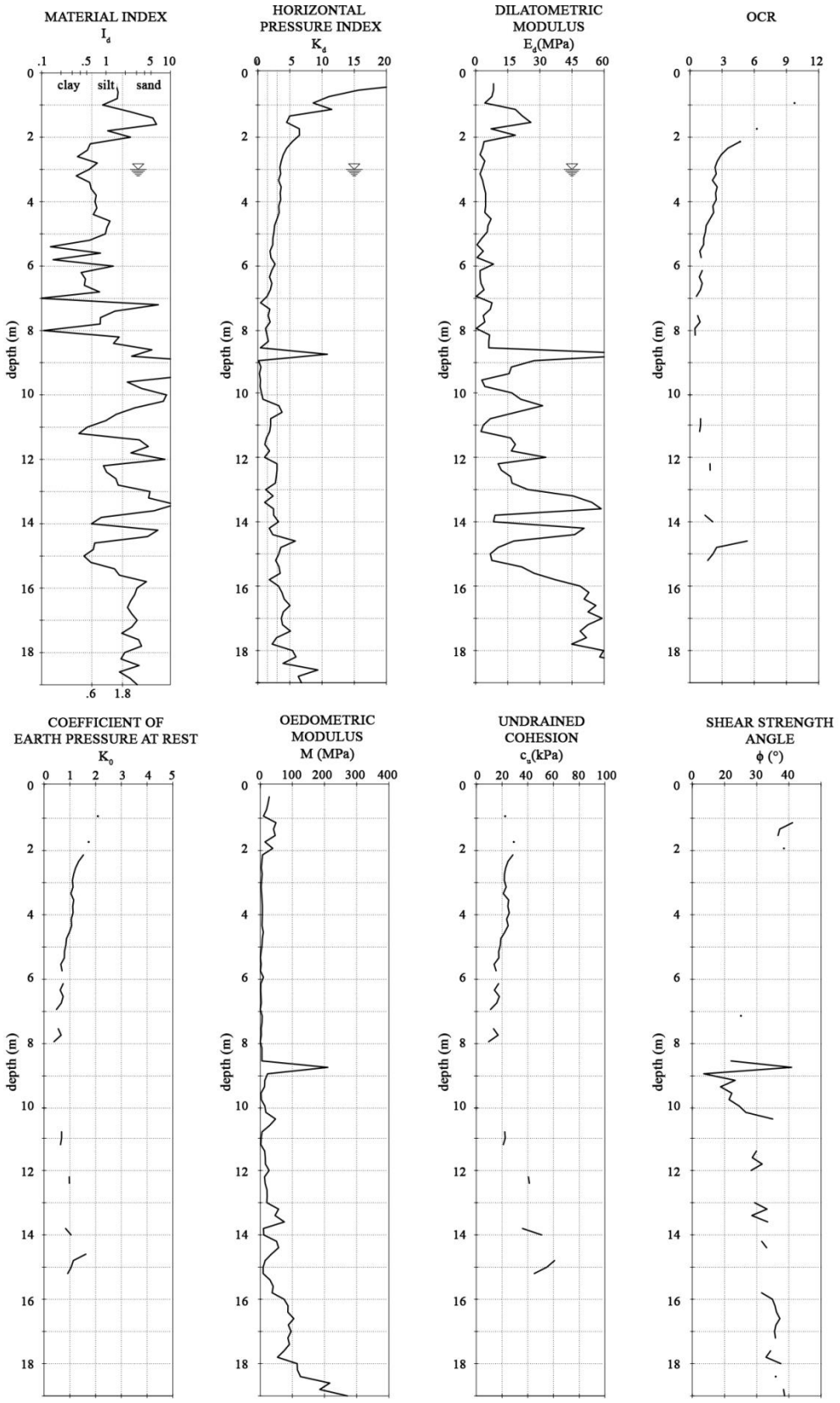

Fig.4.27– DMT2 test results

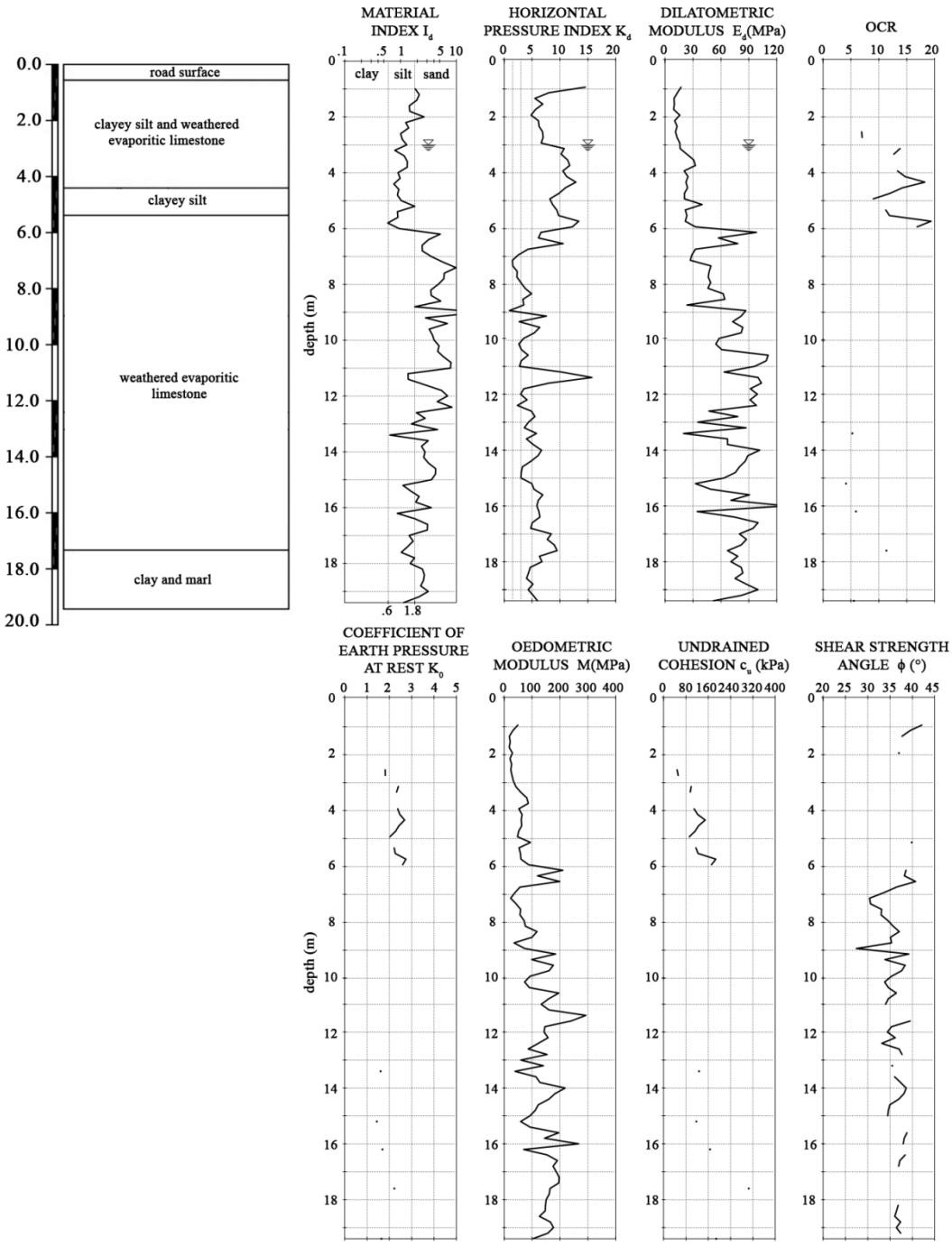

Fig.4.28– DMT3 test results

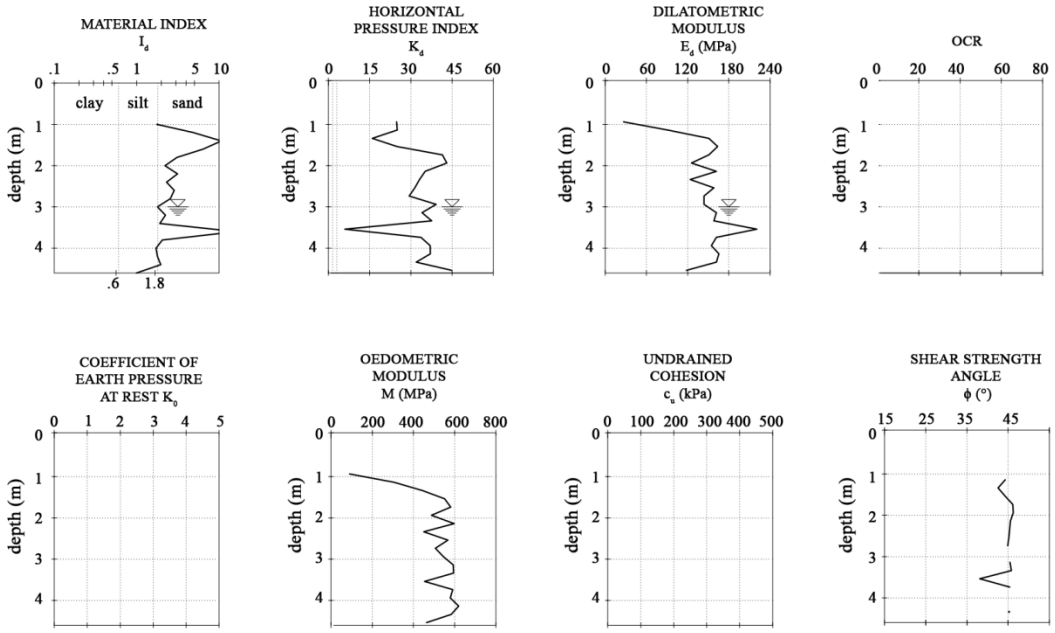

Fig.4.29– DMT4 test results

4.3.5. Piezometric measurements

As formerly mentioned, open pipe piezometers were installed inside V1 and V2 boreholes. In particular, the first one has three different uptakes at 18, 48 and 65 m in depth; the second one has two uptakes at 35 and 55 m in depth. As an example, the measurements performed on 27/04/2012 are shown in Tab.4.2.

borehole	piezometer depth (m)	measurement from ground level (m)
V1	18	--
	48	44.20
	65	63.40
V2	35	33.90
	55	33.90

Tab.4.2 - Piezometers installed inside the Unical boreholes

Furthermore, an electric transducer inside V2 was installed at 18 meters in depth (in the Miocene clay), but the respective measurements are not available. Other piezometers of Casagrande type were installed inside the CNR-IRPI boreholes.

Two of these latter piezometers, i.e. S1 (located at upper part of the slope) and S5 (located at lower part, on the left side of the landslide body) are useful to define the position of groundwater before the occurrence of the landslide.

Piezometer S1 (Mosto locality):

This piezometer is composed of three Casagrande probes (a,b,c) installed at different depth. The available measurements are shown in table 4.3 and in Fig.4.30. As it can be seen, a groundwater table was found at a depth of about 44m from the ground surface.

	Pipe a	Pipe c	Pipe b
depth	7.70 m	26.00 m	67.00 m
DATE	depth of groundwater level [m]		
16/10/2010	-	-	44.95
02/11/2010	-	-	44.40
19/11/2010	-	-	44.24
07/12/2010	-	-	43.73
21/12/2010	-	-	43.70
21/01/2011	-	-	42.55
31/01/2011	-	-	42.40
27/03/2012	-	-	43.60
27/04/2012	-	-	43.50

Tab.4.3 - Groundwater level measurements at piezometer S1

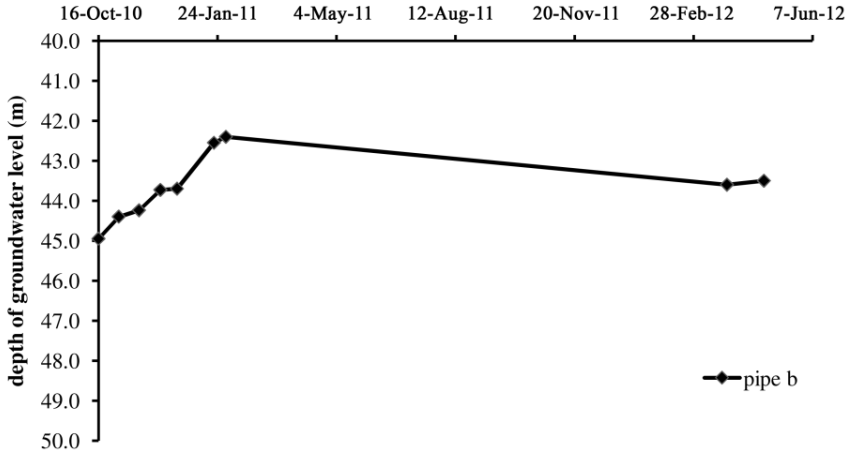

Fig.4.30– Piezometric measurements at piezometer S1

Piezometer S5 (left side of the landslide body):

This piezometer is composed of three Casagrande probes (a,b,c).

The measurements are reported in table 4.4 and in Fig. 4.31:

	Pipe a	Pipe c	Pipe b
depth	4.80 m	18.20 m	41.40 m
DATA	depth of groundwater level [m]		
16/10/2010	-	6.65	29.80
02/11/2010	4.55	5.85	-
19/11/2010	-	5.65	29.65
12/12/2010	-	5.15	29.55
21/12/2010	4.70	5.50	29.42
21/01/2011	4.75	4.90	29.40
31/01/2011	4.18	4.62	29.25
27/03/2012	-	5.55	28.97
27/04/2012	-	5.7	28.84

Tab.4.4 - Groundwater level measurements at piezometer S5

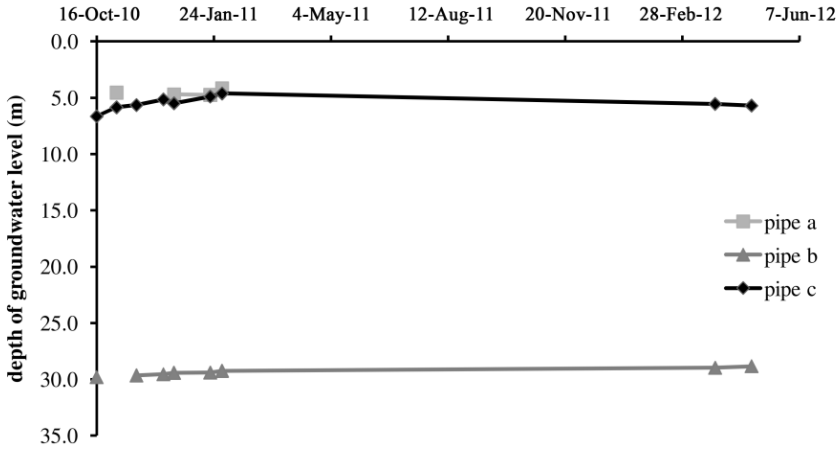

Fig.4.31- Piezometric measurements at piezometer S5

From these data, it seems that two different aquifers take place in the subsoil, with ground table located at a depth of about 5 m and 29 m, respectively.

Finally, it is relevant to point out that the piezometer installed in the $S_{UNICAL}3$ borehole and located on the landslide body, signaled the presence of a groundwater at a depth of 20.2 m from the ground surface.

4.3.6. Laboratory tests

The laboratory tests were carried out on undisturbed specimens and on cores extracted during drilling. The available results are reported below for each soil considered, from the shallowest one (Pliocene sand) to the deepest one (Miocene sand).

PLIOCENE SAND

From the grain size viewpoint, this soil can be classified as silty sand.

Based on the Atterberg limits, the material is an inorganic clay with medium plasticity.

EVAPORITIC LIMESTONE

Evaporitic limestone is the most heterogeneous lithotype, due to the different degree of weathering which affects this material. According to Fig.4.32, the grain size distribution of this material varies from silty sand to sandy clayey silt. Moreover, the material can be substantially classified as an inorganic clay with low-medium plasticity (Fig.4.33). The activity index is always less than 0.75. Therefore, the material can be defined as inactive.

Average value of porosity, n, and unit weight, γ, are 0.38 and 19.5 kN/m^3, respectively.Furthermore, direct shear tests performed on undisturbed specimens provide a linear failure envelope (Fig.4.34). The peak strength parameters are c' =15 kPa and ϕ'=36°, whereas the value of these parameters at residual are $c'_r \cong 0$ and ϕ'_r =28°.

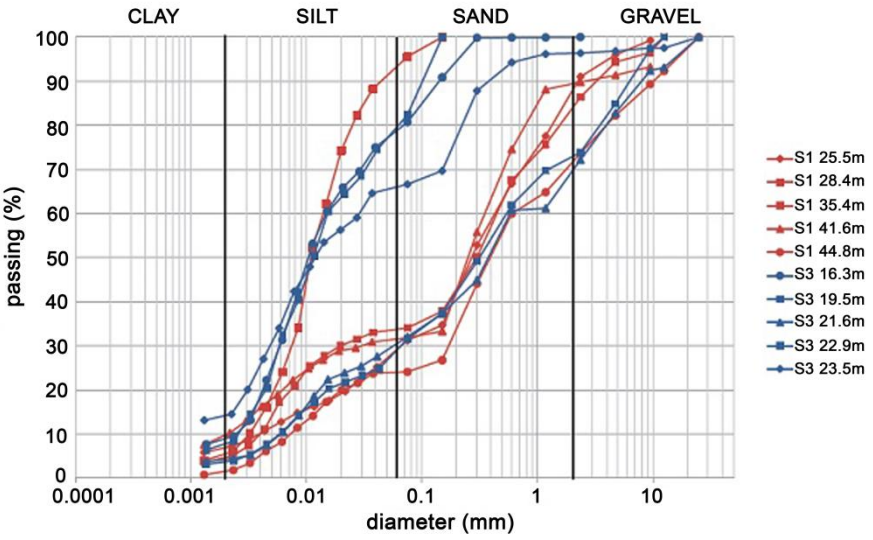

Fig.4.32– Grain size distribution available for evaporitic limestone

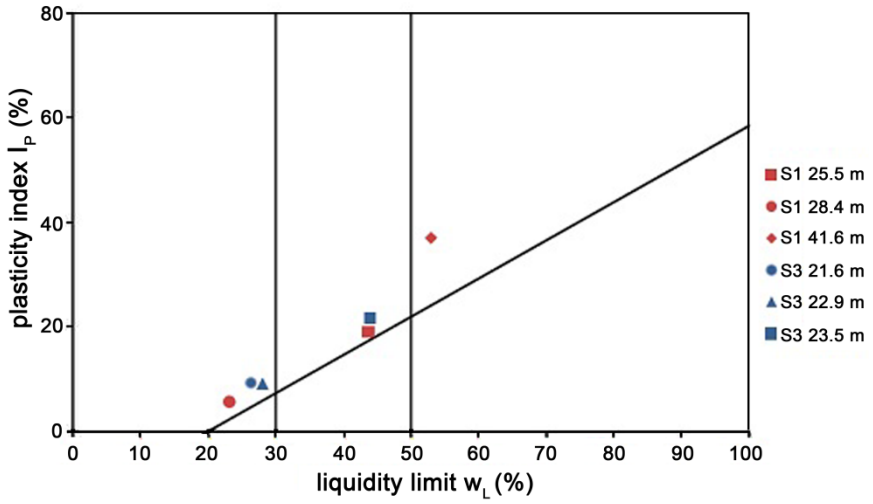

Fig.4.33– Casagrande plasticity chart for the evaporitic limestone

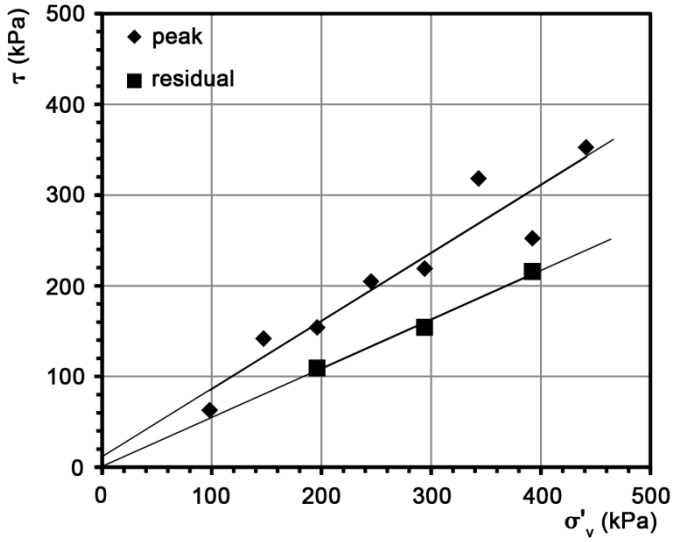

Fig.4.34– Direct shear tests for the evaporitic limestone

MIOCENE CLAY

The experimental results show that the soil can be classified as a clay with silt (Fig. 4.35), and as an inorganic clay with high plasticity (Fig.4.36). The activity index is 0.75-1.25 and which corresponds to a normally active material.

Average value of porosity, *n*, and unit weight, γ, are 0.56 and 18.2 kN/m^3, respectively. In addition, the saturation degree S is close to unity.

From the oedometric test results (Fig. 4.37), average values of the compression ratio RR and the swelling ratio SR are 0.22 and 0.036, respectively.

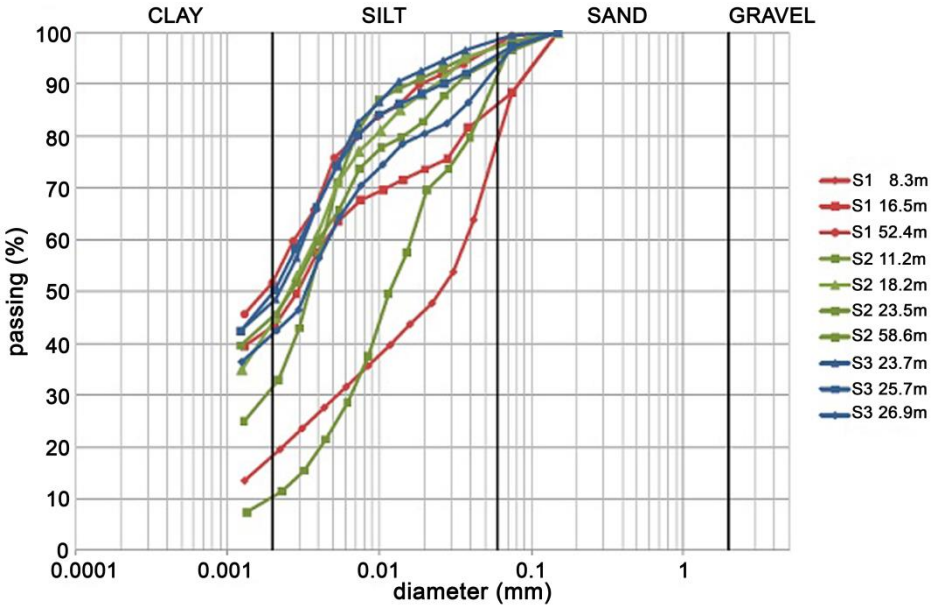

Fig.4.35– Grain size distributions for Miocene clay

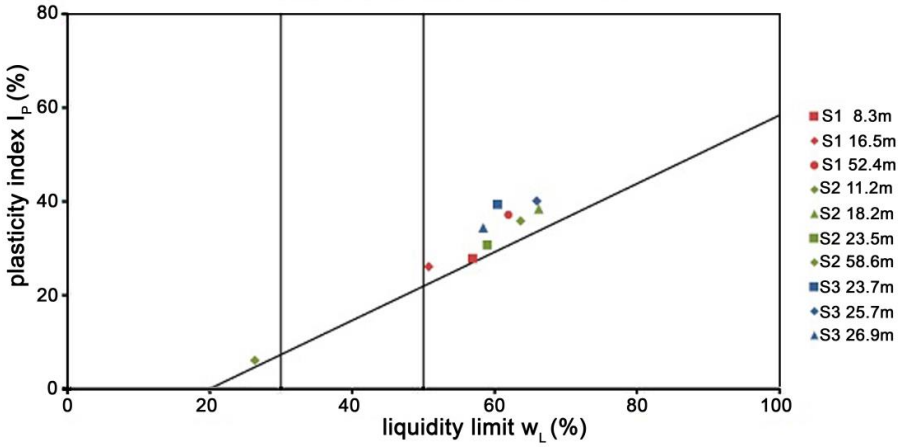

Fig.4.36– Casagrande chart for Miocene clay

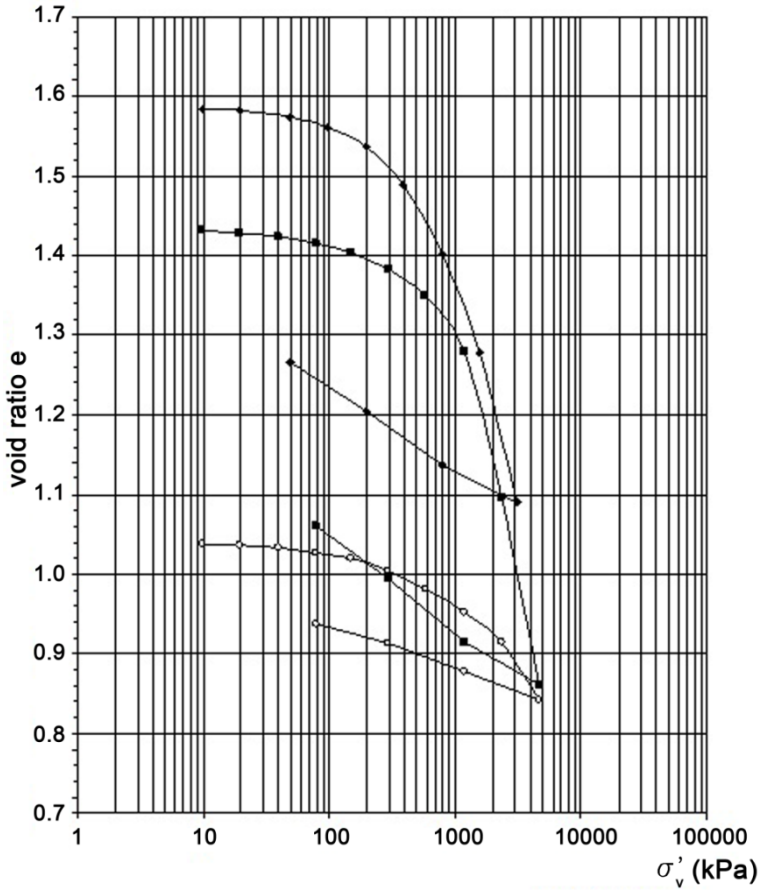

Fig.4.37– Oedometric test results for the Miocene clay

Direct shear tests on undisturbed specimens provided the peak parameters c'=57 kPa and ϕ'=25° and residual ones $c'_r \cong 0$ and ϕ'_r=13° (Fig.4.38).

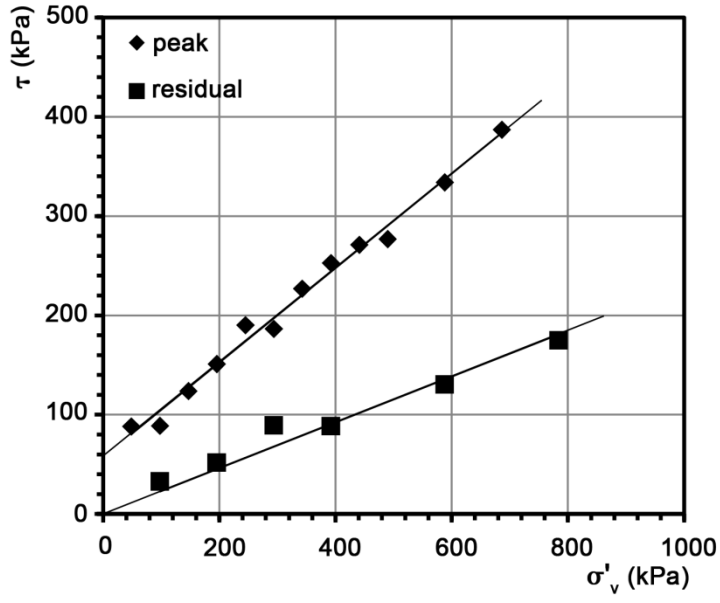

Fig.4.38– Direct shear tests for the Miocene clay

MIOCENE SAND

According to the grain size distribution documented in Fig.4.39, this formation appears quite homogeneous and can be classified as gravelly sand with silt. The Atterberg limits, obtained from the samples with higher fine percentage, define this soil as an inorganic clay with medium-low plasticity (Fig.4.40).

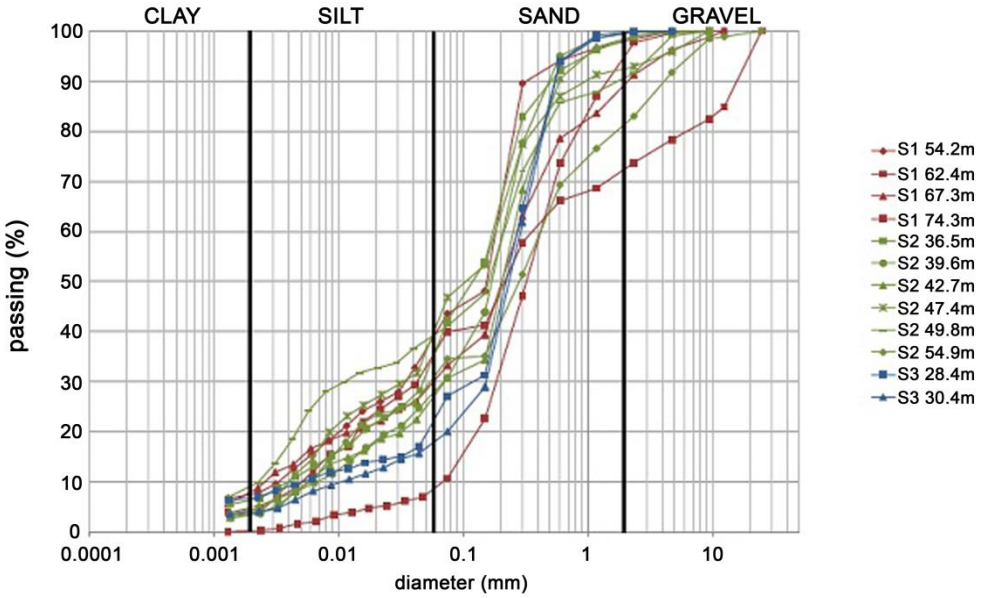

Fig.4.39– Grain size distributions for Miocene sand

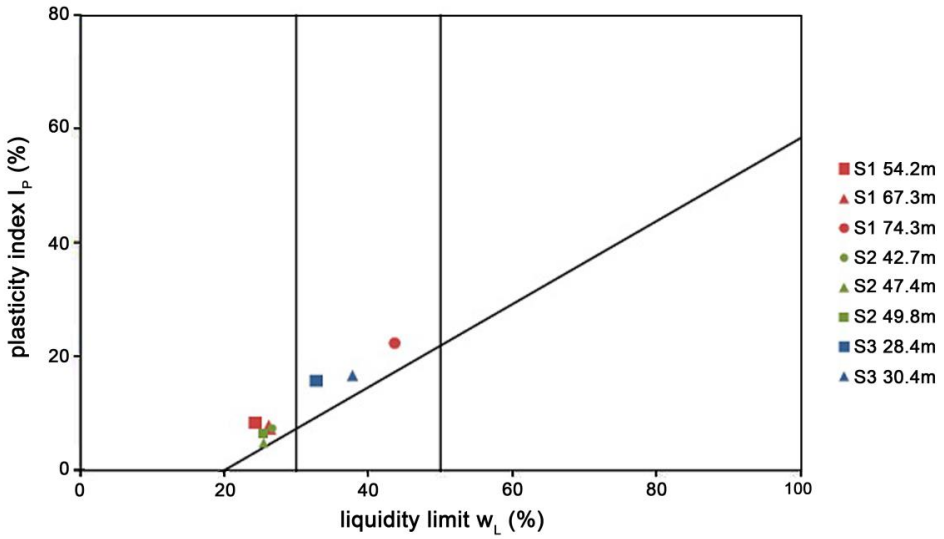

Fig.4.40– Casagrande chart for Miocene sand

4.4. The geotechnical model

The geotechnical model is built on the A-A cross section (Fig. 4.41), the trace of which is shown in Fig. 4.42.

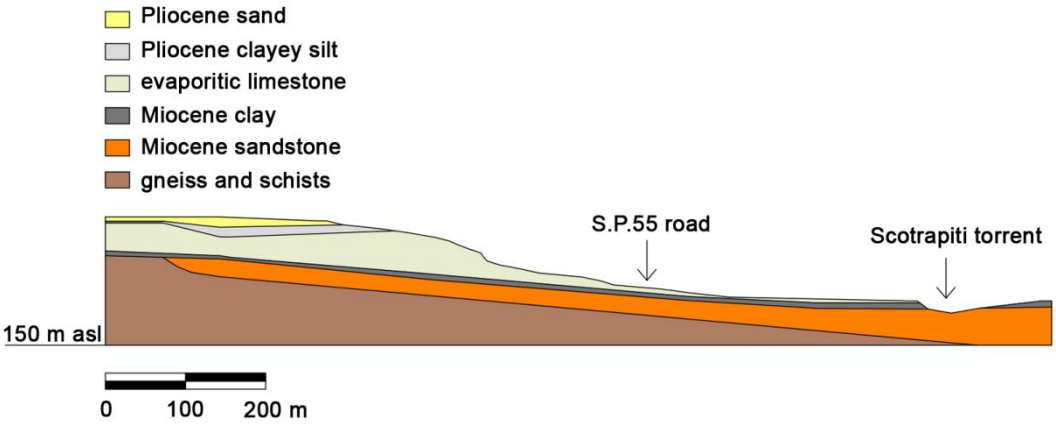

Fig.4.41–cross section A-A

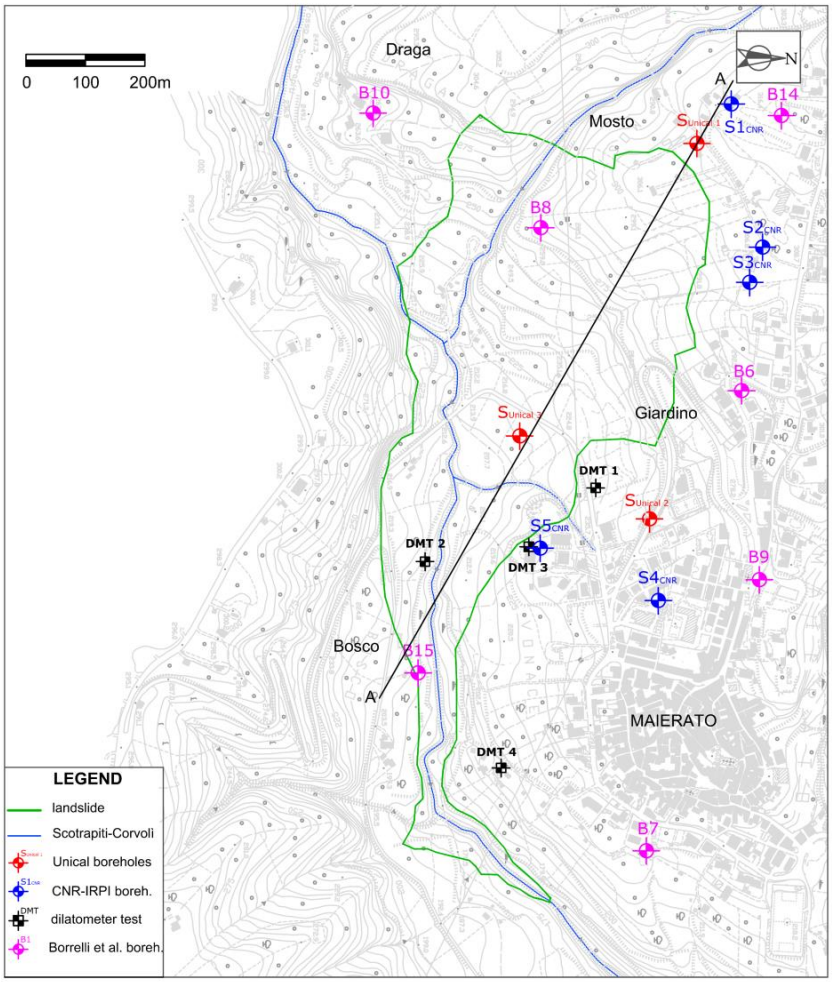

Fig.4.42– Trace of the cross section A-A

A comparison of the cross-section considered before and after the landslide is provided in Fig.4.43.

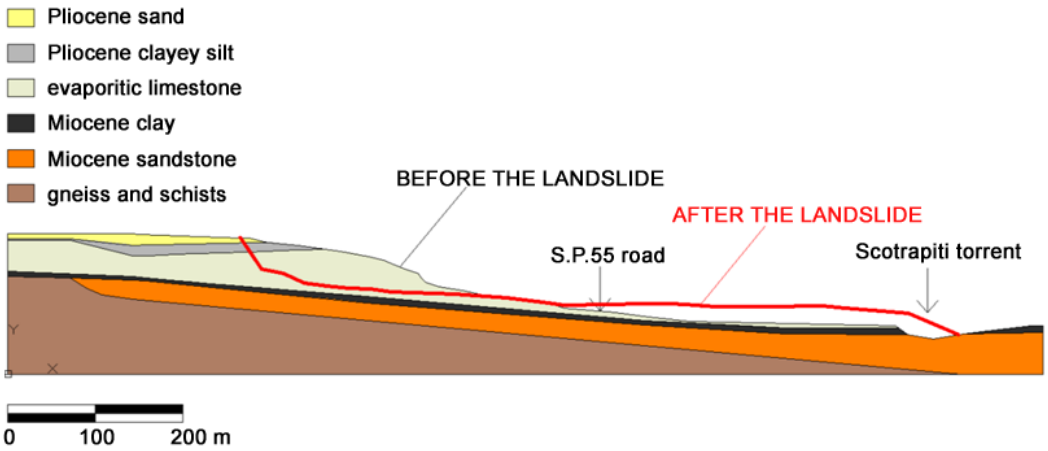

Fig.4.43– Comparison between cross-section A-A before and after the landslide

On the basis of the available results from the laboratory and field tests, the geotechnical parameters assigned to each material are reported in the table 4.5. In this connection, it is worth noting that in the numerical analyses, an elasto-plastic model with Mohr-Coulomb yield criterion is assumed to simulate the behaviour of all the soils involved with exception of the bedrock (formed by gneiss and schist) for which an elastic model is adopted.

The values of the coefficient of permeability, *k*, derive from some Lefranc tests documented in a work by Gattinoni et al. (2011).

Material	γ (kN/m^3)	γ_{sat} (kN/m^3)	c'_p (kPa)	ϕ'_p (°)	ϕ'_r (°)	E' (MPa)	ν	k (m/sec)
Pliocene sand	18	19	0	37	31	20	0.35	$1\cdot10^{-7}$
Pliocene clayey silt	18	19	0	25	18	20	0.35	$1\cdot10^{-9}$
evaporitic limestone	18	19	15	36	28	50	0.35	$1\cdot10^{-7}$
Miocene clay	17	18	57	25	13	18	0.40	$1\cdot10^{-9}$
Miocene sandstone	19	20	0	45	-	100	0.40	$8\cdot10^{-8}$
gneiss and schist	20	20	-			100	0.40	$3\cdot10^{-8}$

Tab.4.5 - Geotechnical parameters adopted in the numerical analyses

4.5. Rainfall

Rainfall was considered the main triggering cause of the Maierato landslide. To support this convincement, rainfall recorded at Vibo Valentia rain-gauge station (elevation 498 m a.s.l.), which is approximately located at a distance of 10 km from Maierato (Fig. 4.44), is examined.

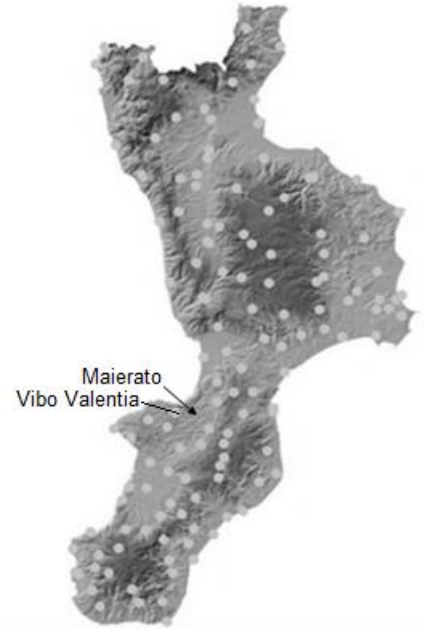

Fig.4.44– Location of Vibo Valentia rain-gauge station

Daily rainfall data recorded from 1 September 2009 to 15 February 2010 (date of the landslide occurred) are shown in the graph of Fig.4.45 and in table 4.6.

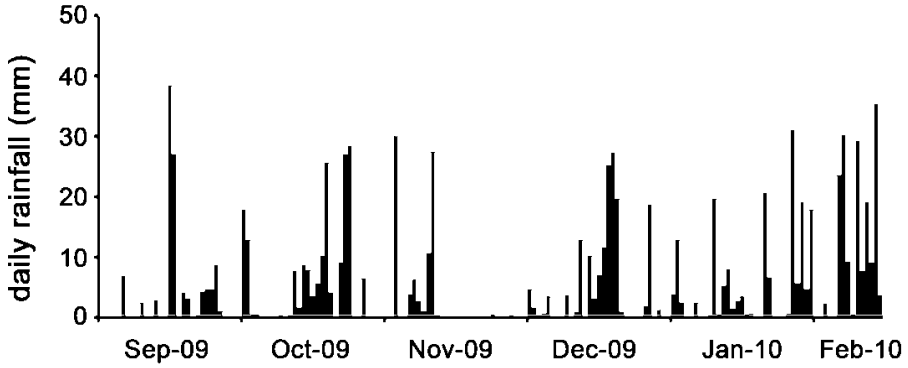

Fig.4.45– Daily rainfall recorded at Vibo Valentia rain-gauge station

Day	September 2009	October 2009	November 2009	December 2009	January 2010	February 2010
1	-	18.0	-	4.8	4.0	-
2	-	13.0	-	1.8	13.0	-
3	-	0.6	30.2	0.4	2.6	2.4
4	-	0.6	0.2	0.8	-	-
5	-	0.2	-	3.6	-	-
6	7.0	-	4.0	-	2.6	23.8
7	-	-	6.4	0.2	-	30.4
8	-	0.2	2.8	0.2	-	9.4
9	-	0.4	1.2	3.8	0.4	0.6
10	2.6	0.2	10.8	-	19.8	29.4
11	-	0.4	27.6	1.0	0.6	7.8
12	-	7.8	0.4	13.0	5.4	19.2
13	3.0	1.8	-	-	8.2	9.2
14	-	8.8	-	10.4	1.6	35.6
15	-	8.0	-	3.2	2.8	3.8
16	38.6	3.6	-	7.2	3.6	
17	27.2	5.8	-	11.8	0.6	
18	-	10.4	-	25.4	0.8	
19	4.2	25.8	-	27.4	0.2	
20	3.2	4.2	-	19.8	-	
21	-	-	-	1.0	20.8	
22	0.4	9.2	-	-	6.8	
23	4.4	27.2	-	-	0.2	
24	4.8	28.6	0.6	-	-	
25	4.8	-	0.2	-	-	
26	8.8	-	0.2	2.0	0.8	
27	1.2	6.6	0.2	18.8	31.2	
28	-	0.2	0.4	-	5.8	
29	-	-	0.2	1.4	19.2	
30	-	-	-	-	4.8	
31	-	-	-	-	18.0	
Total	**112.0**	**181.6**	**85.4**	**158.0**	**173.8**	**171.6**

Tab.4.6 - Rainfall recorded at Vibo Valentia rain-gauge station (the data are in millimeters)

As it can be seen, although significant, rainfall was not exceptional. However, it was fairly distributed with time.

By comparing the monthly rainfall for the period under consideration (1 September 2009-15 February 2010) to the historical average monthly rainfall (from 1919 to 2010) recorded in the same period at Vibo Valentia station, it results that the rainfall before the landslide is considerably over the average value.

This occurs also in terms of cumulative rainfall (Fig. 4.46) with a surplus approximatively of 35% (Table 4.7).

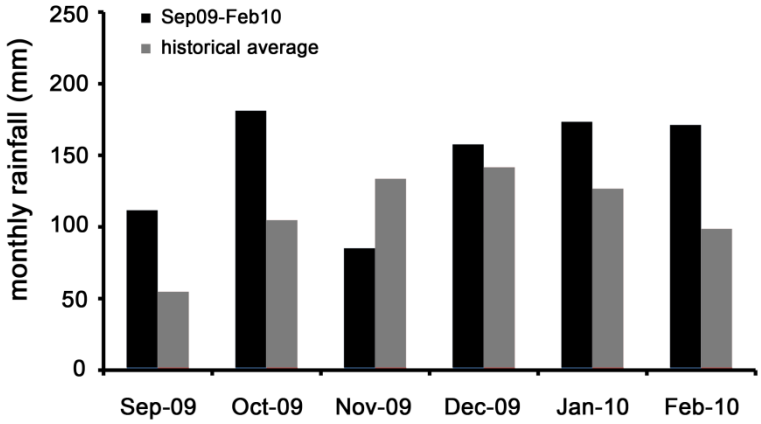

Fig.4.46–Monthly rainfall at Vibo Valentia rain-gauge station

Vibo Valentia rain-gauge station		
h_{CUM} 09-10	h_{CUM} average	surplus
882 mm	651 mm	+35.4%

Tab.4.7 - Comparison of cumulative rainfalls in the period 1 September -15 February

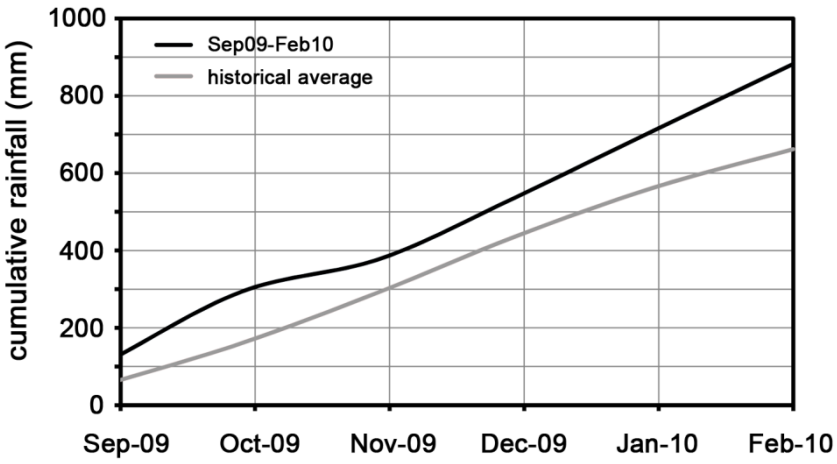

Fig.4.47– Comparison of cumulative rainfall at Vibo Valentia station,
in the period 1 September -15 February

It is also relevant to note from Fig. 4.48 that, two consecutive years with rainfall comparable with that recorded in the years 2009-2010 (black arrow), only occurred twice, i.e. in the periods 1938-1940 and 1944-1947 (white arrows).

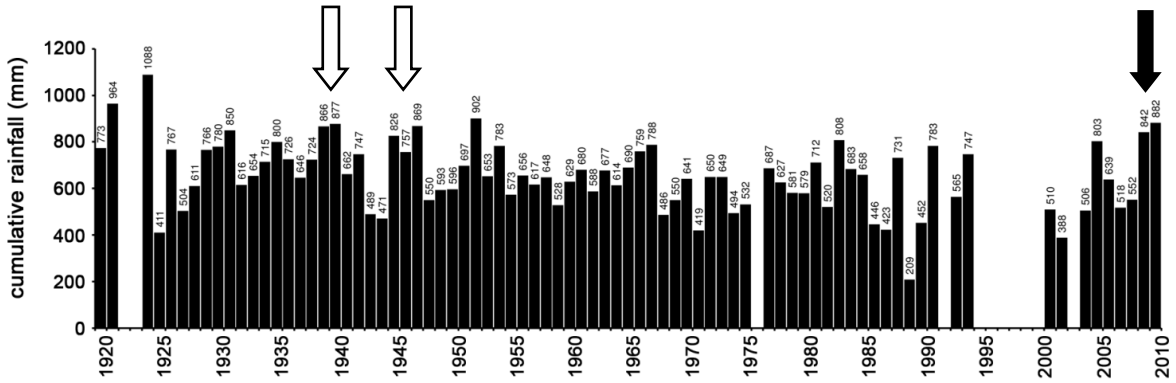

Fig.4.48- Yearly rainfall recorded at Vibo Valentia station in the period Sept-Feb, since 1919

In conclusion, although abundant, the rainfall recorded (in the period from 1 September 2008 to 15 February 2010) was not exceptional. Other times in past, it had been recorded significant events like those occurred before the landslide on 15 February 2010. However, it is relevant to note that at the date of the landslide the area was affected by a different urbanization than the years 1938-1947, which may have caused further water supplies in the study area.

In particular, a big industrial zone was recently built up at short distance from the crown of the landslide body.

4.6. Finite element analysis

Unfortunately, the slope affected by the landslide was not monitored before the failure. Therefore, the groundwater regime at the moment of the landslide is unknown. In the present study, it is back-estimated considering as a starting groundwater level that measured by the piezometers installed after the landslide (see §4.4.5). In particular, this starting level is quite deep in the upper part of the slope and close to the ground level in the lower part. The groundwater level is progressively increased until a failure mechanism similar to that really observed is achieved. Two parameters are controlled to this purpose: the plastic shear strains in the slope and the safety factor *SF*. The first one defines the failure surface, whereas the second one allows the critical position of groundwater level to be estimated. This latter, in fact, is that for which *SF*=1.

The safety factor is calculated using the classic equation:

$$SF = \frac{\int_S \tau_f \, dS}{\int_S \tau dS} \tag{4.2}$$

where τ_f is the available shear strength of the soil and τ is the mobilized one along the failure surface, *S.*

Fundamental information are extrapolated from movies and photographs caught by local people (see Figs. 4.12 e,f,g). From which, it was possible to assess the position of the slip surface during the failure process.

The numerical analyses are performed by using the finite element code Tochnog (Roddeman, 2013).

As it was already said, considering the available soil properties, the elasto-perfectly plastic constitutive model is employed to model the behaviour of the soils involved with the exception of the bedrock for which an elastic behaviour is assumed. The mesh adopted in the calculations (Fig.4.49) consists of 17197 triangular elements with three nodes and one Gauss point (CST element).

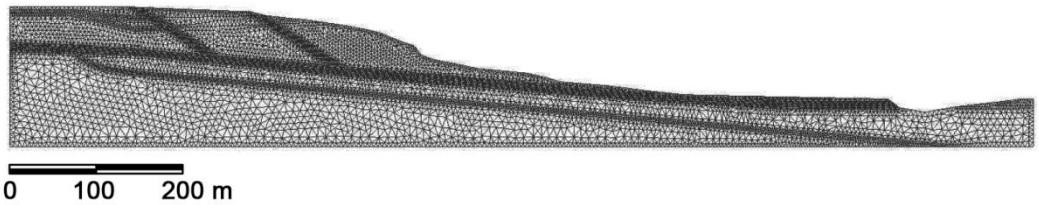

Fig.4.49 – Finite element mesh adopted

The base of the mesh is assumed to be fully impervious and fixed, and the lateral sides are constrained by vertical rollers. A hydraulic head is also imposed at the lateral boundaries, taking into account the available piezometric measurements and the presence of the Scotrapiti torrent at the foot of the slope.

Due to the uncertainties for defining the geologic history of the site and the lack of specific geotechnical data, the initial stress state within the slope is reproduced by increasing progressively the gravity acceleration up to 9.81 m/s^2 (gravity loading) under the assumption that the soils behave as an elastic-perfectly plastic material with Mohr–Coulomb failure criterion.

At the end of the gravity loading, the associated displacements and strains are reset to zero. As already mentioned, slope failure (SF=1) is produced by increasing in the groundwater level from the initial position provided by the piezometric measurements performed after the landslide.

As listed below, four analyses are carried out in accordance with the shear strength parameters adopted (see table 4.5):

1. peak shear strength parameters are assumed for all the soils;
2. residual shear strength parameters are used for the Miocene clay layer, whereas peak strength parameters are used for the other soils;
3. residual shear strength parameters are used for the Miocene clay layer and the evaporitic limestone, whereas peak strength parameters are considered for the other soils;
4. residual shear strength parameters are imposed for two shear zones, according to the hypothesis that they represent pre-existing slip surfaces. Peak parameters are used for the other soils.

FIRST ANALYSIS

The first analysis is carried out using the peak shear strength parameters for every soil involved. The result in terms of plastic strains shows that these latter are negligible and no significant failure mechanism is produced, even if the groundwater level reaches the ground surface.

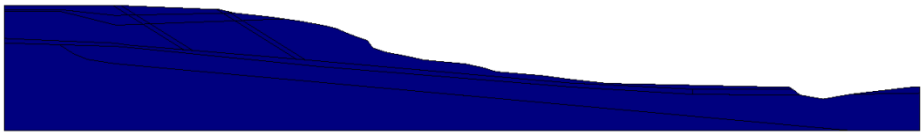

Fig.4.50 - Plastic shear strains are negligible using the peak parameters for all the soils

Therefore, using the peak strength parameters results impossible to account for the failure phenomenon occurred in the slope.

SECOND ANALYSIS

Apart from the Miocene clay layer in which the residual strength parameters are assumed, for the other materials the peak strength parameters are used.

By increasing the groundwater level, plastic strain localizes in the clay layer and involves also the overlying soil. Therefore a slip surface develops in the slope. However, its position is different from that observed on 15 February 2010, as documented in Fig. 4.51 and in the attached photo.

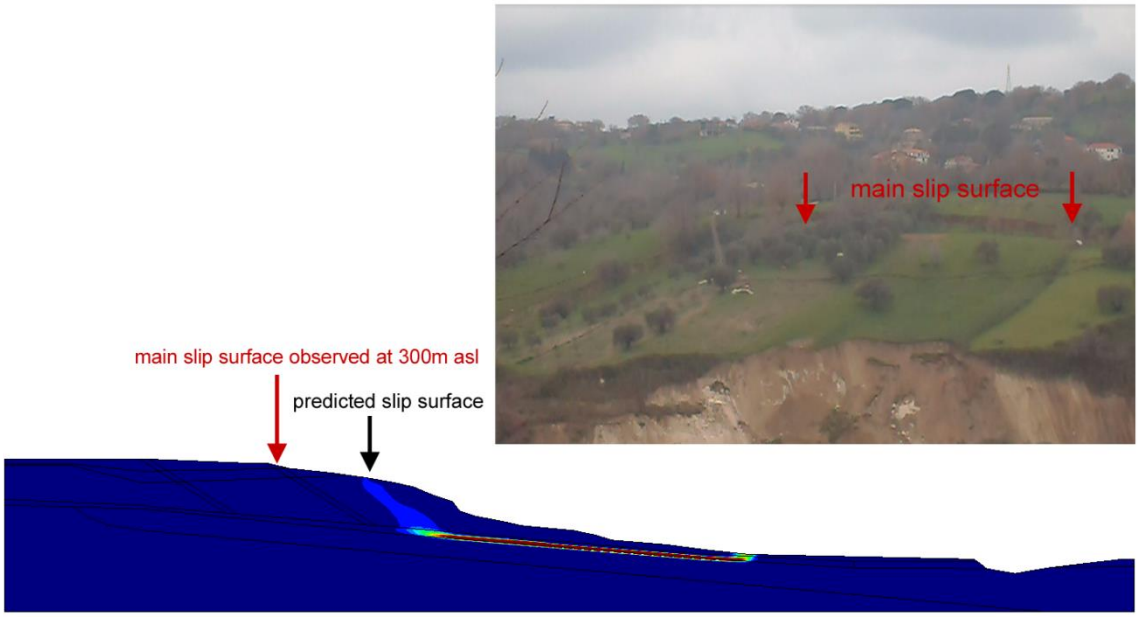

Fig.4.51- A different slip surface than that observed one (indicated by red arrows) is found in the second analysis

In conclusion, assuming the residual strength parameters for the Miocene clay layer only, it is not possible to completely predict the observed phenomenon.

THIRD ANALYSIS

The residual strength parameters are used for both the Miocene clay layer and the evaporitic limestone formation. On the contrary, the peak strength parameters are assumed for the other materials. The results of this analysis are synthetized in Fig.4.52. A failure mechanism can be defined by a shear zone which develops into the clay layer and the overlying soils. Likewise the previous analysis, the landslide body is different from that really observed (Fig.4.52).

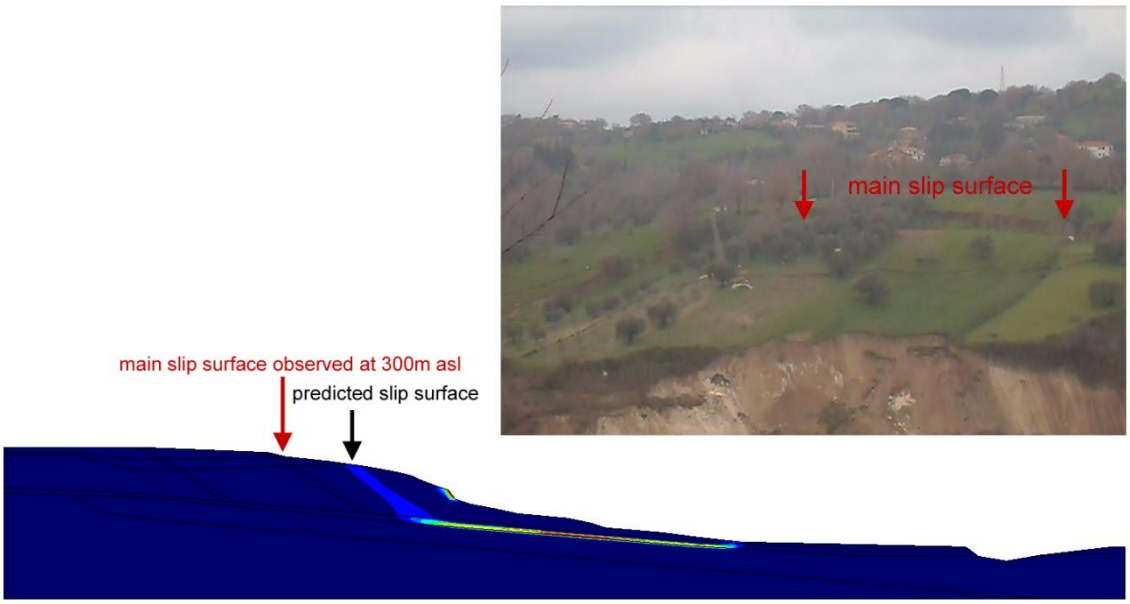

Fig.4.52 - A different slip surface than the observed one (indicated by red arrows) is found in the third analysis

Therefore, using the residual strength parameters for both the Miocene clay layer and the whole evaporitic limestone formation, the slip surface observed *in situ* cannot be obtained.

FOURTH ANALYSIS

The last analysis is performed considering two thin shear zones that develop in the upper part of the slope and are connected with the clay layer. The residual strength parameters are imposed to the soils in these zones for simulating two pre-existing slip surfaces (see Fig. 4.53). The residual strength parameters are also assigned to the Miocene clay layer, whereas the peak strength parameters are assumed for the rest of the soils involved by the landslide.

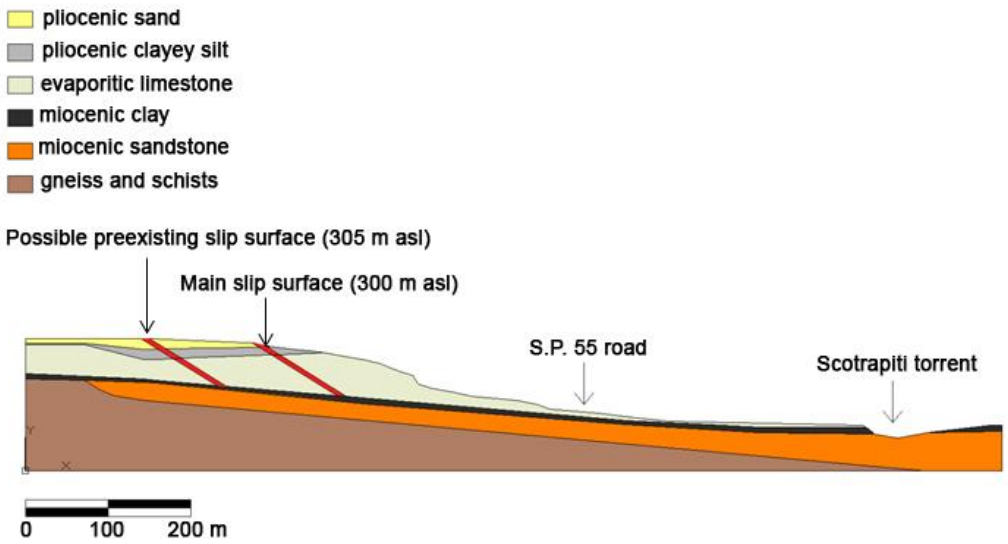

Fig.4.53 – Slope cross-section with an indication of the assumed shear zones (red bands)

The results of the FEM analysis are synthetized in Fig.4.54. Specifically, two slip surfaces can be observed. The main surface is indicated by red arrows and was the first to be activated (Fig. 4.12e). Along this entire surface the soil strength is at residual. The secondary failure surface develops into the clay layer with residual strength and in the overlying soils, the strength of which is at peak. This finding is completely consistent with what really observed. (see photo attached to Fig.4.54).

In other words, the results show that the main slip surface is a pre-existing slip surface, whereas, the secondary one is newly formed. It is worth noting that, the other pre-existing slip surface, indicated by orange arrows, was not involved by the landslide occurred on 2010.

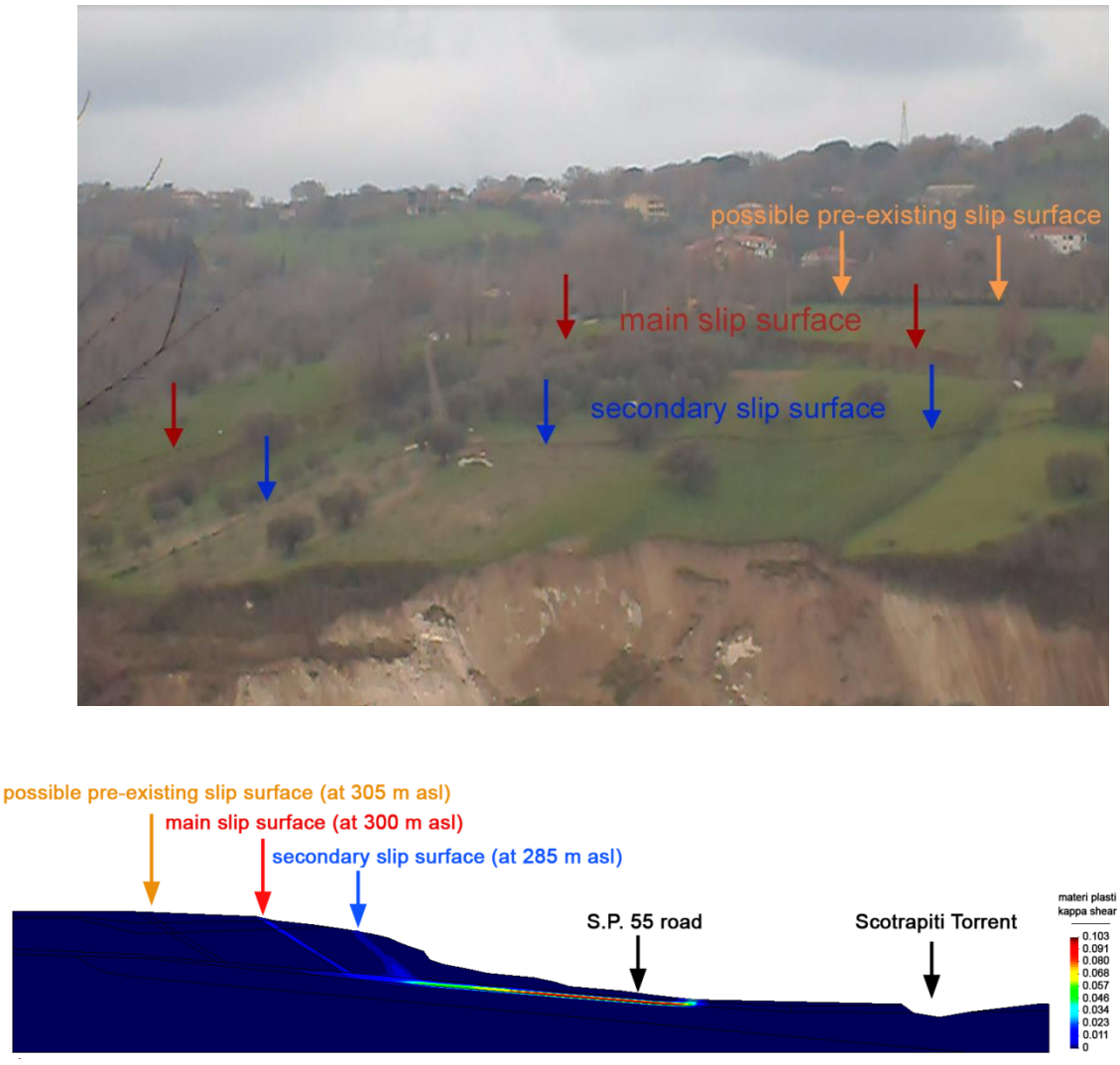

Fig.4.54 - Comparison between the observed slip surfaces and that obtained by the FEM analysis

The failure process is documented in the following figures. Specifically, increasing the groundwater level, failure starts at the slope toe and then moves backward (Figs.4.55-4.57).

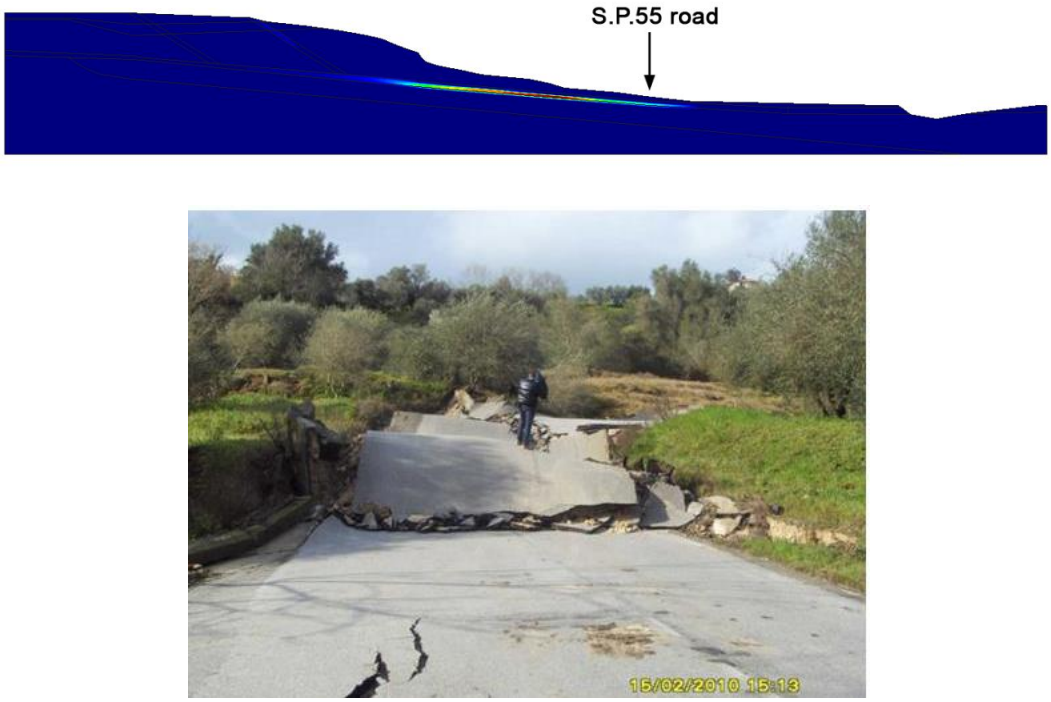

Fig.4.55 - Deformation starts from the toe of the slope where the road SP55 is located.

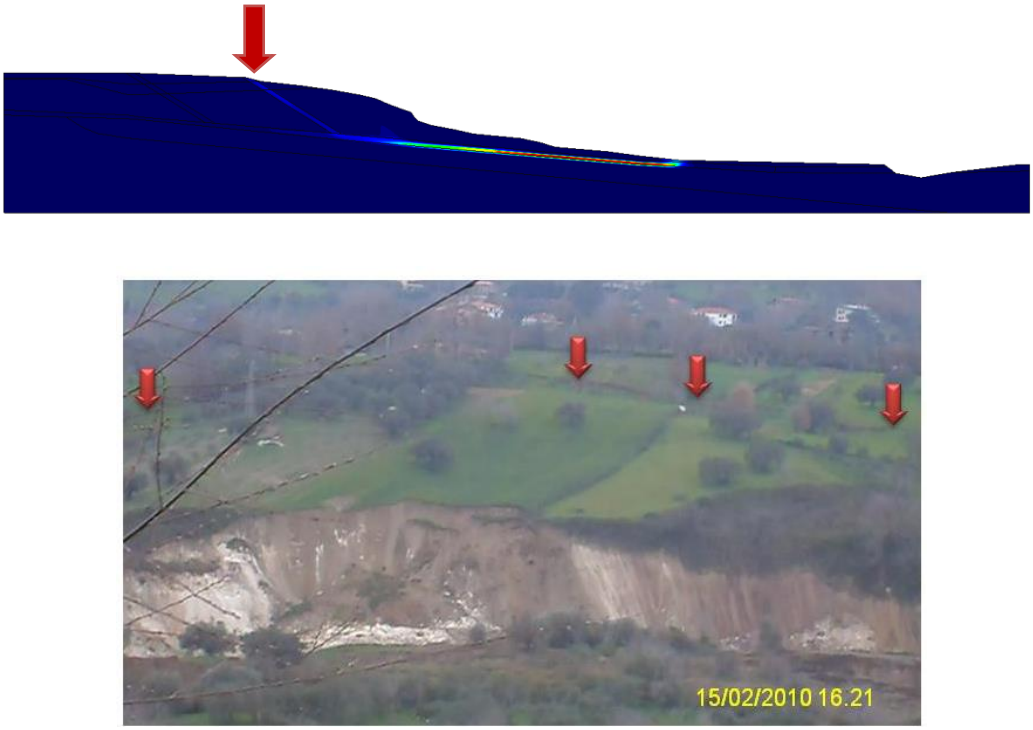

Fig.4.56 - The main slip surface (red arrows) is first activated.

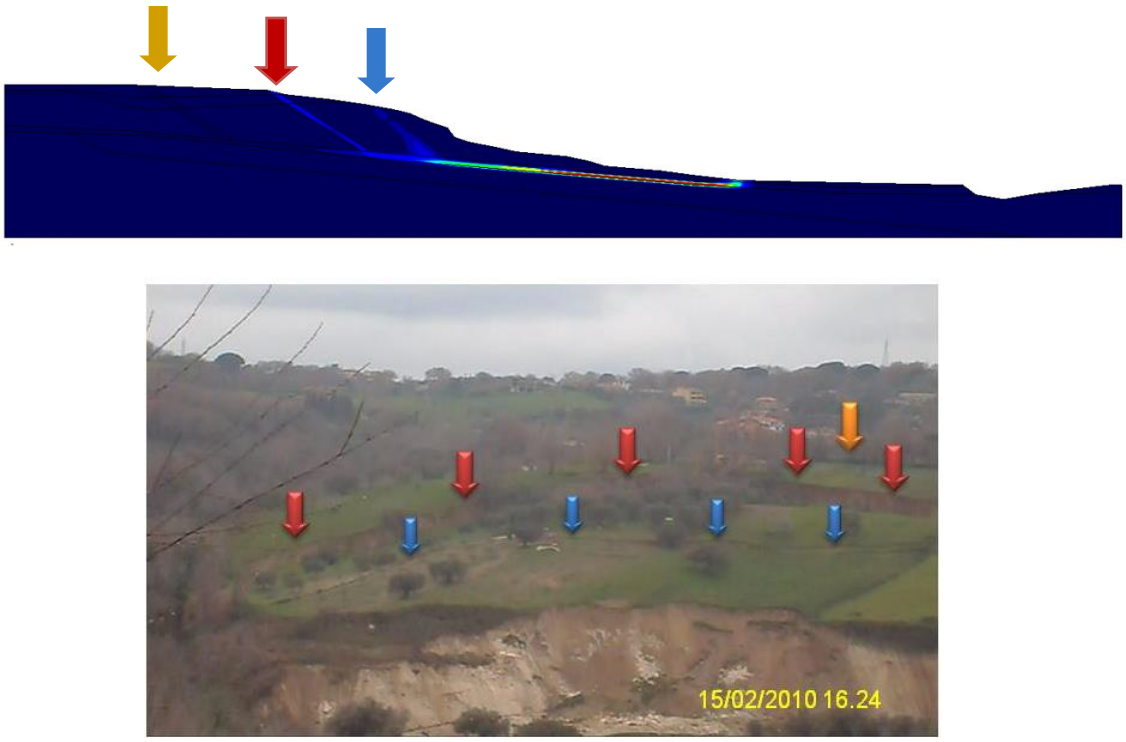

Fig.4.57 - The secondary slip surface (blue arrows) appears after the main one. The other possible pre-existing slip surface (orange arrow) is not affected by failure.

Failure surface appears on the ground level at an elevation of 300 m asl (Fig.4.56). A secondary failure surface is located at an elevation of 285 m asl, like it was really observed (see the photo attached to Fig.4.57).

It is relevant to note that the analysis also confirms the evidence that the second pre-existing surface (orange arrow) is not involved by the landslide (Fig.4.57).

Fig.4.58 shows the critical position of the groundwater level provided by the analysis. As it can be observed, it is about 33 m in depth in the upper part of the slope and it reaches the ground surface in the lower part.

Lastly, for the sake of completeness, Figs.4.59 and 4.60 show the soil displacement field and the deformed mesh (in an exaggerated scale) to point out the soil mass involved by the landslide and the failure mechanism occurred.

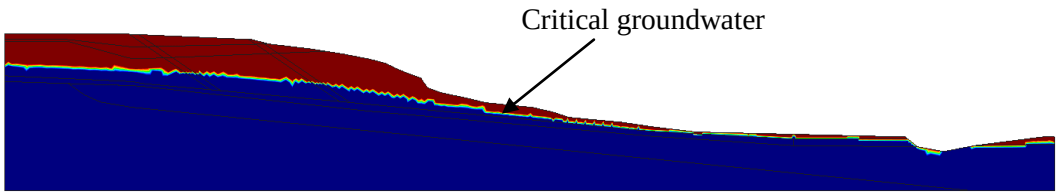

Fig.4.58 - The critical groundwater estimated by back-analysis

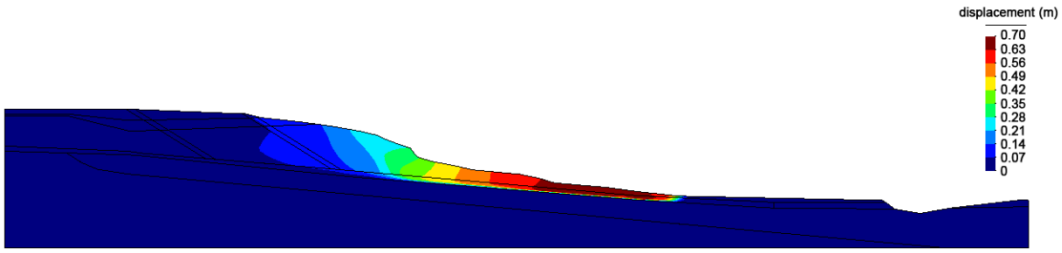

Fig.4.59 – Displacement field

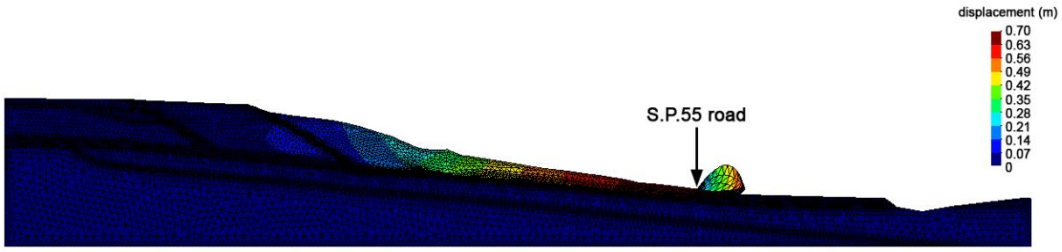

Fig.4.60 - Deformed mesh

4.7. Concluding remarks

Taking into account the information formerly gathered and according to the results achieved by the numerical analyses, it is possible to draw the following concluding remarks:

- the Maierato landslide was a reactivation owing to a significant increase in the groundwater pressure regime. In fact, although not exceptional, rainfall was the main triggering cause of the landslide. However, the occurred slope failure cannot be justified unless the residual strength parameters are assumed for some soils involved;
- the slip surface was essentially localized within the Miocene clay layer. It also developed into the overlying evaporitic limestone formation;
- the finite element analysis has also provided useful information about the failure mechanism and the size of the landslide body.

References

1. Alonso E. E., Gens A., Lloret A., Delahaye C. (1995) “Effect of rain infiltration on the stability of slopes” - Proc. 1st Int. Conf. Unsaturated Soils, Paris 1, 241-248
2. Angeli M.G., Gasparetto P., Menotti R.M., Pasuto A., Silvano S., (1996) “A visco-plastic model for slope analysis applied to a mudslide in Cortina d'Ampezzo” - Italy. Q. J. Eng. Geol. 29, 233–240
3. Bertini T., D’Elia B., Grisolia M., Olivero S., Rossi-Doria M. (1984) “Climatic conditions and slow movements of colluvium covers in central Italy” – Proc. 4th Int Symp Landslides, Toronto 1,367–376
4. Bertini, T., Cugusi F., D’Elia B, Rossi-Doria, M., (1986) “Lenti movimenti di versante nell’Abruzzo Adriatico: caratteri e criteria di stabilizzazione” - 16th Convegno Nazionale di Geotecnica, Bologna, vol. 1, pp. 91–100
5. Bishop A. W., Lovenbury H. T. (1969) “Creep characteristics of two undisturbed clays” - Proc. 7th Int. Conf. Soil Mech. Found. Engng, Mexico City 1, 29-37
6. Borrelli L., Antronico L., Gullà G., Sorriso-Valvo G.M. (2014) “Geology,geomorphology and dynamics of the 15 February 2010 Maierato landslide (Calabria,Italy)”. Geomorphology, 208:50-73
7. Bracegirdle A., Vaughan P.R., High D.W. (1992) “Displacement prediction using rate effects on residual shear strength” - Proc. 6th Int. Symp. Landslides Christchurch N Z 1:343 – 348
8. Calvello M., Cascini L., Sorbino G. (2008) “A numerical procedure for predicting rainfall induced movements of active landslides along pre-existing slip surfaces”. Int. J. Numer. Anal. Methods Geomech. 32(4):327–351
9. Carlslaw H. S., Jaeger J. C. (1959) “Conduction of heat in solids”. Oxford: Oxford University Press
10. Collins B., Znidarcic D. (1998) “Slope stability issues of rainfall induced landslides” - Proc. 11th Danube-European Conf. Soil Mech. Geotech. Engng, Porec, Croatia, 791-798
11. Conte E., Troncone A. (2011) “An analytical method for predicting the mobility of slow moving landslides owing to groundwater fluctuations” - J. Geotech. Geoenviron. Eng. ASCE 137(8):777–784;

12. Conte E., Troncone A. (2012) “Stability analysis of infinite clayey slopes subjected to pore pressure changes” - Geotechnique 62(1):87–91
13. Conte E., Donato A., Troncone A. (2014) “A finite element approach for the analysis of active slow-moving landslides” , Landslides 11(4):723-731
14. Corominas J., Moya J., Ledesma A., Lloret A., Gili,J. A. (2005) “Prediction of ground displacements and velocities from groundwater level changes at the Vallcebre landslide (Eastern Pyrenees, Spain)” - Landslides, 2, 83-96
15. Corominas J., Moya J., Lloret A., Gili J. A., Angeli M. G., Pasuto A., (2000) “Measurement of landslide displacements using a wire extensometer” - Engineering Geology, 55, 149-166
16. Cruden D. M., Varnes D. J. (1996) “Landslide types and processes”- In: Turner, K.A., Schuster, R.L. (Eds.), Landslides :investigation and mitigation, 247, 36-75
17. Cotecchia V., Melidoro G., Travaglini G., (1969) “I movimenti franosi e gli sconvolgimento della rete idrografica prodotti in Calabria dal terremoto del 1783” - Geol. Appl. Idrologeol., 4, 1-24
18. D’Elia B. (1991) “Deformation problems in the Italian structurally complex clay soils” - Proc. 10th European Conf. Soil Mech. Found. Engng, Florence 4, 1159-1170
19. D’Elia B. (1994) “Ricerca sperimentale sul comportamento reologico delle argille sovraconsolidate del Valdarno Superiore (Rapporto Finale)” - Internal Report, Università di Roma “La Sapienza”
20. D’Elia B., Esu F., Pellegrino A., Pescatore T. S. (1985) “Some effects on natural slope stability induced by the 1980 Italian earthquake” - Proc. 11th Int. Conf. Soil Mech. Found. Engng, San Francisco 4, 1943-1949
21. D’ Elia B., Picarelli L., Leroueil S., Vaunat J. (1998) “Geotechnical characterisation of slope movements in structurally complex clay soils and stiff jointed clays”. Riv. Ital. Geotecnica 32(3):5 – 32
22. Desai C. S., Samtani N. C., Vulliet L. (1995). “Constitutive modeling and analysis of creeping soils.” - J. Geotech. Eng., 121(1):43–56
23. Di Maio C. (1996a) “The influence of pore fluid composition on the residual shear strength of some natural clayey soils” - Proc. 7th Int. Symp. Landslides, Trondheim 2, 1189-1194, Balkema, Rotterdam
24. Di Maio C. (1996b) “Exposure of bentonite to salt solution: osmotic and mechanical effects” - Geotechnique 46, No. 4, 695-707
25. Di Prisco C., Imposimato S. (1996) “Time dependent mechanical behaviour of loose sands”- Mech. Coh.-Frictional Mater. 1(1):45–73
26. Di Prisco C., Imposimato S. (2002) “Static liquefaction of a saturated loose sand stratum” – Int. J. Solids Struct. 39:3523–3541

27. Fredlund D.G., Xing A., Fredlund M.D., Barbour S.L. (1996) “The relationship of the unsaturated soil shear strength to the soil-water characteristic curve” - Can Geotech Journal 33(3): 440-448
28. Fredlund D.G. (2000) “The 1999 R.M. Hardy Lecture: The implementation of unsaturated soil mechanics into geotechnical engineering” – Can Geotech Journal 37(5):963-986
29. Gattinoni P., Scesi L., Arieni L., Canavesi M. (2012) “The February 2010 large landslide at Maierato, Vibo Valentia, Southern Italy” – Landslides 9(2):255-261
30. Gottardi G., Butterfield R. (2001) “Modelling ten years of downhill creep data” – Proc. 5th Int. Conf. Soil Mech. Geotech. Eng., Istanbul Turk 1–3:27–31
31. Guerricchio A., Fortunato G., Guglielmo E.A., Ponte M., Simeone V. (2010) “Condizionamenti idrologici e da DGPV nell’attivazione della grande frana di Maierato (VV) del 2010” – Nuova Editoriale Bios
32. Gullà G., Sorbino, G. (1996) “Soil suction measurements in a landslide involving weathered gneiss”. Proc. 7th Int. Symp. Landslides, Trondheim 2, 749-754, Balkema, Rotterdam
33. Herrera G., Fernández-Merodo J.A., Mulas J., Pastor M., Luzi G., Monserrat O.A. (2009) “Landslide forecasting model using ground based SAR data: the Portalet case study”. Eng. Geol. 105(3–4):220–230
34. Hutchinson, J. N. (1987) “Mechanisms producing large displacements in landslides on pre-existing shears”- Mem. Geol. Soc. of China 9, 175-200
35. IUGS (1995) “A suggested method for describing the rate of movement of a landslides” - IUGS Working Group on Landslides. International Association of Engineering Geology, Bulletin, 52, 75-78
36. Johnson K. A., Sitar N. (1990) “Hydrologic conditions leading to debris-flow initiation”- Can. Geotech. J. 27, No. 6, 789-801
37. Kavvadas M. J. (1998) “General report: Modelling the soil behavior and selection of soil parameters” - Proc. 2nd Int. Symp. Geotech. “Hard Soils Soft Rocks”, Naples 3, 1441-1481, Balkema, Rotterdam
38. Kenney T. C., Lau K. C. (1984) “Temporal changes of groundwater pressure in a natural slope of non fissured clay” - Can. Geotech. J. 21, No. 1, 138-146
39. Lacerda W. A. (1989) “Fatigue of residual soils due to cyclic pore pressure variation” . Proc. 12th Int. Conf. Soil Mech. Found. Engng, Rio de Janeiro 5, 3085-3087.
40. Laloui L., Ferrari A., Bonnard C. (2009) “Geomechanical modelling of the Steinernase landslide (Switzerland)” - 1st IWL Napoli 1:186–195

41. Larsson R. (1977) “Basic behaviour of Scandinavian soft clays” – Report No. 4. Linkoping: Swedish Geotechnical Institute
42. Leroueil S., Marques M. E. S. (1996) “State of the art on the importance of strain rate and temperature effects in geotechnical engineering” - ASCE Conv., Washington, Geot. Spec. Pub. 81,1-60
43. Leroueil S. (1998) “Elements of time-dependent mechanical behaviour of overconsolidated clays” - Proc. 51st Can. Geotech. Conf., Edmonton 2, 671-677
44. Leroueil S. (2001) “Natural slopes and cuts: movement and failure mechanism” - Geotechnique, 51(3), 195-244
45. Leroueil S., Locat J., Vaunat J., Picarelli L., Lee H., Faure R. (1996) “Geotechnical characterization of slope movements” - Landslides, 53-74
46. Lollino P., Elia G., Cotecchia F., Mitaritonna G. (2010) “Analysis of landslide reactivation mechanisms in Daunia clay slopes by means of limit equilibrium and FEM methods”- Geot Spec Publ 199:3155–3164
47. Lupini J.F., Skinner A.E., Vaughan P.R. (1981) “The drained residual strength of cohesive soils” - Geotechnique, 31(2):181–213
48. Marchand G. (1982) “Quelques considerations sur le comportement avant rupture des pentes argileuses naturelles” - MSc thesis, Université Laval, Quebec
49. Marchetti S. (1980) “In situ tests by flat dilatometer” - Journal of the Geotech. Engin. Division, ASCE 106 (GT3, Proc.Paper,15290) 299-321
50. Newmark N.M. (1965) “Effects of earthquakes on dams and embankments” – Geotechnique 15(2):139–159
51. Nova R. (2002) “Fondamenti di meccanica delle terre”- McGraw-Hill
52. Olivella S., Gens A., Carrera J., Alonso E.E. (1996) “Numerical formulation for a simulator (CODE_BRIGHT) for the coupled analysis of saline media” - Eng Comput 13:87 – 112
53. Perzyna P. (1963) “The constitutive equations for rate sensitive plastic materials”. Quart. Appl. Math. 20:321–332
54. Picarelli L.(2000) “Meccanismi di deformazione e rottura dei pendii” – Hevelius
55. Picarelli L., Urciuoli G., Russo C. (2004) “Effect of groundwater regime on the behaviour of clayey slopes”. Can. Geotech.J. 41:467–484
56. Picarelli L. (1991) “Resistenza e meccanismi di rottura nei terreni naturali” - Convegno dei ricercatori sul tema: Deformazioni in prossimità della rottura e resistenza dei terreni naturali e delle rocce, Ravello 2, II.7-II.61
57. Potts D.M., Zdravkovic L. (1999) “Finite Element Analysis in Geotechnical Engineering” - vol.1 and vol.2.Thomas Telford

58. Roddeman D. G. (2013) “TOCHNOG user’s manual”, FEAT, The Netherlands. www.feat.nl/manuals/user/user.html
59. Rowe P. W., (1962) “The stress-dilatancy relation for static equilibrium of an assembly of particles in contact” - Proceedings of the Royal Society of London, Series A, Vol 269, pp. 500-527
60. Savage W.Z., Chleborad A.F. (1982) “A model for creeping flow in landslides” – Bull. Assoc. Eng.Geol 4:333–338
61. Singh A. W., Mitchell J. K. (1968) “General stress-strain-time function for soils” - J. Soil Mech. Found. Div., ASCE 94, No. 1, 21-46
62. Skempton A. W. (1985) “Residual strength of clays in landslides, folded strata and the laboratory” - Geotechnique, 35(1), 3-18
63. Stark T. D., Eid H. T. (1994) “Drained residual strength of cohesive soils” - J. Geotech. Engng. Div., ASCE 120, No. 5, 856-871
64. Sun H. W., Wong H. N., Ho K. K. S. (1988) “Analysis of infiltration in unsaturated ground” - Proc. Ann. Sem. Slope Engng. in Hong Kong, Hong Kong, 101-109
65. Tavenas F., Leroueil S., La Rochelle P., Roy, M. (1978) “Creep behaviour of an undisturbed lightly overconsolidated clay” - Can. Geotech. J. 15, No. 3, 402-423
66. Troncone A. (2005) “Numerical analysis of a landslide in soils with strain-softening behavior” - Geotechnique 55(8):585–596
67. Urciuoli G. (1990) “Contributo alla caratterizzazione geotecnica delle frane dell'Appennino” - Reports of the Istituto di Tecnica delle Fondazioni e Costruzioni in Terra - Università di Napoli Federico II
68. Van Asch T. W., Van Beek L., Bogaard T. A. (2007) “Problems in predicting the mobility of slow-moving landslides” - Engineering Geology, 91: 46-55
69. Van Asch T.W., Van Genuchten P.M. (1990) “A comparison between theoretical and measured creep profiles of landslides”- Geomorphology 3:45 – 55
70. Varnes D. J. (1978) “Slope movement types and processes” - In: Schuster R. L. & Krizek R. J. Ed., Landslides, analysis and control. Transportation Research Board Sp. Rep. No. 176. Nat. Acad. of Sciences
71. Vulliet L., Hutter K. (1988) “Viscous-type sliding laws for landslides” - Canadian Geotechnical Journal, 25(3): 467-477